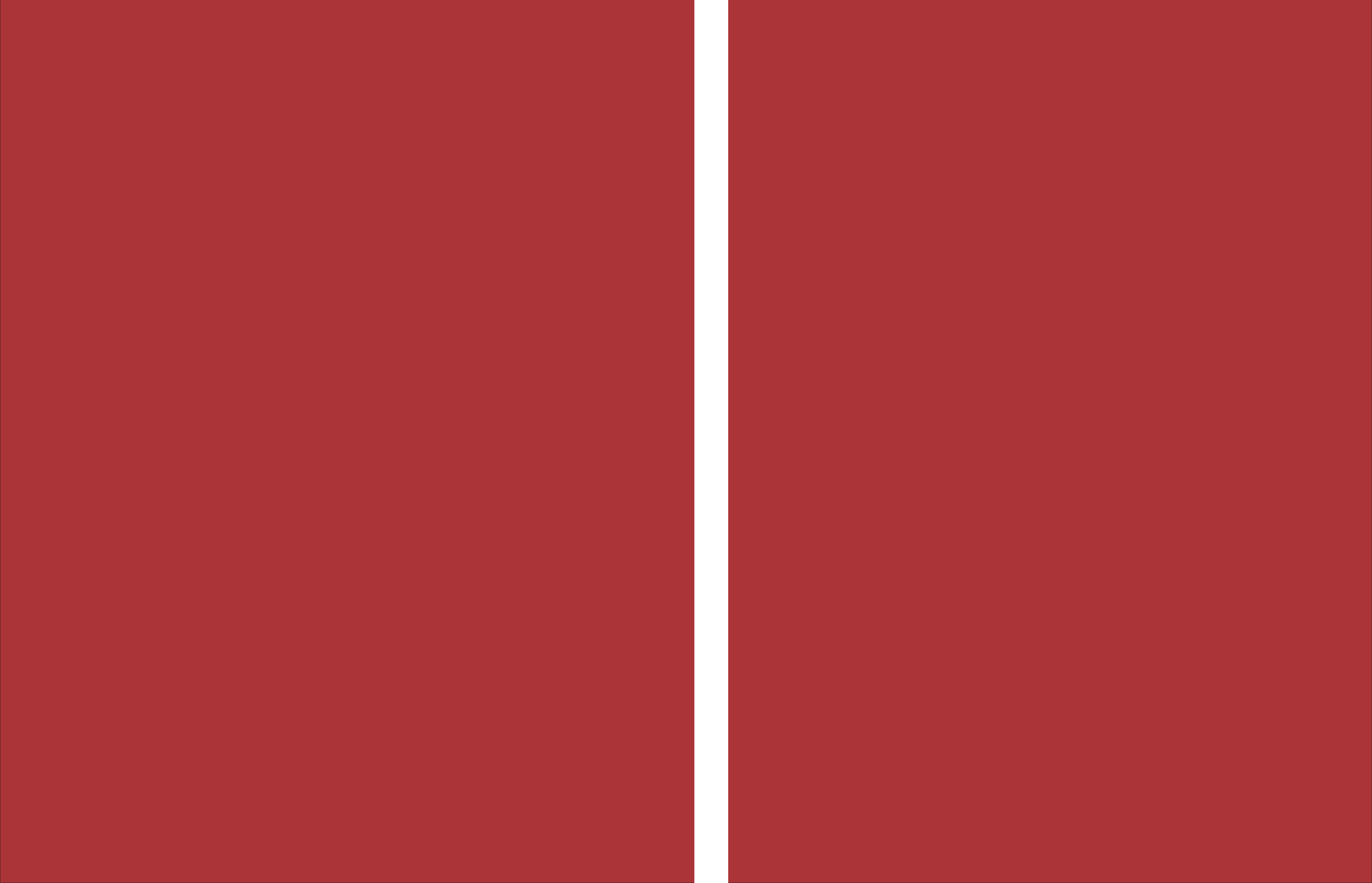


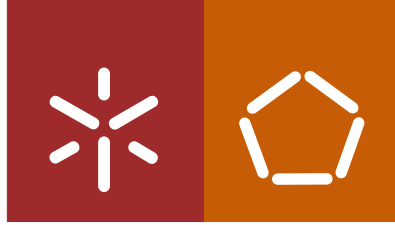


**Universidade do Minho**  
Escola de Engenharia

Carlos Nuno Veiga Barbosa

**Integration of Engineering, Manufacturing  
and Economic Issues in Design against  
Impact of Polymer Automotive Components**





**Universidade do Minho**  
Escola de Engenharia

Carlos Nuno Veiga Barbosa

**Integration of Engineering, Manufacturing  
and Economic Issues in Design against  
Impact of Polymer Automotive Components**

Tese de Doutoramento em Líderes para Indústrias Tecnológicas

Trabalho efetuado sob a orientação do  
**Professor Doutor Ricardo João Ferreira Simões**  
e do  
**Professor Doutor Júlio Cesar Machado Viana**

janeiro de 2018

## DECLARAÇÃO

**Nome:** Carlos Nuno Veiga Barbosa

**Endereço electrónico:** [nnunext@gmail.com](mailto:nnunext@gmail.com)

**Telefone:** +351912407969

**Número do Cartão de Cidadão:** 11505864

**Título da tese:** Integration of Engineering, Manufacturing and Economic Issues in Design against Impact of Polymer Automotive Components

**Orientador(es):**

Professor Doutor Ricardo João Ferreira Simões

Professor Doutor Julio César Machado Viana

Ano de conclusão:2018

**Designação do Doutoramento:** Líderes para as Industrias Tecnológicas (Enenharia de Concepção e Processos de Fabrico Avançado, programa MIT-Portugal)

DE ACORDO COM A LEGISLAÇÃO EM VIGOR, NÃO É PERMITIDA A REPRODUÇÃO DE QUALQUER PARTE DESTA TESE

Universidade do Minho, 30 / 01 / 2018

Assinatura: \_\_\_\_\_

## STATEMENT OF INTEGRITY

I hereby declare having conducted my thesis with integrity. I confirm that I have not used plagiarism or any form of falsification of results in the process of the thesis elaboration.

I further declare that I have fully acknowledged the Code of Ethical Conduct of the University of Minho.

University of Minho, 30 / 01 / 2018

Carlos Nuno Veiga Barbosa

---



## ACKNOWLEDGMENTS

First and foremost, I wish to thank Professor Ricardo Simões and Professor Julio C. Viana for their supervision, encouragement and support, which they provided as mentors and friends.

I would like to express my sincere gratitude to Engineer Markus Franzen and Doctor Thomas Baranowski, from Ford Werke GmbH, Research & Innovation Center Aachen, for their super professionalism, cordiality and friendliness, during my stay in Aachen, Germany.

To Professor Randolph Kirchain, from Materials System Laboratory of Massachusetts Institute of Technology, for his kind hospitality and knowledge sharing.

I would also like to express my gratitude to the people that helped me somehow with my experimental work. To my colleagues, professors and technicians from the Department of Polymer Engineering of the University of Minho.

To the Portuguese Foundation for Science and Technology (FCT) for their financial support through a PhD grant SFRH/BD/51570/2011.

To MIT-Portugal EDAM focus area through the international program of scientific and technical cooperation with Massachusetts Institute of Technology.

I would like to deeply express my gratitude to the exceptional people who inspired me in many ways over the course of these years. To my dear friends who have encouraged me over the many years it has taken to complete this degree.

At last, I am especially thankful to my family for their un-ending support, patience and careness. To them, I dedicate this thesis.





## ABSTRACT

This work investigates the influence of the injection molding conditions on the developed microstructure and consequently on the final mechanical properties of unreinforced polypropylene (PP). Also, it gives insights about the mechanical behavior dependency on time and temperature, considering meanwhile the process-induced microstructure. The properties are strongly affected by the morphology which is dictated thermomechanical environment. Therefore, a simulation chain from the injection molding simulation up to the structure simulation with appropriate micromechanical models was established and validated.

PP tensile samples were obtained through controlled injection molding design of experiments with 25 different processing condition settings. The relationships between the resulting morphologies and the mechanical properties measured under different strain rates and temperatures were investigated. Polarized light microscopy, wide-angle X-ray scattering, and differential scanning calorimetry, were employed to assess the structural heterogeneity of the moldings. High velocity tensile tests and dynamic-mechanical thermal analysis were carried out to study the thermo-mechanical response. The melt temperature was identified as the most significant variable for the development of the morphologies and the mechanical response of the moldings. According to the dynamic-mechanical thermal analysis, the mold wall temperature was found to have the highest influence on the storage static modulus and frequency sensitivity coefficient. The skin thickness, its crystallinity and molecular orientation (flow direction) influence, to a certain degree, the tensile properties of the materials.

The most challenging issue of this thesis was the development/application of a simulation chain that links injection molding simulation and crash simulation. The objective is to discretize/map the mechanical properties over the entire domain of an injection moulded unreinforced thermoplastic model by considering the process-induced microstructure. It was essential to develop a dedicated computer application – based on the thermomechanical indices methodology – that allows importing computer aided flow study results and locally, i.e. per element of the meshed model, characterising the thermo-mechanical environment. Mathematical functions have been used to correlate the TMI and the relevant mechanical properties of the thermoplastic moldings. A user defined material model can read those indices and translate them to local mechanical properties.

The simulation chain approach was tested in a case-study component (toolbox). Different combinations of molding conditions were selected to manufacture several toolbox replicates. The injection molding

process was simulated by means of Autodesk Moldflow Insight 2012 according to the production settings. Quasi-static (1 mm/s) and dynamic impact (3 m/s) tests were performed, the force-displacement curves being experimentally and numerically assessed. These tests have been simulated by using the finite element (FE) program LS-Dyna.

The different imposed thermomechanical environments do not show noteworthy variations among the experiments, neither for quasi-static nor for dynamic simulations. The simulations under quasi-static loads overestimate the peak force of the material. However, the overall response (elastic and hardening) is somehow correct. In the case of dynamic loads, the simulations can predict the overall force-displacement curves. In spite of small, the variations among the machine settings observed in real tests are reproduced by the integrative methodology proposed.

## RESUMO

Este trabalho investiga sobre a influência das condições de processamento no desenvolvimento da microestrutura e conseqüentemente nas propriedades mecânicas do polipropileno (PP) não-reforçado. Estuda também a dependência dessas propriedades em função da temperatura e tempo, considerando simultaneamente a morfologia determinada pelo processamento. As propriedades são largamente afetadas pela morfologia desenvolvida através do ambiente termomecânico. Por isso, esta tese estabelece válida uma metodologia de simulação em cadeia que relaciona resultados de simulação de injeção com resultados de simulação estrutural.

Provetes de tração em PP foram obtidos pela tecnologia de moldação por injeção. O processo foi controlado através de um design de experiências com 25 condições de processamento diferentes. Foram investigadas as relações entre a morfologia obtida e as propriedades mecânicas medidas a diferentes temperaturas e taxas de deformação. Várias técnicas laboratoriais foram utilizadas para quantificar a heterogeneidade microestrutural das moldações, tais como: microscopia de luz polarizada, varrimento de raio-X em largos-ângulos, calorimetria diferencial de varrimento, entre outras técnicas. Foram realizados ensaios de tração de alta velocidade e análises térmicas dinâmico-mecânicas para quantificar a resposta termomecânica dos provetes. A temperatura do fundido foi identificada como a variável mais significativa para o desenvolvimento microestrutural e conseqüente resposta mecânica. A temperatura do molde refletiu-se como a variável mais importante no módulo de armazenamento e no coeficiente de sensibilidade (relacionado com a frequência dos testes de dinâmico-mecânicos). As propriedades mecânicas dos materiais, são até certo nível, ditadas pela espessura da casca dos provetes, a sua cristalinidade e orientação molecular.

A tarefa mais desafiante desta tese foi o desenvolvimento a aplicação de uma metodologia de simulação em cadeia que co-relaciona resultados de simulação do processo de injeção com simulação de análise estrutural. O objetivo é discretizar/mapear as propriedades mecânicas no modelo tri-dimensional do componente, tendo em conta o ambiente termomecânico imposto durante o processamento. Para isso foi essencial o desenvolvimento de uma ferramenta computadorizada, baseada na metodologia dos índices termomecânicos, que permitiu exportar resultados de simulação de injeção e quantificar esse ambiente termomecânico para cada elemento finito da malha. Os índices termomecânicos foram relacionados matematicamente com as propriedades mecânicas. As relações matemáticas obtidas por este processo

semi-empírico foram depois incluídas nas equações constitutivas dos materiais que descrevem o comportamento mecânico.

A metodologia proposta foi testada num componente tipo-caixa (toolbox). Foram selecionadas várias condições de processamento, previamente identificadas, para produzir as caixas de teste. O processo de injeção foi simulado através do Autodesk Moldflow Insight 2012 de acordo com as condições de processamento reais. Ensaios quase-estáticos (1 mm/s) e dinâmicos (3 m/s) foram realizados, e as curvas força-deslocamento foram avaliadas experimentalmente e numericamente. Estes ensaios foram simulados através do programa de análise de elementos finitos LS-Dyna.

Os ambientes termomecânicos determinados pelas diferentes condições de processamento revelaram variações diminutas para ambos os casos de simulação. As simulações quase-estáticas resultaram numa força de pico sobreavaliada. No entanto, a resposta experimental global é de certa forma bem descrita pela simulação. No caso dos ensaios dinâmicos, a simulação consegue prever globalmente as curvas de força-deslocamento. Apesar de pequenas, as variações observadas entre as curvas experimentais obtidas pelas diferentes amostras / condições de processamento são reproduzidas pela metodologia de simulação em cadeia proposta.

# CONTENT

Acknowledgments.....	iii
Abstract.....	vii
Resumo.....	ix
Content.....	xi
List of Figures.....	xv
List of Tables.....	xix
List of Abbreviations.....	xxi
List of Symbols.....	xxiii
List of Publications.....	xxvii
1. Introduction.....	1
1.1 Research problem statement.....	1
1.2 Background.....	2
1.3 Technical approach.....	4
1.4 Overall project milestones.....	4
1.5 Thesis organization.....	5
References.....	5
2. Comprehensive study on the relationships between processing, microstructure and mechanical properties of injection molded polypropylenes.....	7
Abstract.....	7
2.1 Introduction.....	8
2.2 Experimental.....	9
2.2.1 Materials and test specimen geometries.....	9
2.2.2 IM experimental design.....	9
2.2.3 Morphology characterization.....	11
2.2.4 Mechanical characterization.....	14
2.3 Results and discussion.....	15
2.3.1 Influence of the IM conditions on morphologies.....	15
2.3.2 Influence of the IM conditions on the tensile properties.....	20

2.4	Comprehensive summary of structure-processing-mechanical properties relationships.....	23
2.4.1	Processing-morphology relationships analysis.....	24
2.4.2	Processing-mechanical properties relationships analysis.....	24
2.4.3	Morphology-mechanical properties relationships analysis.....	25
2.5	Conclusions .....	28
	References .....	29
3.	Mechanical properties dependency on time, temperature and molding conditions for a PP .....	31
	Abstract.....	31
3.1	Introduction.....	31
3.2	Experimental and data analysis .....	34
3.2.1	Materials and test specimen geometries.....	34
3.2.2	Injection molding experimental design.....	35
3.3	Dynamic mechanical thermal analysis .....	36
3.3.1	Equipment and test conditions.....	36
3.3.2	Dynamic mechanical investigations.....	36
3.3.3	Time-temperature superposition (TTS) principle.....	37
3.4	Results and discussion .....	38
3.4.1	Storage modulus, $E'$ .....	38
3.4.2	Loss or damping factor, $\tan\delta$ .....	40
3.4.3	Magnitude of the $\beta$ -relaxation process, $A\beta$ .....	42
3.4.4	Time-temperature superposition (TTS) and master curves.....	44
3.4.5	Dependency on processing .....	48
3.5	Conclusions .....	54
	References .....	55
4.	Applying flow simulations in the development process of injection molded thermoplastic parts.....	57
	Abstract.....	57
4.1	Introduction.....	57

4.2	Injection moulding simulation .....	59
4.3	Thermo-mechanical environment in injection moulding .....	60
4.3.1	Thermo-mechanical variables.....	60
4.3.2	Thermo-mechanical indices .....	61
4.4	TMI predictive tool.....	66
4.5	Experimental design .....	67
4.5.1	Importing and meshing.....	67
4.5.2	Moulding window size and simulation design.....	68
4.6	Results and discussion .....	73
4.7	Conclusion remarks and future work.....	76
	References .....	77
5.	Integrative simulation chain for designing automotive injection moulded thermoplastic components: linking process and structural simulations .....	79
	Abstract.....	79
5.1	Introduction.....	80
5.2	Materials and moldings production .....	82
5.2.1	Thermoplastic material .....	82
5.2.2	Moldings production .....	82
5.3	Samples preparation and physical testing .....	84
5.3.1	Quasi-static tests .....	84
5.3.2	Dynamic tests.....	85
5.4	Simulation techniques and mapping tools.....	86
5.4.1	Moldflow simulations .....	86
5.4.2	Structural FEA and material model.....	87
5.4.3	Computer applications for properties prediction and mapping.....	88
5.5	Integrative simulation approach .....	90
5.6	Results and discussion .....	91
5.6.1	Integrative methodology validation through simpler simulations .....	92
5.6.2	Quasi-static (compression) experiments and simulations .....	93

5.6.3	Dynamic (impact) tests experiments and simulations.....	93
5.7	Conclusions .....	94
	References .....	95
6.	Cost modeling for early stage design decisions: A moldflow-based technical cost estimation for injection molded thermoplastic parts.....	99
	Abstract.....	99
6.1	Introduction.....	99
6.2	Literature review.....	101
6.3	Cost modeling methodology.....	102
6.4	Case-study presentation .....	107
6.5	Results and discussion .....	108
6.5.1	Design features .....	109
6.5.2	Number of cavities.....	109
6.5.3	Annual production volume .....	111
6.6	Conclusions .....	111
6.7	Further research .....	112
	References .....	112
7.	Global synthesis.....	115



## LIST OF FIGURES

Figure 2-1. Representation of the skin/core microscopy analysis procedure.....	11
Figure 2-2. Transversal sections from microtomed bar samples: (a) PP07 bars, experiment E09; and (b) PP07 bars, experiment E16.....	15
Figure 2-3. ANOVA summary of the effect of the significant IM parameters on the $Sa$ .....	16
Figure 2-4. ANOVA summary of the effect of the significant IM parameters on $\chi s$ .....	17
Figure 2-5. ANOVA summary of the effect of the significant IM parameters on $\Omega s$ .....	18
Figure 2-6. ANOVA summary of (a) the effect of the significant IM parameters on $\beta 300$ , and (b) two factor interaction effects [ $vi \times Ti$ ] evaluated on $\beta 300$ of PP07 bars. ....	19
Figure 2-7. ANOVA summary of the effect of the significant IM parameters on E (normalized values)..	21
Figure 2-8. ANOVA summary of the effect of the significant IM parameters on $\sigma y$ (normalized values). .....	22
Figure 2-9. ANOVA summary of the effect of the significant IM parameters on $\sigma y$ (normalized values). .....	23
Figure 2-10. Variations of the mechanical properties (normalized values) with $Sa$ versus $\chi s$ (a, c, and e); and $Sa$ versus $\Omega s$ (b, d, and f). Data for PP07 are represented by the low density mesh ( $\square$ ) and data for PP81 by the high-density mesh ( $\circ$ ). ....	27
Figure 3-1. Geometry of the injection molded test specimens. ....	34
Figure 3-2. $E'$ as a function of temperature and frequency (0.03, 1 and 10 s <sup>-1</sup> ) for selected IM experiments. ....	39
Figure 3-3. $E'$ as function of temperature for the selected IM experiments at $f = 0.1 \text{ s}^{-1}$ . ....	40
Figure 3-4. $\tan\delta$ as a function of temperature and frequency (0.03, 1 and 10 s <sup>-1</sup> ) for the selected IM experiments. ....	41
Figure 3-5. $\tan\delta$ as a function of the temperature for the selected IM experiments at $f = 0.1 \text{ s}^{-1}$ ....	42
Figure 3-6. $\beta$ -relaxation curves obtained for 8 selected experiments at 0.1 s <sup>-1</sup> (dataset of lower amplitude curves) and 10 s <sup>-1</sup> (dataset of higher amplitude curves).....	43
Figure 3-7. $E'$ vs. $f$ for a range of temperatures and for E06 and E11 samples.....	45
Figure 3-8. $E'$ master curves for the E06 and E11 at a reference temperature of 23 °C: a) $E'$ vs. $f$ over a wide range of frequencies; and b) $E'$ vs. $f$ covering only the range of 10 <sup>-3</sup> to 10 <sup>2</sup> s <sup>-1</sup> . ....	45

Figure 3-9. Variation of $\log aT$ with $1T - 1T_{ref}$ for the molded specimens of E06 and E11 [dashed lines represent the linear fits for each experiment (grey $\square$ – E06, black $\square$ – E11) and $\bullet$ stands for the $T_{ref}$ , where $aT = 1$ (no shift), thus $\log aT = 0$ ].	47
Figure 3-10. Variation of $Tg$ with $Tw$ at frequencies of 0.1 and 10 $s^{-1}$ .	48
Figure 3-11. Variations of $FWHM$ with the significant processing conditions for frequencies: a) 0.1 $s^{-1}$ and b) 10 $s^{-1}$ .	49
Figure 3-12. Variations of $\beta$ -relaxation peak area, $A\beta$ , with the significant processing conditions for frequencies: a) 0.1 $s^{-1}$ and b) 10 $s^{-1}$ .	50
Figure 3-13. Variations of the static modulus $E'0$ (at $f = 0$ and at 23 °C) with the significant processing conditions.	51
Figure 3-14. Variations of the frequency (strain-rate) sensitivity coefficient, $m$ , with: a) significant processing conditions; and b) 2Fl.	52
Figure 4-1. Flow chart scheme for the TMI computation and prediction of the mechanical properties at model mesh element level (see online version for colours).	67
Figure 4-2. CAD model to mesh, (a) the imported STL file and the scaled-up image (b) the finite element post-processed mesh model with four gate locations (yellow cones) (see online version for colours).	67
Figure 4-3. XY plot of the maximum pressure drop as a function of the injection time for the considered combinations of processing temperatures.	69
Figure 4-4. XY plot of the flow front temperature as a function of the injection time for the considered combinations of processing temperatures.	70
Figure 4-5. XY plot of the shear rate as a function of the injection time.	71
Figure 4-6. XY plot of the shear stress as a function of the injection time for the considered combinations of processing temperatures.	71
Figure 4-7. 95 <sup>th</sup> percentile results of the holding/packing time versus part weight and bulk temperature.	72
Figure 4-8. a) STL model of the door panel with the respective labels of the AOI and the injection moulding locations marked in black spots; b) AOI labelling in the physical component: AOI#1 (tags 18-20); AOI#2 (tags 22-24); AOI#3 (tags 14-16); AOI#4 (tag 10 marked with a dashed line); and AOI#5 (tags 37-45).	74
Figure 4-9. Variation of the Young's modulus with the TMI for the AOI#5 ( $R2 = 0.83$ ).	75
Figure 4-10. Measured and computed Young's modulus results for the envisaged AOI.	76
Figure 5-1. Geometry of the injection molded plastic box case study part.	83

Figure 5-2. Simplified injection molded plastic box for laboratorial testing (dashed lines region represents the glued area; see dynamic tests).....	84
Figure 5-3. Identification of the most relevant setup elements for a quasi-static compression test. ....	85
Figure 5-4. Representation of the single body – toolbox glued against the fixation plate (calmping plate and fixation modules). ....	86
Figure 5-5. Identification of the most relevant setup elements for a dynamic (drop tower) test. ....	86
Figure 5-6. Finite element model used in the LS-Dyna simulations (semi-transparent top plate represents the compression/impact plate). ....	88
Figure 5-7. Cooling index as mapped by TMI-App (left image as per rheological mesh) and by MAPIT (right image as per structural mesh) for a simple disc geometry. ....	89
Figure 5-8. Thermo-stress index as mapped by TMI-App (left image as per rheological mesh) and by MAPIT (right image as per structural mesh).....	89
Figure 5-9. Integrative user-defined simulation chain to link the processing induce material changes with commercial explicit finite element codes. ....	91
Figure 5-10. a) coundary prescribed motion for tensile simulation; b) comparative results for different inputs.....	92
Figure 5-11. Comparitive results between simulation and experimental quasi-static tests for the toolbox, as a function of the processing conditions.....	93
Figure 5-12. Comparitive results between simulation and experimental dynamic tests for the toolbox, as a function of the processing conditions. ....	94
Figure 6-1. Process-based cost modelling framework [10, 11]. ....	102
Figure 6-2. CAD models: M2a and M2b (modified). ....	108
Figure 6-3. Elementary costs and total manufacturing costs estimation of both models for a batch number of 200k parts.....	109
Figure 6-4. Elementary and total costs sensibility to the number of cavities. ....	110
Figure 6-5. Cost per-part sensibility as a function of the annual production volume.....	111



# LIST OF TABLES

Table 2-1. Injection molding experimental plan for the tested materials (FCC design). ..... 10

Table 2-2. Diffracted angle,  $2\theta$ , and the correspondent Miller indices and crystal form of iPP. .... 13

Table 2-3. Summary of the linear (1<sup>st</sup>-order) and non-linear ( $X^2$  and 2FI) effects of the processing conditions on the selected morphologies (▲ increase and ▼ decrease). .... 24

Table 2-4. Summary of the linear (1<sup>st</sup>-order) and non-linear ( $X^2$  and 2FI) effects of the processing conditions on the selected tensile properties (▲ increase and ▼ decrease). .... 25

Table 2-5. Maximum and average variations of the mechanical properties predictive models as a function of morphological parameters, for both materials. .... 26

Table 3-1. Main features of the PP81 material. .... 34

Table 3-2. Injection molding experimental plan based on a FCC orthogonal array ( $vi$  – injection velocity,  $Ti$  - melt temperature,  $Tw$  – mold temperature,  $Ph$  – holding pressure). .... 35

Table 3-3.  $\tan\delta$  parameters for all IM conditions at distinct frequencies ( $Tg$  – glass transition temperature,  $FWHM$  – full width at half maximum of the  $\beta$ -relaxation peak, and  $A\beta$  – area of the  $\beta$ -relaxation peak). .... 44

Table 3-4. Parameters from the  $E'$  vs  $f$  curves for all molding conditions [ $E'0$  – storage static modulus ( $f = 0$  Hz at 23 °C),  $m$  – frequency (strain-rate) sensitivity coefficient, and  $Ea$  – activation energy]. 46

Table 3-5. Summary of the linear (1<sup>st</sup>-order) and non-linear ( $X^2$  and 2FI) effects of the processing conditions on the selected properties (▲ increase and ▼ decrease). .... 53

Table 4-1. Boundary injection times as a function of the processing temperatures. .... 70

Table 4-2. Injection moulding simulation design. .... 73

Table 4-3. TMI (normalized) results of the two extreme processing conditions for all regions of interest. .... 74

Table 5-1. Technical data of the PP81 (Moldflow database). .... 82

Table 5-2. Boundary injection times as a function of the processing temperatures. .... 83

Table 6-1. Considered manufacturing cost elements. .... 103

Table 6-2. General injection molding settings. .... 108



## LIST OF ABBREVIATIONS

IM	Injection moulding
PP	Polypropylene
DOE	Design of experiments
RSM	Response surface methodology
ANOVA	Analysis of variance
iPP	Isotactic polypropylenes
MFI	Melt flow index
MWA	Molding window analysis
FCC	Face central composite
2FI	Two factor interactions
X <sup>2</sup>	Quadratic factor or 2 <sup>nd</sup> -order effect
PLM	Polarized light microscopy
WAXS	Wideangle X-ray scattering
DSC	differential scanning calorimetry
DMTA	Dynamic-mechanical thermal analysis
TTS	Time-temperature superposition
WLF	Williams-Landel-Ferry
FWHM	Full width at half maximum
CAE	Computer-aided engineering
TME	Thermo-mechanical environment
AMI	Autodesk Moldflow Insight
TMI	Thermo-mechanical indices
TMV	Thermo-mechanical variables
CI	Cooling index
TSI	Thermo-stress index
AOI	Area of interest
STL	
OEMs	Original equipment manufacturers
CAD	Computer-aided design

FEA	Finite element analysis
FEM	Finite element model
PDD	Product design and development
PBCM	Process-based cost model
MIT	Massachusetts Institute of Technology
MSL	Materials System Laboratory
RMP	Raw material price
AMC	Annual material consumption
EPV	Effective production volume
ER	Electricity requirement
EC	Electricity cost
ADW	Allocated direct workers
APT	Annual paid time
DW	Direct wages
NDL	Number of direct laborers
PLA	Percentage of the line allocated (dedicated line)
PLR	Percentage of the line required (non-dedicated line)
PBC	Press base cost
PIC	Press installation cost
AEC	Cost of eventual auxiliary equipment
MBC	Mold base cost
CCC	Cavity and core cost
AIW	Allocated indirect workers
RBS	Required building space
BSC	Building space cost
WCP	Working capital period
ABS	Acrylonitrile-butadiene-styrene



## LIST OF SYMBOLS

$\rho_s$	Solid density
$\rho_m$	Melt density
$v_i$	Injection velocity
$T_i$	Injection temperature
$T_w$	Mold temperature
$P_h$	Holding pressure
$S_a$	Skin-to-core thickness ratio
$R_t$	Representative radius of the bar samples
$h$	Skin thickness
$\Omega_s$	Molecular orientation of the skin
$\chi_s$	Index of crystallinity of the skin
$\beta_{300}$	$\beta$ -phase content of the skin
$\lambda$	Wave length
$S_{total}$	Total area below the intensity X-ray scan curve
$S_{cryst}$	Specific area of the X-ray crystalline peaks
$\chi_b$	Index of bulk crystallinity
$\Delta H_m$	Enthalpy of fusion
$\sigma^t - \varepsilon^t$	True stress–true strain curves
$E$	Modulus of elasticity
$\sigma_y$	Stress at yield
$\varepsilon_b$	Strain at break
% $p$	Percentage of contribution of the model parameter
<i>Model</i> $R^2$	Coefficient of determination of the model
<i>Adj.</i> $R^2$	Adjusted coefficient of determination of the model
<i>Pred.</i> $R^2$	Adjusted coefficient of determination of the model
$t_r$	Time allowed for relaxation
$\lambda$	Relaxation time of the material
% <i>Max. Res.</i>	Maximum percentage of the residuals

$\%Ave. Res.$	Average percentage of the residuals
$R^2$	Coefficient of multiple correlation
$T$	Temperature
$f$	Frequency
$\delta$	Phase lag, or phase angle
$\dot{\epsilon}$	Strain rate
$d_0$	Displacement amplitude
$l_0$	Reference specimen length or grip distance
$E_0$	Reference elastic modulus
$\dot{\epsilon}_0$	Reference strain-rate
$m$	Strain-rate sensitivity coefficient
$\dot{\gamma}$	Viscosity
$\theta$	Average specimen diameter cross-section
$l$	Averaged specimen length
$E'$	Storage modulus
$\tan\delta$	Damping factor
$E''$	Loss modulus
$A_\beta$	Magnitude the $\beta$ -relaxation process
$T_g$	Glass transition temperature
$T_{ref}$	Reference temperature
$a_T$	Shift factor
$R$	Universal gas constant
$E_a$	Activation energy
$E'_0$	Static modulus
$v_j$	Uncoded factor value
$\bar{v}$	Mean of the uncoded factors
$Y_c$	Cooling index
$\tau_Y$	Thermo-stress index
$t_i$	Injection time
$t_h$	Packing or holding time
$t_c$	Cooling time

$C_{total}$	Total fabrication cost
$C_{mat}$	Material cost
$C_{ene}$	Energy cost
$C_{lab}$	Labor cost
$C_{press}$	Injection molding machine (or press) cost
$C_{mold}$	Injection molding tool (or mold) cost
$C_{ohla}$	Operational overhead labor cost
$C_{build}$	Building cost
$C_{wcap}$	Working capital cost
$C_{maint}$	Maintenance cost
$I_m$	Payment of loans for a machine (credit or investment)
$n_m$	Accounting life of a machine (in years)
$i_r$	Capital recovery rate (in %)
$F_c$	Injection molding machine clamping force
$I_t$	Payment of loans for a tool (credit or investment)
$n_t$	Accounting life of a tool (in years)
$A_c$	Area of the mold base plate
$h_p$	Combined thickness of cavity and core mold base plates
$t_0$	Total number of hours to manufacture the mold
$t_{es}$	Manufacturing hours to produce the ejection system
$t_{gf}$	Manufacturing hours to produce one cavity
$t_{ps}$	Manufacturing hours to produce one core
$A_p$	Total projected area of the part
$N_{sp}^{in}$	Number of surface patches/segments of the inner surfaces
$N_{sp}^{ou}$	Number of surface patches/segments of the outer surfaces
$I_b$	Payment of loans for a building (credit or investment)
$n_b$	Accounting life of a building (in years)
$F_p$	Impact peak force
$U_p$	Impact peak energy
$U_b$	Impact break energy
$\equiv$	Equivalent to



## LIST OF PUBLICATIONS

C.N. Barbosa, R. Simoes, M. Franzen, T. Baranowski, and J.C. Viana. Comprehensive study on the relationships between the processing, the microstructure and mechanical properties of injection molded polypropylenes. *Polymer Engineering and Science*, DOI 10.1002/pen.24650 (2017).

C.N. Barbosa, R. Simoes, J.C. Viana, M. Franzen, T. Baranowski, and P. Afonso. Cost modeling for early stage design decisions: A moldflow-based technical cost estimation for injection molded thermoplastic parts. *International Conference on Project Evaluation, ICOPEV, Guimarães* (2016).

C.N. Barbosa, F. Carvalho, J.C. Viana, M. Franzen, T. Baranowski, and R. Simoes. Applying flow simulations in the development process of injection moulded thermoplastic parts. *International Journal of Materials and Product Technology*, 52, 76-95 (2016).

C.N. Barbosa, F. Carvalho, J.C. Viana, M. Franzen, and R. Simoes. Impact performance prediction of injection-molded talc-filled polypropylene through thermomechanical environment assessment. *International Journal of Advanced Manufacturing Technology*, 77, 873-883 (2015).

C.N. Barbosa, R. Simoes, M. Franzen, and J.C. Viana. Thermomechanical environment characterisation in injection moulding and its relation to the mechanical properties of talc-filled polypropylene. *Journal of Materials Science*, 48, 2597-2607 (2013).

C.N. Barbosa, J.C. Viana, M. Franzen, and R. Simoes. Effect of the impact conditions on the mechanical properties of injection-molded parts. *Polymer Engineering and Science*, 52, 1845-1853 (2012).



# 1. INTRODUCTION

This work was developed under the framework of the Leaders for Technical Industries (LTI) doctoral program within the Engineering Design and Advanced Manufacturing (EDAM) focus area of the MIT-Portugal program.

The LTI PhD program considers that product and process innovation and current complex decision-making must also take into account economics, management and social aspects. Along these lines, a collaboration between University of Minho (Guimarães, Portugal) and Ford Research & Advanced Engineering Europe (Aachen, Germany) was agreed in order to carry out the research tasks which focus on improving and predicting the mechanical performance and engineering costs of injection moulded plastic parts through simulation approaches.

The project was developed under the scientific supervision of Professors Ricardo Simões and Júlio Viana from MPP-UMinho. The sponsorship and technical guidance was supported by Markus Franzen and Thomas Baranowski from Ford Research & Advanced Engineering Europe.

## 1.1 Research problem statement

Automotive plastic components are sometimes required to withstand deformation at high strain rate during their service life. Safety regulations impose increasingly demanding specifications for energy absorption during impact loading of interior plastic components (e.g., pillar covers, dashboard, door panels, interior trim, airbag covers), with the aim of preventing injuries to the occupants.

Contrasting with this increasing need, the knowledge of the impact behavior of polymeric materials is scarce, and the use of valid predictive methodologies and tools is rare. This creates numerous difficulties in the design of plastic components that withstand impact loading, typically leading to the adoption of empirical approaches based on phased trial-and-error experimentation. Needless to say, such methodologies absorb large amounts of resources and result in over-engineering of the plastic components. The existent knowledge limitations are mainly related to:

- i) the intrinsic nature of the impact event (thermomechanical coupling, localized phenomena, friction effects, monitoring difficulties);
- ii) the intricate loading conditions imposed in testing methods;
- iii) complex mechanical behavior of polymers with high time-temperature sensitivity;
- iv) marked dependence of polymers' properties upon their microstructure.

The impact behavior of polymers is, in fact, far from being completely understood. For instance, current testing methods do not provide intrinsic material properties (the response being dependent both upon the test and the sample geometry), and thus do not support predictive efforts. Additionally, polymer behavior is dictated to a large extent by the processing conditions used to manufacture the plastic components, that is, by the process-induced microstructure. Moreover, the effects of temperature and strain-rate on the response of molded plastics are also influenced by the microstructure.

Adequately accounting for this phenomena could result in very significant improvements in materials selection and design processes for interior safety components, amongst other applications. Therefore, this project aims at improving knowledge about the impact behavior of plastics by establishing accurate relationships between the processing conditions, the developed microstructure and the consequent mechanical response of moldings. The approach here proposed combines experimental and computational efforts to design and process the plastic component for optimized mechanical behavior by “controlling” the microstructure development during processing. A simulation chain from the mold filling simulation up to the structural simulation with appropriate material constitutive model is established.

The molding conditions of a specific polymer leads to a set of product characteristics, comprising function, quality and cost. Currently, there is no computational tools offering such an integrative evaluation. It is therefore essential to have an holistic perspective upon the product development process, allowing the prediction and subsequent optimization of a plastic component, through computer modeling and simulation.

## 1.2 Background

The mechanical behavior of polymers (e.g. polypropylene, PP) at high strain rate is a scientific field of scarce research efforts, with very limited amount of published work on the subject, in spite of the high industrial relevance. A relatively high number of impact test methods does exist but mainly aimed at ranking materials rather than acquiring relevant design data. Typically, the results between distinct types of tests are difficult to extrapolate between each other [1]. In fact, the current test methods do not give intrinsic material properties, as the response is both test and sample geometry dependent.

One of the most extensively used mechanical tests used to obtain basic mechanical properties (e.g., elastic modulus, yield stress and strain at break) is the tensile test. Extensive knowledge is available about the mechanical behaviour of PP at quasi-static conditions (strain-rate  $< 10^{-2} \text{ s}^{-1}$ ) whilst due to the complicated experimental procedure and data interpretation not enough reliable material data has so far



been determined at high strain rates [2-7]. There are not many studies regarding high speed tensile tests ( $\equiv$  tensile-impact tests) of polymeric materials because, no standard, only a recommendation procedure by the Society of Automotive Engineers (SAE) exists. This makes the experimental procedure and data interpretation hard to standardize.

Polymers exhibit a complex mechanical behavior strongly influenced by temperature, strain-rate and loading mode sensitivities, and still with a marked dependence upon the morphology developed during processing. Such intricate relationships render difficult the accurate characterization of the polymer behavior, and the technical hitches increase when high strain rates are involved.

Engineering procedure to study the mechanical behaviour of injection moulded semi-crystalline polymers has been based on the scale features of this skin-core laminate arrangement. Due to the strong stress and temperature gradients existent in the injection molding (IM) process, several types of hierarchical superstructures such as the skin ratio [8-11], molecular orientation [12-14], and polymorphic crystalline structures [15-18] are developed across the tri-dimensional domain of the moldings. Therefore, the establishment of straightforward relationships between processing conditions, microstructural features development and consequent mechanical responses is a complex issue [19-24].

Another priority in an industrial context is the development of predictive tools that can be used in the product design stage, avoiding the current cumbersome and costly empirical approaches. In spite of its high importance, the prediction of the impact resistance of plastic parts is still a rather difficult engineering task. Moreover, modeling the mechanical behavior of polymeric materials requires significant computational effort. Simulations based on the finite element method (FEM) are typically adopted, but are often ran as black-boxes or using over-simplified models that are not adequate for the material in use. Explicit methods are normally adopted to solve the non-stationary, highly coupled, mechanical and thermal problems involving several non-linearities (e.g., large displacements, complex elastic-visco-plastic material behavior and intricate contact conditions) [1, 25, 26].

Despite the complex anisotropic behaviour of injection molded semi-crystalline thermoplastics, phenomenological models are widely used to improve the mechanical behavior prediction of these materials [25-31]. The constitutive models proposed in the literature for polymeric materials do not explicitly include the microstructure influence (dependent on material and molding conditions) on the stress-strain relationship, and are therefore unable to support accurate numerical predictions. The development of predictive methodologies and tools for designing impact resistant polymer components that encompasses the influence of molding conditions on the microstructure and properties emerges, therefore, as an important research area.

### 1.3 Technical approach

The ultimate goal of this work is to establish the relationships between processing, microstructure, and mechanical behavior of injection molded parts, and to develop a methodology for designing impact-resistant plastic components, while simultaneously considering processing effects and engineering costs. The approach is based on a synergistic and complementary combination of a detailed experimental characterization and accurate simulation of the molding process and impact behavior.

Processing conditions are systematically varied based on a design of experiments (DOE) approach. The microstructure of the moldings is characterized by several structure-sensitive techniques in order to assess skin thickness, degree of crystallinity (bulk and at skin), and level of molecular orientation at skin. The impact behavior is assessed by true stress-true strain tensile and instrumented crash tests at different strain rates. The critical processing parameters influencing the morphological features and consequently the mechanical response are identified. The analysis technique incorporate the thermal and the mechanical issues.

Based on previous results, the thermomechanical indices methodology (and its dedicated computer tool) is applied in order to establish straightforward relationships between processing and properties. This relevant information is then included in FEA codes (linking processing/rheological and structural simulations). Due to the nature of the phenomena, explicit algorithms are the adequate framework to develop the simulation model. Typically, this involves contact modeling with adequate models for thermal, strain-rate and processing dependence of constitutive equations.

Finally, a process-based cost model (PBCM) has been used to predict the engineering costs of an injection molded component based on its geometric features and process simulation results (cycle time, etc.).

### 1.4 Overall project milestones

This research work combines experimental and computational efforts with advanced engineering methodologies. The main objectives of this work are:

- Improve the understanding on the impact behaviour (in a wide range of strain rates) of injection moulded polymers;
- Correlate processing, microstructure, and mechanical properties;
- Identify the relevant microstructure parameters determining mechanical properties;
- Enhance the TMI formulation to better predict part behaviour;

- Introduction of the effects of processing on constitutive parameters by coupling flow and structural simulations;
- Simulation of the impact tests with phenomenological constitutive laws, considering the effect of processing;
- Adapt a process-based cost model to predict the engineering costs of moldings;
- Propose and evaluate mechanisms to translate and apply these approaches into industrial practice.

## 1.5 Thesis organization

Hereafter, the document is divided in two main sections: i) ; and ii) . The first section presents the relevant topics and results of the thesis: i) study the relationships between processing *vs.* microstructure *vs.* mechanical properties of injection molded polypropylenes; ii) study the mechanical properties dependency of injection molded polypropylenes on strain rate and temperature; iii) study the thermomechanical environment through flow simulations for improved mechanical properties prediction/mapping; iv) implement an integrative methodology to link molding process and structural simulations for an unreinforced polypropylene; and v) develop a moldflow-based technical cost model for engineering costs estimation at early product design stages. The second section resumes the overall work, presents a set of conclusions and points out the main unsolved issues.

## References

1. J.C. Viana, N.Billon and A.M. Cunha. Proceed. 11th Conf. Def. Yield & Fract. Polymer, Cambridge, (2003).
2. High Strain Rate Tensile Testing of Polymers J2749, SAE international (2008).
3. M. Zrida, H. Laurent, V. Grolleau, G. Rio, M. Khelif, D. Guines, N. Masmoud, and C. Bradai, Polym. Test., 29, 685 (2010).
4. S.R. Raisch and B. Möglinger. Polym. Test., 29, 265 (2010).
5. M. Schoßig, C. Bierögel, W. Grellmann, and T. Mecklenburg. Polym. Test., 27, 893 (2008).
6. X. Xiao. Polym. Test., 27, 164 (2008).
7. J.C. Viana, N. Billon, and A.M. Cunha. Polym. Eng. Sci., 44, 1522 (2004).
8. M. Fujiyama and K. Azuma. J. Appl. Polym. Sci., 23, 2807 (1979).
9. J. Housmans, M. Gahleitner, G.W.M. Peters, and H.E.H. Meijer. Polymer, 50, 2304 (2009).
10. C. Shen, G. Zheng, C. Liu, Y. Wang, J. Chen, and X. Peng. J. Macromol. Sci. Part B, 48, 439 (2009).

11. J.C. Viana. *Polymer*, 45, 993 (2004).
12. M.M. Favaro, M.C. Branciforti, and R.E.S. Bretas. *Mater. Res.*, 12, 455 (2009).
13. R. Mendoza, G. Régnier, W. Seiler, and J. Lebrun. *Polymer*, 44, 3363 (2003).
14. T.B. Van Erp, L.E. Govaert, and G.W.M. Peters. *Macromol. Mater. Eng.*, 298, 348 (2013).
15. J. Varga and J. Karger-Kocsis. *J. Polym. Sci. Part B Polym. Phys.*, 34, 657 (1996).
16. C. Tribout, B. Monasse, and J.M. Haudin. *Colloid Polym. Sci.*, 274, 197 (1996).
17. R. Čermák, M. Obadal, P. Ponižil, M. Polášková, K. Stoklasa, and J. Hecková. *Eur. Polym. J.*, 41, 1838 (2005).
18. C. Zhang, G. Liu, Y. Song, Y. Zhao, and D. Wang. *Polymer*, 55, 6915 (2014).
19. R. Čermák, M. Obadal, P. Ponižil, M. Polášková, K. Stoklasa, and J. Hecková. *Eur. Polym. J.*, 42, 2185 (2006).
20. T. Parenteau, G. Ausias, Y. Grohens, and P. Pilvin. *Polymer*, 53, 5873 (2012).
21. P. Tordjeman, C. Robert, G. Marin, and P. Gerard. *Eur. Phys. J. E.*, 4, 459 (2001).
22. J.C. Viana. *Polymer*, 46, 11773 (2005).
23. G. Kalay and M. J. Bevis. *J. Polym. Sci.*, 35,241 (1997).
24. A.M. Cunha, J.S. Godinho, and J.C. Viana. In *Structure Development During Polymer Processing*, 255 (2000).
25. Y. Duan, A. Saigal, R. Greif, M.A. Zimmerman. *Polym. Eng. Sci.*, 43, 112 (2003).
26. C. G´Sell, J.J. Jonas. *J. Mat. Sci.*, 14, 583 (1979).
27. M. Zrida, H. Laurent, G. Rio, S. Pimbert, V. Grolleau, N. Masmoudi, and C. Bradai. *Comput. Mater. Sci.*, 45, 516 (2009).
28. F. Bédoui, J. Diani, and G. Régnier. *Polymer*, 45, 2433 (2004).
29. J.S. Godinho, A. Cunha, and R.J. Crawford. *Plast. Rubber Compos.*, 29, 329 (2000).
30. C.N. Barbosa, R. Simoes, M. Franzen, and J.C. Viana. *Journal of Materials Science*, 48, 2597 (2013).
31. C.N. Barbosa, F. Carvalho, J.C. Viana, M. Franzen, and R. Simoes. *Int. J. Adv. Manuf. Technol.*, 77, 873 (2015).

## 2. COMPREHENSIVE STUDY ON THE RELATIONSHIPS BETWEEN PROCESSING, MICROSTRUCTURE AND MECHANICAL PROPERTIES OF INJECTION MOLDED POLYPROPYLENES

This chapter is based on the scientific paper published elsewhere:

C.N. Barbosa, R. Simoes, M. Franzen, T. Baranowski, and J.C. Viana. Polym. Eng. Sci., DOI 10.1002/pen.24650 (2017).

### **Abstract**

The relationships between the morphologies of different injection molded polypropylenes and their tensile properties measured at high strain rate were investigated. A threefold systematic analysis is proposed by establishing the following relationships: (i) processing-morphology; (ii) processing-mechanical properties; and (iii) morphology-mechanical properties. Experimental techniques were employed to assess the structural heterogeneity of the moldings, namely: polarized light microscopy (skin thickness), wide-angle X-ray scattering (crystallinity, molecular orientation and polymorphism of the skin layer), and differential scanning calorimetry (bulk crystallinity). High velocity tensile tests (1m/s) were recorded by a high speed camera that runs 20k frames per second. The influence of multiple processing variables on the morphology and properties was studied adopting a structured statistical approach by means of two statistical tools: analysis of variance and response surface methodology. The most important molding variables and their interactions were identified. Straightforward relationships between the morphology and the tensile properties were established by fitting the experimental data to polynomial equations, using a least-square minimization procedure. The melt temperature was identified as the most significant variable for the development of the morphologies and the mechanical response of the moldings. The skin thickness, its crystallinity and molecular orientation (flow direction) influence, to a certain degree, the tensile properties of the materials.

## 2.1 Introduction

Injection molding (IM) is one of the most important manufacturing processes for producing thermoplastic parts for a wide variety of industries and markets (e.g. automotive). Due to global competition, the IM companies face continuously increasing requirements to deliver high quality parts (aesthetics, mechanical, etc.) while lowering production costs. At the shop floor level, those requirements are highly dependent on the IM process settings (processing temperatures, injection velocity, cooling time, pressure, etc.).

For a given material (e.g. polypropylene, PP) the definition and combination of the molding parameters induce a specific morphology across the thickness and along the entire domain of the part [1-6]. Also, and as a result of the developed morphology, the molding parameters will determine the mechanical response of the material [7-12]. Under well-defined service conditions, namely temperature, load case and strain rate, the mechanical performance of an injection molded part is basically a result of the fundamental molecular nature plus the process induced morphology [13-20]. Despite the huge amount of information on PP in the scientific literature, few studies were found in what concerns the mechanical behavior of PP injection molded parts tested at high strain rates, particularly in the setting of identifying processing-microstructure-properties relationships [21, 22].

The complex relationships among processing conditions, morphology and mechanical properties of injection molded thermoplastics is a very important research area, both in industrial and academic settings. Design of experiments (DOE) and other techniques have been used as powerful approaches to achieve increased understanding of the IM process, again contributing to significant improvements in product and process quality while decreasing the manufacturing costs [23-28].

As aforementioned, studies have been conducted to obtain information on the morphology of moldings and to correlate the observations with the processing conditions and with the mechanical properties. Normally, the applied techniques do not offer a broader and systematic approach to tackle consistently the issue of processing-morphology-properties relationships in IM. Almost all existing research is focused on the effect of individual variables on the final morphological features and mechanical properties, but not in the systematical effect caused by multiple factors (e.g., considering interactions between those processing variables). Thus, current predictive capabilities based on the literature are inaccurate and inadequate.

The current work aims at improving state-of-the-art knowledge of the correlation between processing, morphology and properties of injection molded PP. The objective is twofold. First, an advanced DOE technique – response surface methodology (RSM) – and analysis of variance (ANOVA) are applied to

systematically vary the molding window and evaluate (qualitatively and quantitatively), supported on a statistical approach, the interactions of multiple variables (processing temperatures, injection velocity, and packing pressure) and their interrelations with (i) structure development (skin ratio, molecular orientation, crystallinity and  $\beta$ -phase content) and (ii) mechanical response (initial modulus, stress at yield and strain at break) under tensile loading at high strain rates. Second, straightforward relationships between the envisaged morphological features and the mechanical properties are depicted by response surfaces obtained by fitting the experimental data to polynomial equations, using a least-square minimization procedure. The specimens tested were injection molded cylindrical tensile bars made of two PP grades (from different suppliers) typically used in automotive interior applications, to investigate universality of the identified relationships.

## 2.2 Experimental

### 2.2.1 Materials and test specimen geometries

Two commercial unreinforced isotactic polypropylenes (iPP), coded as PP07 and PP81, were used to produce specimens through IM which were subsequently characterized. Due to confidentiality restrictions, the specific PP grades cannot be disclosed. PP81 presents a melt flow index, MFI, of 10 g/600 s and solid density,  $\rho_s$ , of 0.911 g/cm<sup>3</sup>, and PP07 has a MFI of 15 g/600 s and a  $\rho_s$  of 0.891 g/cm<sup>3</sup>. The melt density,  $\rho_m$ , of both materials is actually equivalent.

The molding is an axisymmetric dumbbell-like specimen of 3 mm diameter and 28 mm constant circular cross-section, with a total length of 60 mm, laterally gated in one of the specimen's rectangular heads.

### 2.2.2 IM experimental design

An IM machine with clamping force capacity of 850 kN and maximum hydraulic injection pressure of 160 bar was used to produce all specimens. The IM boundary conditions were assessed through molding window analysis (MWA) available in the Autodesk Moldflow Insight software package. An example of MWA can be found elsewhere [29]. Based on the MWA results, the processing window was established and a DOE plan was created to further investigate the influence of the molding parameters on the morphology and mechanical properties of the specimens.

The current DOE plan was based on the RSM, adopting a Face Central Composite (FCC) design. It is a very efficient method to estimate linear (1st-order) and non-linear terms (interaction between two terms:

two factor interactions, 2FI; and quadratic factor,  $X^2$ ), becoming the most commonly used response surface designed experiment [27, 30]. This statistical methodology helps to identify the most significant terms (IM variables) and tradeoffs that affect the morphological features and the mechanical properties, supporting in this way the optimization of the process settings.

The following processing conditions were selected as variables, factors or model terms: injection velocity,  $v_i$ ; injection temperature,  $T_i$ ; mold temperature,  $T_w$ ; and holding pressure,  $P_h$  (applied for 5 s). These factors were varied in three levels: minimum (coded as “-1”); center (coded as “0”); and maximum (coded as “+1”). A total of 25 different processing conditions were completed, as described in Table 2-1.

Table 2-1. Injection molding experimental plan for the tested materials (FCC design).

Experiment	$v_i$		$T_i$		$T_w$		$P_h$ (*)	
	level	mm/s	level	°C	level	°C	Level	MPa
E01	-1	10	-1	200	-1	10	-1	7
E02	+1	100	-1	200	-1	10	-1	7
E03	-1	10	+1	280	-1	10	-1	7
E04	+1	100	+1	280	-1	10	-1	7
E05	-1	10	-1	200	+1	70	-1	7
E06	+1	100	-1	200	+1	70	-1	7
E07	-1	10	+1	280	+1	70	-1	7
E08	+1	100	+1	280	+1	70	-1	7
E09	-1	10	-1	200	-1	10	+1	42
E10	+1	100	-1	200	-1	10	+1	42
E11	-1	10	+1	280	-1	10	+1	42
E12	+1	100	+1	280	-1	10	+1	42
E13	-1	10	-1	200	+1	70	+1	42
E14	+1	100	-1	200	+1	70	+1	42
E15	-1	10	+1	280	+1	70	+1	42
E16	+1	100	+1	280	+1	70	+1	42
E17	-1	10	0	240	0	40	0	25
E18	+1	100	0	240	0	40	0	25
E19	0	55	-1	200	0	40	0	25
E20	0	55	+1	280	0	40	0	25
E21	0	55	0	240	-1	10	0	25
E22	0	55	0	240	+1	70	0	25
E23	0	55	0	240	0	40	-1	7
E24	0	55	0	240	0	40	+1	42
E25	0	55	0	240	0	40	0	25

(\*) pressure at the nozzle.



### 2.2.3 Morphology characterization

All materials have been tested extensively with the following described methods: polarized light microscopy (PLM), wide-angle X-ray scattering (WAXS), differential scanning calorimetry (DSC), and mechanical characterization (tensile-impact tests at 1 m/s).

#### a. Polarized light microscopy

PLM was used to assess the skin-to-core thickness ratio, or simply the skin ratio,  $S_a$ . Thin layers of about  $17\ \mu\text{m}$  were microtomed transversely to the flow direction from approximately the center of the cylindrical region, then immersed in a cold cure epoxy resin, as schematized in Figure 2-1, and cured for at least 48 h at room temperature. Prior to PLM analyses, the samples were placed on *Canada balsam* between glass slides for at least 48 h at room temperature so that any refractive-index mismatch was eliminated. The microscopy analyses were carried out using an Olympus BH-2 microscope coupled with an image analyzer system Leica Quantimed 500C.

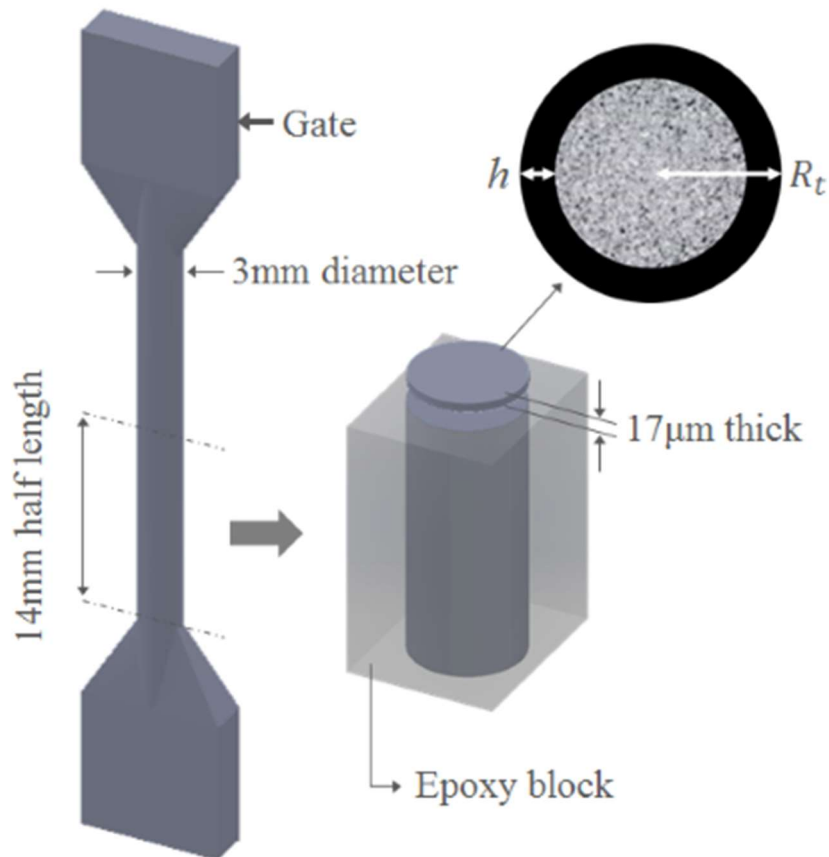


Figure 2-1. Representation of the skin/core microscopy analysis procedure.

The skin region has been defined as the external darkest zone when the specimen is under polarized light observation, as schematically represented in Figure 2-1. Its thickness was measured in 10 points along the perimeter and a representative average value was calculated.  $Sa$  was defined as the ratio of the crosssectional areas of the skin to the total sample, as represented by Equation 2-1.  $R_t$  is the representative radius of the bar samples and  $h$  is the skin thickness.

$$Sa = \frac{2R_t h - h^2}{R_t^2} \quad \text{Equation 2-1}$$

#### b. Wide-angle X-ray scattering

The level of molecular orientation,  $\Omega_s$ , index of crystallinity,  $\chi_s$ , and amount of b-phase,  $\beta_{300}$ , of the skin was assessed by WAXS. The crystalline structure of the skin samples was determined in a reflection mode on a Bruker AXS D8 Discover diffractometer with a Cu-K $\alpha$  radiation ( $\lambda = 1,54060 \text{ \AA}$ ), in  $\theta$ - $2\theta$  mode ranging from  $5^\circ$  to  $30^\circ$  in steps of  $0.04^\circ$  and an integration time of 1 s. The scans were taken parallel to the flow direction. The X-ray beam was directly irradiated against the center of the cylindrical region of the bars and the diffractograms are the result of the X-rays interaction with the whole skin region (i.e., skin surface, transition zones and part of the core [2]) of the molded bars. The typical penetration depth is about  $700 \mu\text{m}$  [31].

The linear equatorial WAXS profiles were treated for digital filtering and enhancement, baseline processing and spectra deconvolution were carried out using dedicated software. A Gaussian convolution smoothing was applied to the raw data. The curves were then corrected for background scattering by subtracting the background line and a spectroscopy Gaussian function was used as a deconvolution (peak separation) method to avoid overlapped peaks.

The  $\chi_s$  was calculated according to the Hermans-Weidinger method [5, 17] and represented by Equation 2-2. The  $S_{total}$  stands for the total area below the intensity scan curve consisting of crystalline peaks and amorphous halo. The  $S_{cryst}$  defines the specific area of the crystalline peaks.

$$\chi_s = \frac{S_{cryst}}{S_{total}} \quad \text{Equation 2-2}$$

The value of  $\Omega_s$  was evaluated by calculating two orientation indices,  $A_{110}$  and  $A_{130}$ , on the relative peak intensities of the  $\theta$ - $2\theta$  scans. These indices are related to the orientation of  $\alpha$ -crystallites in the flow direction. The  $I_{hkl}$  is the peak height (or intensity) of the correspondent  $hkl$  planes [18]. For highly oriented samples,  $A = 1$ ; otherwise  $A < 1$ . The  $\Omega_s$  was evaluated as the average between both orientation indices,  $A_{110}$  and  $A_{130}$ , as shown in Equation 2-3. Table 2 presents the diffracted angles of the most relevant crystalline peaks and the correspondent Miller indices and crystal form for an iPP, as reported elsewhere [2].

$$\Omega_s = \frac{\frac{I_{110}}{I_{110}+I_{111}+I_{131}+041} + \frac{I_{130}}{I_{130}+I_{111}+I_{131}+0}}{2} = \frac{A_{110}+A_{130}}{2} \quad \text{Equation 2-3}$$

Table 2-2. Diffracted angle,  $2\theta$ , and the correspondent Miller indices and crystal form of iPP.

$2\theta$ (°)	Crystalline plane ( $hkl$ )	iPP phase
14.1	110	$\alpha$
16.1	300	$\beta$
16.8	040	$\alpha$
~17.5	Amorphous halo	Amorphous
18.5	130	$\alpha$
21.2	111	$\alpha$
21.8	041+131 (301)	$\alpha$ ( $\beta$ )
25.5	160 (060)	$\alpha$
28.4	220	$\alpha$

The  $\beta_{300}$  index represents the amount of  $\beta$ -spherulites, where pure  $\beta$ -PP would yield  $\beta_{300} = 1$ , and can be calculated according to the method of Turner-Jones et al. [5, 18], represented by Equation 2-4.

$$\beta_{300} = \frac{I_{300}}{I_{300}+I_{110}+I_{040}+I_{130}} \quad \text{Equation 2-4}$$

### c. Differential scanning calorimetry

DSC was used to determine the crystalline content (given as % of bulk crystallinity,  $\chi_b$ ) of the samples. The measurements were performed in a DSC 200 F3 Maia<sup>®</sup> differential scanning calorimeter, at a heating rate of 10° C/min, in the temperature range from 30 °C to 200 °C. Samples within 7±1 mg were cut out

from approximately the center of the cylindrical region of the specimens fully through their thickness (bulk sample).

The enthalpy of fusion,  $\Delta H_m$ , was calculated as the area below the DSC thermogram, between fixed lower and upper limit temperatures,  $T_{lower} = 120$  °C and  $T_{upper} = 185$  °C, respectively. At least, two samples of each studied microstructure were tested. The  $\chi_b$  was calculated from the measured  $\Delta H$  values according to Equation 2-5 [12]. The  $\Delta H_m^x$  is the theoretical enthalpy of fusion of a single polymer crystal. In the case of PP,  $\Delta H_m^{PP} = 148$  J/g was assumed [32].

$$\chi_b = \frac{\Delta H_m}{\Delta H_m^x} \times 100 \quad \text{Equation 2-5}$$

#### 2.2.4 Mechanical characterization

Prior to any test, the tensile bars were kept conditioned in a laboratory using a standard environment (atmosphere of  $23 \pm 2$  °C and  $50 \pm 5$  % relative humidity), for at least 3 weeks. The dynamic tensile tests were conducted under those standard conditions at 1 m/s (nominal strain-rates of about  $36$  s<sup>-1</sup>) in a servo-hydraulic Zwick-Roell Amsler HTM3712 testing machine with a load capacity of 25 kN.

All tests were recorded using a Photron APX-RS high-speed video system at 20.000 frames per second with a resolution of 384 x 304 pixels. Two halogen lamps of 1,000 W were synchronized with the servo-hydraulic machine and high-speed camera to record in perfect clarity with negligible motion blur.

The initial force-displacement curves were converted into true stress–true strain curves,  $\sigma^t - \varepsilon^t$ . The variation of the circular cross-section of the specimens in the neck zone during the dynamic tensile test was adequately captured by the videography system. The recorded films were fragmented into frames and the local strain and neck area reduction were tracked and measured using image analyzer software. From the  $\sigma^t - \varepsilon^t$  curves the initial modulus,  $E$ , stress at yield,  $\sigma_y$ , and strain at break,  $\varepsilon_b$ , were calculated.  $E$  was measured in the linear slope of the curve between 0.006 and 0.01 mm/mm. The  $\sigma_y$  was defined as the maximum stress obtained from the nominal stress–strain curves with the localized area correction. The  $\varepsilon_b$  is simply the strain specified at the sample break from the  $\sigma^t - \varepsilon^t$  curves. Six samples were tested per condition, for each material, and the average results were used for analysis.

## 2.3 Results and discussion

The ANOVA statistical results include the percentage of contribution,  $\%p$ , of each IM variable on the specific response (morphology and property), the coefficient of determination of the model,  $Model R^2$ , and the adjusted and predicted coefficient of determination of the model,  $Adj.R^2$  and  $Pred.R^2$ , respectively. The statistical analyses were performed according to the procedure for choosing model(s) suggested in [33], that is, the model selection criterion follows the highest order polynomial that maximizes  $Adj.R^2$  and  $Pred.R^2$ . A rule of thumb is that  $Adj.R^2 - Pred.R^2 < 0.2$  to obtain a statistically significant model and  $Adj.R^2 \geq 0.7 \wedge Pred.R^2 \geq 0.7$  to obtain a model that can determine precisely the optimum molding parameter settings, thus applied for prediction purposes.

### 2.3.1 Influence of the IM conditions on morphologies

#### a. Skin-to-core thickness ratio, $Sa$

Figure 2-2 shows examples of microtomed samples taken from PP07 bars. Whereas the skin is black and shows no structure, the crystalline core layer appears as a light granular area. Figure 2-2a and b shows the thickest and thinnest skin ratio samples for PP07, respectively.

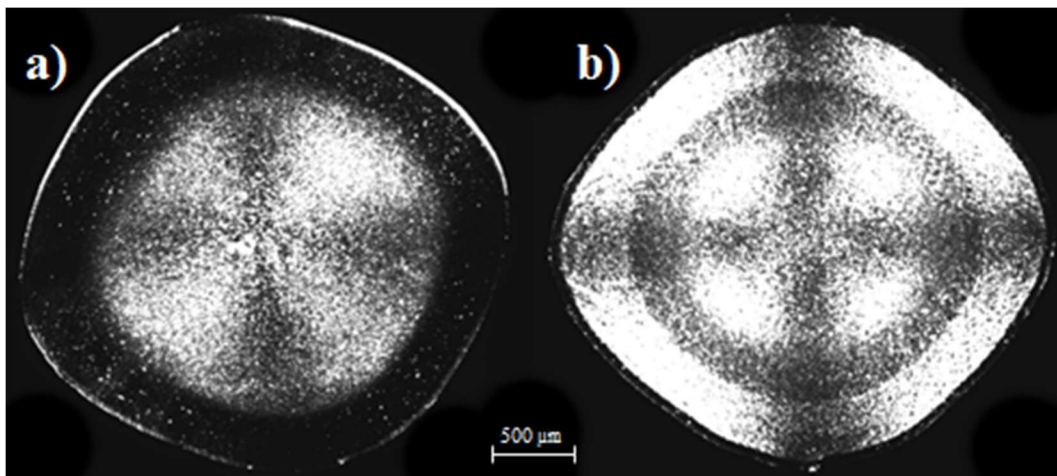


Figure 2-2. Transversal sections from microtomed bar samples: (a) PP07 bars, experiment E09; and (b) PP07 bars, experiment E16.

The skin ratio of the PP81 moldings was more complicated to measure due to the lack of contrast. The non-roundness shape of the specimens results from the mold tooling. Also, a Maltese cross-like pattern

is observed, typical of polymer spherulites. This extinction pattern may indicate a radial distribution of birefringent structures (e.g., spherulites), an optical pattern related to the sizes of the scattering entities, or just an optical artifact [34].

ANOVA was carried out to identify the influence of each IM parameter on  $Sa$ . Figure 2-3 shows the relative effect of the significant processing variables on  $Sa$  and summarizes the ANOVA statistical results. This statistical analysis was run with a confidence level of 99%. The % of residuals are irrelevant (PP07) or small (PP81) and the  $R^2$  values are very satisfactory. Consequently, the identified significant terms and the respective effects on the  $Sa$  response consider most of the sources of variation in the process.

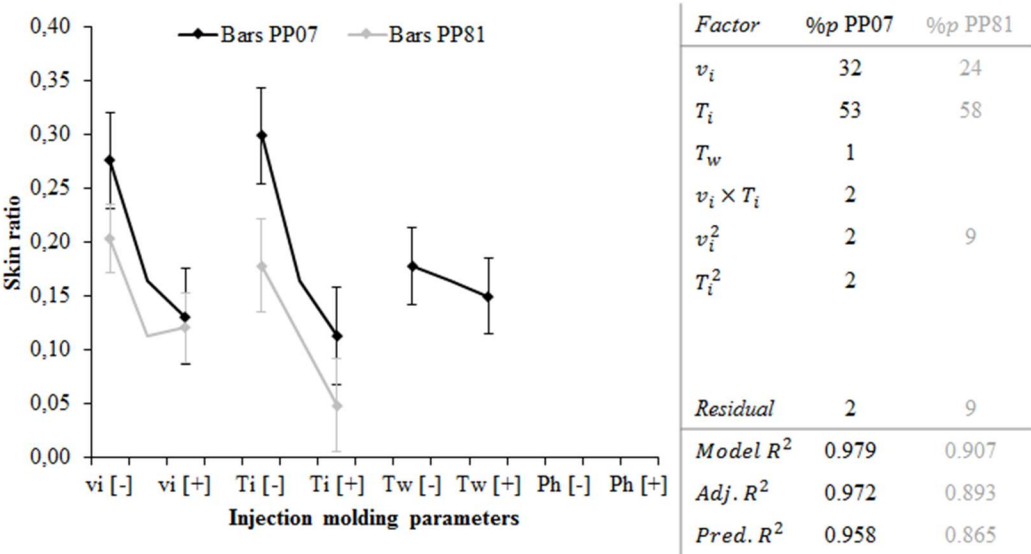


Figure 2-3. ANOVA summary of the effect of the significant IM parameters on the  $Sa$ .

$Sa$  is basically determined by  $v_i$  (%p  $\approx$  32% for PP07 and 24% for PP81) and  $T_i$  (%p  $\approx$  53% for PP07 and 58% for PP81).  $T_w$  has a small %p  $\approx$  2% for PP07 and negligible for PP81.  $P_h$  has no effect on the  $Sa$ , and expectantly on the crystallization development of these materials. The non-linear (2FI and  $X^2$ ) effects on the variations of  $Sa$  are minor, thus intentionally not shown. An interaction [ $v_i \times T_i$ ] was found for PP07, however with relative low contribution (%p  $\approx$  2%). Also, the same variables display a quadratic effect on  $Sa$  with a %p  $\approx$  2%. In the case of PP81, the quadratic effect of  $v_i$  is relatively higher with a %p  $\approx$  9% but no interactions were found for this material.

The skin layer contains highly oriented and crystalline form structures because the flow induced orientation does not have enough time to relax before crystallization occurs. According to the phenomenological model presented in [35, 36], the skin thickening is promoted by lower  $t_r$  (time allowed

for relaxation before reaching the crystallization temperature of the material) and higher  $\lambda$  (relaxation time of the material). Therefore, thicker skins are at great extent determined by lower  $T_i$  (lower  $t_r$ , higher  $\lambda$ ) and  $v_i$  (lower  $T_i$ , by consequence of lower viscous dissipation).

**b. Index of crystallinity of the skin,  $\chi_s$**

The processing parameters that mostly affect the development of the  $\chi_s$  are presented in Figure 2-4, which also summarizes the ANOVA statistical results and illustrates the comparative effect of each parameter on  $\chi_s$ . This analysis was run with a 99% confidence level. ANOVA of PP81 shows good results in terms of  $R^2$  and relative small residuals. The % of residuals is rather relevant in the case of PP07 (35%) and, despite the statistically significance of the model, the  $R^2$  values revealed that the significant terms identified and their effects do not consider all the sources of variation in the process.

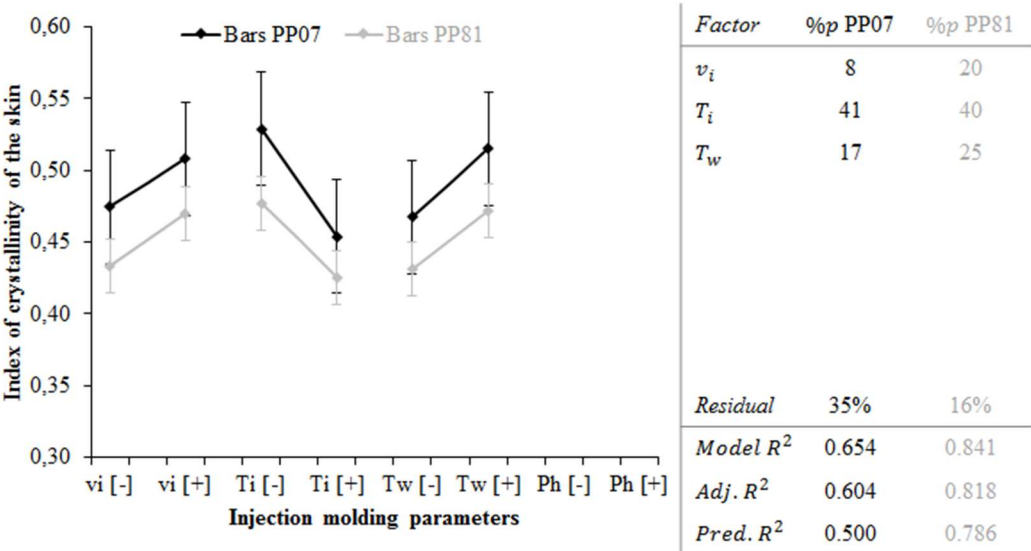


Figure 2-4. ANOVA summary of the effect of the significant IM parameters on  $\chi_s$ .

Particularly for the PP07 bars,  $\chi_s$  is determined by  $T_i$  and  $T_w$  with a  $\%p \approx 41\%$  and  $17\%$ , respectively. Likewise,  $\chi_s$  of the PP81 bars is dominated by the processing temperatures with a  $\%p \approx 40\%$  and  $25\%$  for  $T_i$  and  $T_w$ , respectively. The  $v_i$  has a significant effect on  $\chi_s$  for both materials, but more noticeable for PP81 ( $\%p \approx 20\%$ ). For both materials,  $P_h$  has no effect on the crystallinity of the skin and no interactions between processing variables were found.

Generally,  $\chi_s$  increases by combining low  $T_i$  and high  $T_w$  levels with high  $v_i$ . Low  $T_i$  and high  $v_i$  may result in a higher viscous dissipation, that combined with the high shearing effects (affecting flow induced crystallization), increase  $\chi_s$ . These high thermal and shear levels at the skin are promoted by high  $T_w$ .

### c. Molecular orientation of the skin, $\Omega_s$

To check the WAXS data quality, a scatterplot was used to represent the relationship between the intensity of both planes ( $I_{110}$  and  $I_{130}$ ) that are oriented perpendicularly to the c-axis of the  $\alpha$ -form crystallites. According to [18], the ratio between both these intensities should be nearly 0.5. Values of 0.49 ( $R^2 = 0.88$ ) and 0.41 ( $R^2 = 0.81$ ) were found for the PP07 and PP81, respectively, and considered valid.

The identification of the IM parameters affecting the development of  $\Omega_s$  was statistically analyzed through the ANOVA method, with a 99% confidence level. The statistical results are shown in Figure 2-5. Relatively high statistical residuals were found for PP07 (28%) and PP81 (23%), revealing some unidentified sources of variation in the process or a large experimental error on the measurements. Nevertheless, the models of both materials are significant and the optimum (most important) parameters are identified.

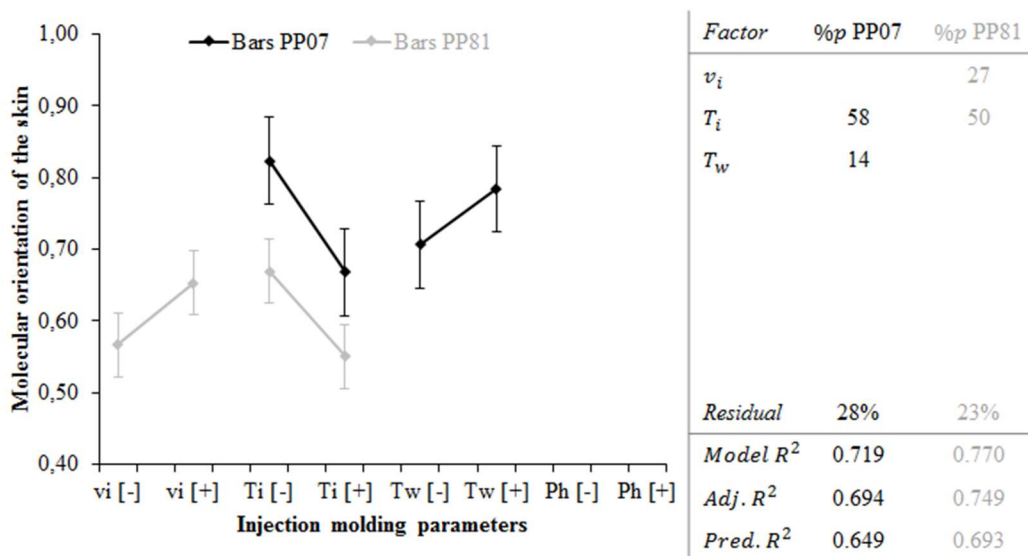


Figure 2-5. ANOVA summary of the effect of the significant IM parameters on  $\Omega_s$ .

The  $\Omega_s$  is mostly determined by  $T_i$  with a %p  $\approx$  58% (PP07) and 50% (PP81). Additionally,  $\Omega_s$  is influenced by  $T_w$  (%p  $\approx$  14%) for the PP07 bars, and by  $v_i$  (%p  $\approx$  27%) for the PP81 bars. In the case of PP07 bars,  $\Omega_s$  increases by combining low  $T_i$  with high  $T_w$ . Conversely, for PP81 bars,  $\Omega_s$  is maximized by high  $v_i$  and low  $T_i$ . The  $v_i$  parameter is rather significant for PP81 due to the higher



viscosity compared to PP07, leading to higher flow induced orientation. The orientation of PP81 moldings results from the combination of shear and thermal levels; conversely, the orientation of PP07 is more dependent on the thermal levels (processing temperatures). For both PP grades,  $P_h$  has no effect on  $\Omega_s$  and no significant interactions between processing variables are identified.

The differences between the two materials are related to their viscosity and relaxation times. The PP81 holds lower MFI, thus higher viscosity and relaxation time than PP07. For the same thermomechanical environment, materials with higher  $\lambda$  show lower in-flow molecular orientation ( $\Omega_s^{PP07} > \Omega_s^{PP81}$ ).

#### d. $\beta$ -phase content of the skin, $\beta_{300}$

Figure 2-6a summarizes the ANOVA statistical results and compares the effect of the significant IM parameters on  $\beta_{300}$ . The statistical analysis was run with a confidence level of 99% for PP07 and 90% for PP81. The  $R^2$  values observed for the PP81 bars are rather low ( $\sim 0.4$ ) and the residuals are much higher (62%) when compared to PP07. In this way, the weak statistics discloses the inaccuracy of the PP81 model for prediction purposes. The  $\beta_{300}$  values observed in the PP81 moldings are definitely small (in average, 8 times less than those observed for PP07 bars) and the experimental error is within the experimental variation; therefore, PP81 data will not be considered for discussion.

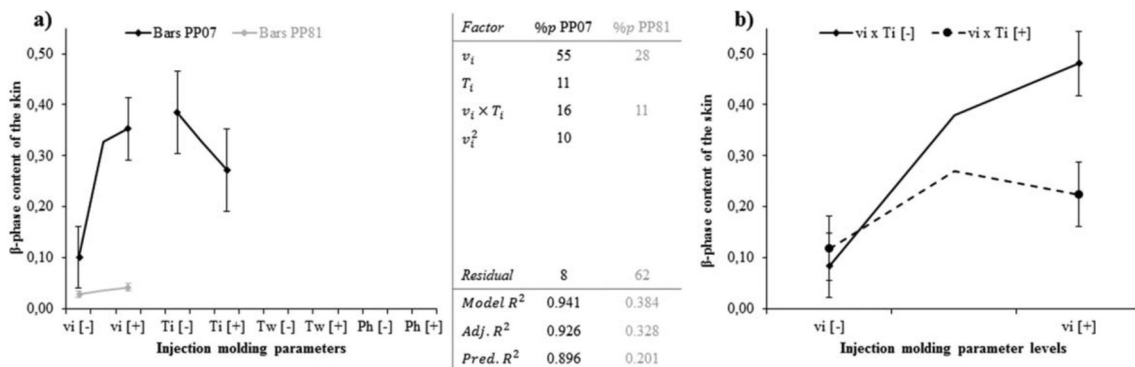


Figure 2-6. ANOVA summary of (a) the effect of the significant IM parameters on  $\beta_{300}$ , and (b) two factor interaction effects  $[v_i \times T_i]$  evaluated on  $\beta_{300}$  of PP07 bars.

For PP07 bars,  $\beta_{300}$  is mostly determined by  $v_i$  with a  $\%p \approx 55\%$  (PP07 bars) followed by  $T_i$  with  $\%p \approx 11\%$  and a 2<sup>nd</sup>-order dependence on  $v_i$  ( $\%p \approx 10\%$ ). The interaction  $[v_i \times T_i]$  is also relevant ( $\%p \approx 16\%$ ). This is depicted in Figure 2-6b. This interaction reveals that the effect of  $v_i$  is higher for low  $T_i$ . The development of  $\beta_{300}$  is favored when the polymer melt is under high shear stress levels (i.e., increased shear rate,  $\uparrow v_i$ , and viscosity,  $\downarrow T_i$ ). For high  $T_i$ , the effect is similar although less pronounced.

In fact, particularly for the PP07 bars, a significant pattern is detected: the highest  $\beta_{300}$  values are found for conditions with higher flow rates and lower  $T_i$  (E02, E06, E10, and E14) evidencing the adequate thermomechanical environment for the development of  $\beta$ -PP.

**e. Index of bulk crystallinity,  $\chi_b$**

PP07 bars exhibit a total variation of about 7%, with a minimum value of 0.403 for E17 and a maximum value of 0.433 for E03. The PP81 bars show a total variation of about 6% with a minimum value of 0.458 for E10 and a maximum value of 0.488 for E18. These minor variations can be explained by the fact that both PP grades have a very high crystallization rate. Both PP seem to be insensitive with respect to variations of  $\chi_b$  with the IM conditions.

PP81 bars show, on average,  $\chi_b$  values which are 12% higher than those of the PP07 bars. The two materials have slightly different solid density, which is higher for the PP81 material.

To test the effect of the crystallization rates on the degree of crystallinity of both materials, two simple experiments were carried out: (i) the PP melt was cooled down in liquid nitrogen; and (ii) the PP melt was cooled down at room temperature. It was observed that the % of crystallinity remained within the experimental error observed for the DOE samples. Due to the small variations, no effect of processing conditions on bulk crystallization was considered.

### 2.3.2 Influence of the IM conditions on the tensile properties

**a. Elastic modulus,  $E$**

The contribution of each IM variable on  $E$  was studied through the ANOVA method. Figure 2-7 summarizes the statistical results and compares the effect of each parameter on  $E$ . The statistical analysis was performed under a confidence level of 95%. Relatively high statistical residuals (26%) were found for PP07. However, an acceptable  $R^2$  (near 0.7) was calculated, which means that the model is significant and may be used for prediction purposes. Conversely, the statistical analysis of PP81 bars featured very high residuals (58%) and weak  $R^2$  values. In this case, the identified terms do not result in a robust model able to predict  $E$  accurately. Yet, the model is statistically significant.

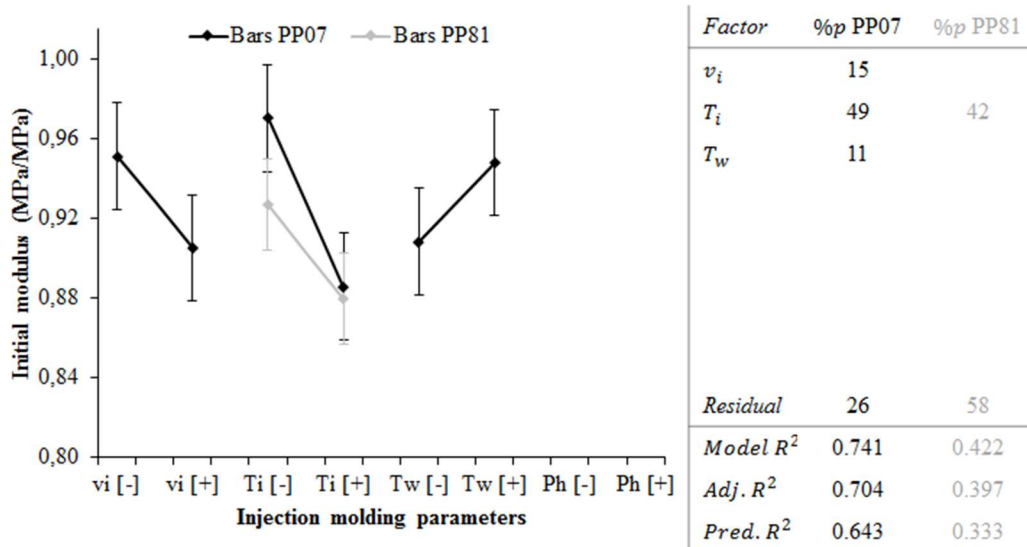


Figure 2-7. ANOVA summary of the effect of the significant IM parameters on  $E$  (normalized values).

For the PP07 bars,  $E$  is mostly governed by  $T_i$  with a  $\%p \approx 49\%$ . Also,  $v_i$  and  $T_w$  are considered significant model terms with  $\%p \approx 15\%$  and  $11\%$ , respectively. It was found that  $E$  increases with low  $T_i$  and  $v_i$ , as well as high  $T_w$  levels. In the case of PP81 bars,  $T_i$  was identified as the significant and unique model term. As had been observed for PP07 bars, low  $T_i$  again lead to high values of  $E$ . Generally, conditions with the lowest levels of  $v_i$  and  $T_i$  (E01, E05, E09, and E13) exhibit the highest  $E$  values. Essentially, a stiffer material is obtained when using lower injection temperature.

#### b. Stress at yield, $\sigma_y$

The contributions of each IM parameter on  $\sigma_y$  for the two PP grades were studied through ANOVA. Figure 2-8 summarizes the statistical results and compares the effect of each parameter on  $\sigma_y$ , for a confidence level of 95%. The statistical residual values (<10%) for both PP grades are small. Both models (PP07 and PP81) are statistically significant and the  $R^2$  values are very satisfactory. As such, this property may be accurately predicted as a function of the IM variables.

In the case of PP07 bars,  $\sigma_y$  is mostly governed by  $T_i$  with a  $\%p \approx 62\%$ . The parameters  $v_i$  and  $P_h$  are also considered significant model terms with a  $\%p \approx 3\%$  and  $12\%$ , respectively. High  $\sigma_y$  is obtained using low levels of  $T_i$  and  $v_i$ , and high  $P_h$ . Also  $T_w$  is considered a significant model term due to its quadratic effect with a  $\%p \approx 12\%$ . In this case,  $\sigma_y$  is improved using intermediate values of  $T_w$ . Moreover, the interaction [ $v_i \times T_i$ ] was identified in this model with a  $\%p \approx 3\%$ , which represents a minor contribution for the overall model response, thus not graphically represented.

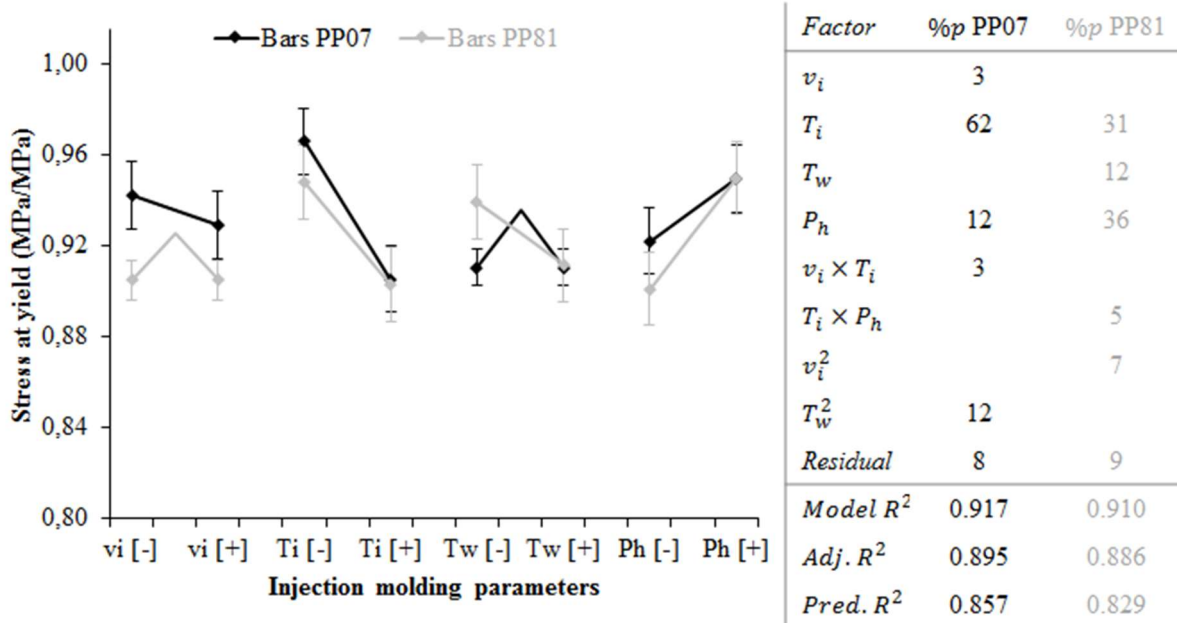


Figure 2-8. ANOVA summary of the effect of the significant IM parameters on  $\sigma_y$  (normalized values).

Regarding the PP81 bars, it was found that  $\sigma_y$  is controlled by  $T_i$  and  $P_h$ , with a %p  $\approx$  31% and 36%, respectively. High  $\sigma_y$  is obtained using low  $T_i$  and high  $P_h$ , as had been observed for the PP07 bars. The interaction [ $T_i \times P_h$ ] was identified in this model with a small %p  $\approx$  5% (also not graphically shown). The  $\sigma_y$  is maximized by combining low  $T_i$  and high  $P_h$ . It was also found that  $T_w$  has a significant effect on  $\sigma_y$ , with a %p  $\approx$  12%. Low  $T_w$  lead to high  $\sigma_y$  values. Finally,  $v_i$  was identified as a significant model term due to its quadratic effect with a %p  $\approx$  7%, and  $\sigma_y$  is improved using intermediate values of  $v_i$ .

### c. Strain at break, $\epsilon_b$

The processing parameters that affect the development of  $\epsilon_b$  can be observed in Figure 2-9a. This figure summarizes the ANOVA statistical results and compares the effect of each parameter on  $\epsilon_b$ . The analysis was carried out under a 95% confidence level. The statistical results for the PP81 bars are better than those obtained for the PP07 bars. The latter show a considerable residual of 44% and relative low  $R^2$ , suggesting that the identified significant model terms do not consider all the sources of variation and, thus, the model should not be used to predict  $\epsilon_b$  of PP07. In the case of PP81, a relative high residual value with a %p  $\approx$  21% was found. However,  $R^2$  values are nearly acceptable (0.7). In this case, the identified terms result in a significant statistical model to predict  $\epsilon_b$  within a certain confidence level.

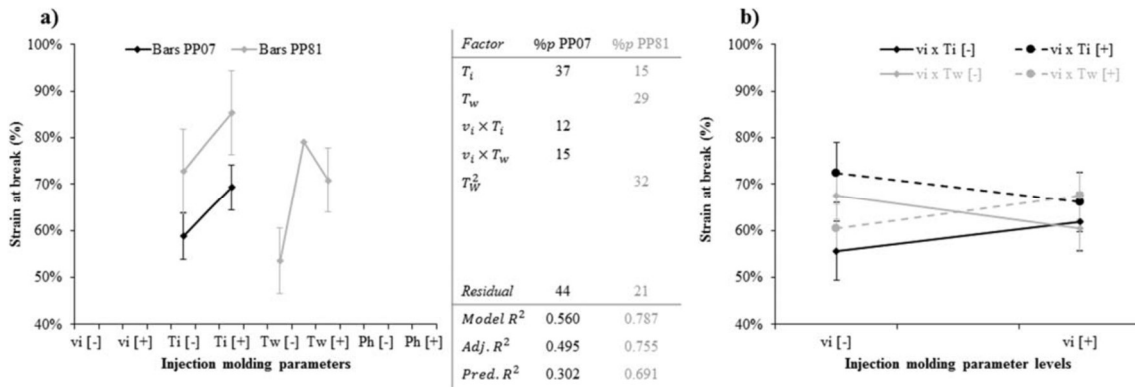


Figure 2-9. ANOVA summary of the effect of the significant IM parameters on  $\sigma_y$  (normalized values).

It was found that  $\varepsilon_b$  is largely driven by  $T_i$  with a  $\%p \approx 37\%$  (PP07). The values of  $\varepsilon_b$  increase with increasing  $T_i$ . Two significant interactions were identified:  $[v_i \times T_i]$  and  $[v_i \times T_w]$ , with a  $\%p \approx 12\%$  and  $15\%$ , respectively. Such effects are represented in Figure 2-9b. The parallelism between the full line and respective dashed line (in color) indicates the interaction effect of the molding parameters. The effect of  $v_i$  may slightly invert depending on the levels of  $T_w$  and  $T_i$ . The value of  $\varepsilon_b$  is maximized with high  $T_i$  and low  $v_i$ . Conversely, higher  $\varepsilon_b$  may be obtained by combining together either low or high levels of  $v_i$  and  $T_w$ . Finally,  $P_h$  does not contribute to the  $\varepsilon_b$  response for PP07 bars.

Concerning PP81 bars,  $\varepsilon_b$  is mostly determined by the processing temperatures with a  $\%p \approx 15\%$  for  $T_i$  and  $29\%$  for  $T_w$ . It was found that  $T_w$  presents an additional contribution due to the quadratic effect, with a  $\%p \approx 32\%$ . The effect of  $T_w$  is stronger at low levels than at high levels, being maximized for the intermediate values of  $T_w$ . Conversely,  $P_h$  does not contribute to the  $\varepsilon_b$  response of the PP81 bars.

It should be noted that  $\varepsilon_b$  is somehow the most difficult tensile property to characterize and to predict, which is largely due to the chaotic nature of the fracture mechanisms. In general terms, our findings reveal that  $P_h$  has absolutely no effect on  $\varepsilon_b$ . The values of  $\varepsilon_b$  increase (for the two PP grades) with high  $T_i$  levels. Also,  $T_w$  was found to be considerably more significant for PP81 than PP07. Conversely,  $v_i$  is rather more significant for PP07 than for PP81.

## 2.4 Comprehensive summary of structure-processing-mechanical properties relationships

To gain a fundamental understanding of the relationships between the structure and the properties, a threefold systematic analysis is suggested: (i) processing-morphology; (ii) processing-mechanical properties; and (iii) morphology-mechanical properties. The latter are depicted by means of response surfaces.

### 2.4.1 Processing-morphology relationships analysis

Table 2-3 shows that  $T_i$ ,  $v_i$ , and  $T_w$  (ranked in descending order of relevance) are the most significant parameters with respect to the morphology results. The value of  $P_h$  has a marginal effect. In the case of  $\beta_{300}$  and  $\chi_b$ , the % $p$  of the non-linear effects (2FI and  $X^2$ ) may be considered relevant. Due to the relative low statistical significance (except for  $\beta_{300}$  of the PP07 bars) identified by the *Model R<sup>2</sup>* of  $\beta_{300}$  and  $\chi_b$ , this section focus only on  $Sa$ ,  $\chi_s$ , and  $\Omega_s$ .

Table 2-3. Summary of the linear (1<sup>st</sup>-order) and non-linear ( $X^2$  and 2FI) effects of the processing conditions on the selected morphologies (▲ increase and ▼ decrease).

Factor	▲ $Sa$		▲ $\chi_s$		▲ $\Omega_s$		▲ $\beta_{300}$		▲ $\chi_b$	
	PP07	PP81	PP07	PP81	PP07	PP81	PP07	PP81	PP07	PP81
$v_i$	▼▼	▼▼	▲	▲▲		▲▲	▲▲▲	▲▲	▲▲	
$T_i$	▼▼▼	▼▼▼	▼▼▼	▼▼▼	▼▼▼	▼▼▼	▼			
$T_w$	▼		▲▲	▲▲	▲					▲
$P_h$									▲	
2FI	(2)						(16)	(11)	(19)	(43)
$X^2$	(4)	(9)					(10)		(12)	
Resid.	(2)	(9)	(35)	(16)	(28)	(23)	(8)	(62)	(46)	(50)
$R^2$	0.979	0.907	0.654	0.841	0.719	0.770	0.921	0.384	0.540	0.499

Data between parenthesis stand for the % $p$ .

The selected morphologies are mostly controlled by the  $T_i$  (>50% in the case of  $Sa$  and  $\Omega_s$ , and 40% for  $\chi_s$ ). Thicker, more crystalline and more highly oriented skin layers are obtained with lower  $T_i$  levels. It was also found that  $v_i$  imparts a significant contribution; however, it influences  $Sa$  in an opposite manner to that of  $\chi_s$  and  $\Omega_s$ . Thicker skins are promoted by lower  $v_i$ , but  $\chi_s$  and  $\Omega_s$  are maximized for higher  $v_i$  values, mostly in the PP81 samples. As far as  $T_w$  is concerned, it influences mostly  $\chi_s$ . A more crystalline skin is developed using high  $T_w$ . Also,  $T_w$  is still important for  $\Omega_s$  in PP07 bars; in this case, high  $T_w$  leads to high  $\Omega_s$ .

### 2.4.2 Processing-mechanical properties relationships analysis

Table 2-4 lists the significant molding parameters for the studied tensile properties. The *Model R<sup>2</sup>* parameter exhibits reasonable values. Unexpectedly, statistics reveal a relative low  $R^2$  for  $E$  in the case of the PP81 grade. Basically, the most relevant processing parameter is  $T_i$ ; however, with a small % $p$  for  $\varepsilon_b$ . This is more evident for the PP07 bars. The modulus ( $E$ ) and yield strength ( $\sigma_y$ ) of both materials

are improved by lowering  $T_i$ . Conversely, the strain at break ( $\varepsilon_b$ ) increases by increasing  $T_i$ . This confirmed it is not possible to improve all material properties simultaneously. It was found that  $P_h$  exhibits significant %p for  $\sigma_y$  in the case of both materials, although more strongly in the case of PP81. High levels of  $P_h$  lead to high  $\sigma_y$ . Also,  $T_w$  contributes to the changes in  $E$  of the PP07 bars, and in  $\sigma_y$  and  $\varepsilon_b$  of the PP81 bars. Regarding  $\varepsilon_b$ , the %p of the non-linear effects may be considered of importance. Finally,  $v_i$  exhibits significant %p for the evolution of  $E$  (PP07); low  $v_i$  levels lead to high  $E$  values.

Table 2-4. Summary of the linear (1<sup>st</sup>-order) and non-linear ( $X^2$  and 2FI) effects of the processing conditions on the selected tensile properties (▲ increase and ▼ decrease).

Factor	▲ $E$		▲ $\sigma_y$		▲ $\varepsilon_b$	
	PP07	PP81	PP07	PP81	PP07	PP81
$v_i$	▼		▼			
$T_i$	▼▼▼	▼▼	▼▼▼	▼▼	▲▲	▲
$T_w$	▲			▼		▲▲▼
$P_h$			▲	▲▲		
2FI			(3)	(5)	(27)	
$X^2$			(12)	(7)		(32)
Resid	(26)	(58)	(8)	(9)	(44)	(21)
$R^2$	0.741	0.422	0.917	0.910	0.561	0.787

Data between parenthesis stand for the %p.

### 2.4.3 Morphology-mechanical properties relationships analysis

According to the previous results,  $T_i$  is the crucial processing parameter for both morphology and mechanical properties. Therefore, it is expected that the morphological features mostly affected by  $T_i$  will dictate the mechanical behavior of the injection molded parts.

The present study targets the variations of the mechanical properties with the morphologies. The relationships are depicted by response surfaces obtained by fitting the experimental data to a planar surface ( $z = ax + by + c$ ), using a least-square minimization procedure. The quality of the regression is evaluated by the coefficient of multiple correlation,  $R^2$ , and by the maximum and average percentage of the residuals, %Max. Res. and %Ave. Res., respectively (see Table 2-5).

Table 2-5. Maximum and average variations of the mechanical properties predictive models as a function of morphological parameters, for both materials.

Morphological inputs	Statistical parameters	PP07			PP81		
		$E$	$\sigma_y$	$\varepsilon_b$	$E$	$\sigma_y$	$\varepsilon_b$
$Sa \times \chi_s$	%Max. Res.	8	5	38	7	9	56
	%Ave. Res.	3	2	10	3	3	17
	$R^2$	0.62	0.49	0.17	0.15	0.16	0.14
$Sa \times \Omega_s$	%Max. Res.	7	5	35	6	7	47
	%Ave. Res.	3	2	11	2	3	16
	$R^2$	0.63	0.60	0.16	0.26	0.25	0.28

The  $R^2$  reveals the accuracy of the mathematical fittings.

For optimum comparison of the morphology-mechanical properties relationships for both materials, the polynomial equation type was equally defined for the combinatory relationships. Other combinations between properties and  $\chi_b$  and  $\beta_{300}$  were tested; however, they resulted in lower statistical significance, and were thus discarded. Figure 2-10 shows the relationships between the morphological features ( $Sa$ ,  $\chi_s$ ,  $\Omega_s$ ) and the mechanical properties ( $E$ ,  $\sigma_y$ , and  $\varepsilon_b$ ) measured at 1 ms<sup>-1</sup> for the two materials.

For both materials,  $E$  increases for high values of  $Sa$ ,  $\chi_s$  and  $\Omega_s$ . The modulus is improved for thicker, more crystalline (Figure 2-10a), and more highly oriented skin layers (Figure 2-10b). The contributions of  $Sa$ ,  $\chi_s$  and  $\Omega_s$  are more pronounced and statistically valid for PP07 bars than for PP81 bars. The statistical results (see Table 2-5) of these relationships show reasonable  $R^2$  values for PP07 (~0.6) and a low  $R^2$  values for PP81 (~0.2). In both cases, the percentage of residuals is small, indicating that the presented models may be used to predict the evolution of  $E$  within the considered processing window with a maximum error of 8% and an average error of about 3%.

The statistics for both materials are improved for the relationship  $E = f(Sa, \Omega_s)$  evidencing the dominance of  $\Omega_s$  compared to  $\chi_s$ . However, the existence of low  $R^2$  values, particularly for the PP81 bars, suggests that other morphological parameters could be considered.

As observed for  $E$ , the values of  $\sigma_y$  (Figure 2-10c and d) increases for high values of  $Sa$ ,  $\chi_s$ , and  $\Omega_s$ , for both materials. The yield strength is improved for thicker, more highly oriented, and more crystalline skin layers. Again, the contributions of  $Sa$ ,  $\chi_s$ , and  $\Omega_s$ , are more statistically valid (higher  $R^2$  values) for PP07 than for PP81 bars. The percentage of residuals is negligible (see Table 2-5): %Max. Res. of 5% (for PP07) and 9% (for PP81), and a %Ave. Res. of about 3%.



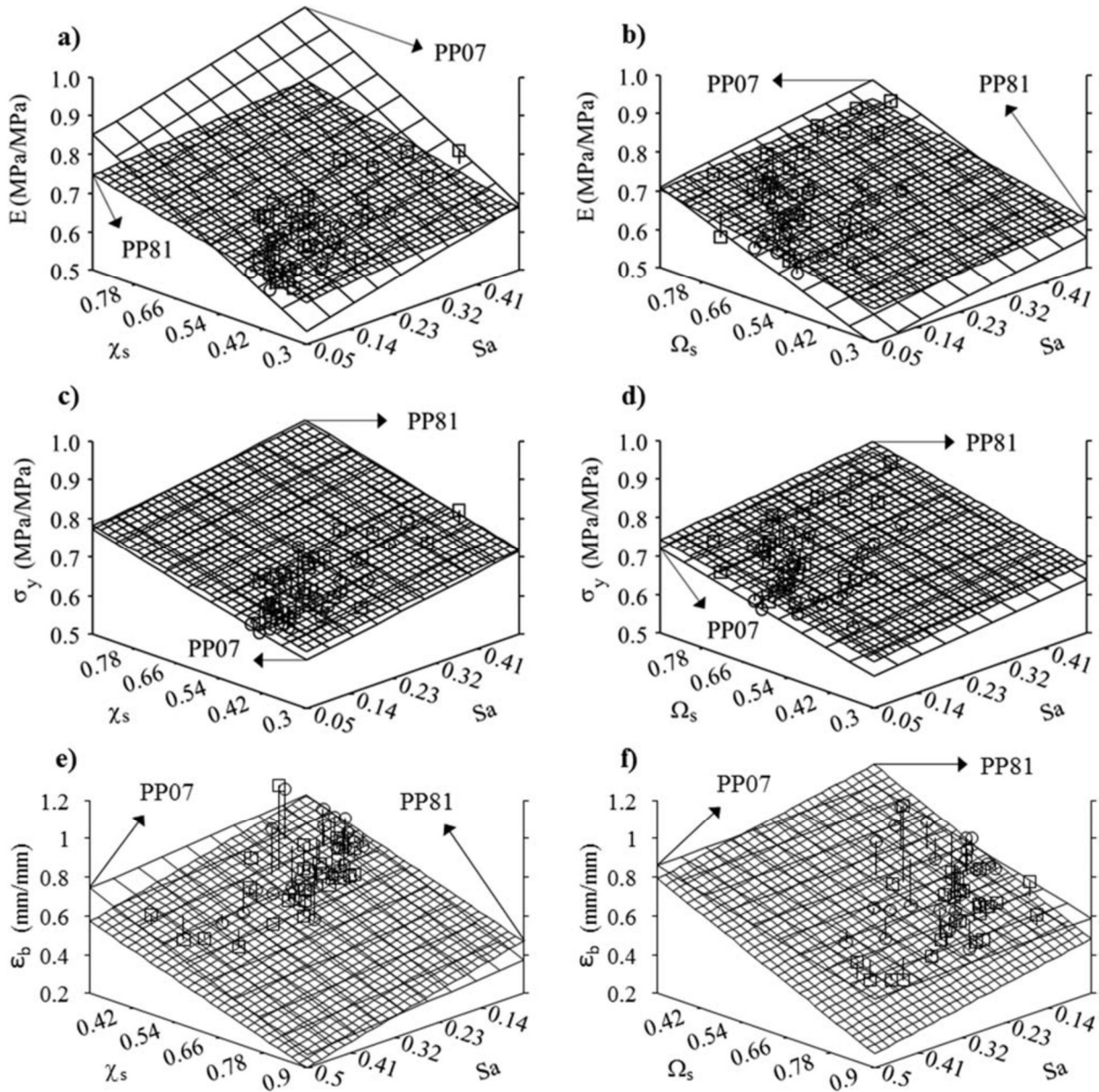


Figure 2-10. Variations of the mechanical properties (normalized values) with  $Sa$  versus  $\chi_s$  (a, c, and e); and  $Sa$  versus  $\Omega_s$  (b, d, and f). Data for PP07 are represented by the low density mesh ( $\square$ ) and data for PP81 by the high-density mesh ( $\circ$ ).

The statistics of the two materials are enhanced for the relationship  $E = f(Sa, \Omega_s)$  evidencing the dominance of  $\Omega_s$  against  $\chi_s$ . Again, the existence of low  $R^2$  values, particularly for the PP81 bars, suggests that other morphological parameters could be considered.

The value of  $\epsilon_b$  of both materials increases for low values of  $Sa$ ,  $\chi_s$ , and  $\Omega_s$  (as seen in Figure 2-10e and f). Conversely to what had been observed for  $E$  and  $\sigma_y$ , the values of  $\epsilon_b$  for both materials are improved for thinner, less oriented and more crystalline skin layers. The statistical results presented in Table 2-5 show low  $R^2$  values and a high percentage of residuals for the two tested materials. The

evolution of  $\varepsilon_b$  with the considered morphologies shows a %*Max. Res.* of 38% (for PP07) and 56% (for PP81). The %*Ave. Res.* values are also higher for the PP81 bars (17%) than for the PP07 bars (11%). The statistics of the two materials are enhanced for the relationship  $E = f(Sa, \Omega_s)$ , particularly for the PP81 material, evidencing again the dominance of  $\Omega_s$  compared to  $\chi_s$ . However, the existence of low  $R^2$  values suggests that other morphological parameters could be considered.

## 2.5 Conclusions

This work aimed at investigating the relationships between the IM process conditions, the developed morphology, and the resulting tensile properties of PP moldings measured at high strain rates (impact velocities of 1 m/s, corresponding to nominal strain rates of circa 36 s<sup>-1</sup>).

With respect to the effect of the molding conditions on the morphology development, it was concluded that  $Sa$  increases by reducing  $T_i$  and  $v_i$ . A higher  $T_w$  leads to higher  $\chi_s$  due to the slower cooling. The effect of  $T_i$  depends on the balance between effects of shear-induced crystallization and cooling rate. In this case, crystallization by shearing dominates and the crystallinity is higher when  $T_i$  is decreased and  $v_i$  increased. An increase of  $T_i$  reduces the shearing stresses and, consequently,  $\Omega_s$ . Similarly to what was observed for  $\chi_s$ , the effect of  $v_i$  on  $\Omega_s$  is more relevant for the PP81 bars. Under similar processing conditions, it seems that oriented states can relax more readily in PP81 than in PP07 due to viscosity differences. Thus, surface layers in PP81 are thinner, less oriented and less crystalline than in PP07. Conversely, the bulk crystallinity of PP81 is circa 12% higher than PP07, in spite of being independent on the processing conditions. This illustrates the different crystallization kinetics of both PP materials.

Concerning the effect of the molding conditions on the properties, it was concluded that  $E$  is maximized by lowering  $v_i$  and  $T_i$  (which is the most important variable), and by raising  $T_w$ . Typically,  $\sigma_y$  is determined by  $T_i$  and  $P_h$ , increasing for lower  $T_i$  and higher  $P_h$ . Compared to other properties,  $\varepsilon_b$  presents a significant dependence on processing conditions, increasing with  $T_i$ .

As far as the effect of the morphology on the properties is concerned, it was concluded that  $E$  increases for high values of  $Sa$ ,  $\chi_s$ , and  $\Omega_s$ , and that the same effects are observed for  $\sigma_y$ . Conversely,  $\varepsilon_b$  is higher for low values of  $Sa$ ,  $\chi_s$ , and  $\Omega_s$ .

This work clearly demonstrated the level of complexity of the relationships between IM conditions, developed morphologies, and resulting mechanical properties; it also shows that the underlying relations are far from being fully understood. Nevertheless, the work conducted provides novel information on

structure-morphology-properties relationships, particularly concerning the mechanical behavior of PP injection molded parts at high strain rates.

## References

1. K. Wang, F. Chen, Z. Li, and Q. Fu, *Prog. Polym. Sci.*, 39, 891 (2014).
2. M.M. Favaro, M.C. Branciforti, and R.E.S. Bretas, *Mater. Res.*, 12, 455 (2009).
3. R. Pantani, I. Coccorullo, V. Speranza, and G. Titomanlio, *Polymer*, 48, 2778 (2007).
4. R. Pantani, I. Coccorullo, V. Speranza, and G. Titomanlio, *Prog. Polym. Sci.*, 30, 1185 (2005).
5. R. Cermak, M. Obadal, P. Ponizil, M. Polaskova, K. Stoklasa, and A. Lengalova, *Eur. Polym. J.*, 41, 1838 (2005).
6. G.-J. Zhong and Z.-M. Li, *Polym. Eng. Sci.*, 45, 1655 (2005).
7. J. Hu, X. Gao, Z. Chen, K. Shen, and C. Deng, *J. Appl. Polym. Sci.*, 127, 1198 (2013).
8. C.N. Barbosa, R. Simoes, M. Franzen, and J.C. Viana, *J. Mater. Sci.*, 48, 2597 (2013).
9. R. Cermak, M. Obadal, P. Ponizil, M. Polaskova, K. Stoklasa, and J. Heckova, *Eur. Polym. J.*, 42, 2185 (2006).
10. T. Nagaoka, U.S. Ishiakua, T. Tomari, H. Hamada, and S. Takashima, *Polym. Test.*, 24, 1062 (2005).
11. Y. Zhou and P.K. Mallick, *Polym. Eng. Sci.*, 45, 755 (2005).
12. S. Sahin and P. Yayla, *Polym. Test.*, 24, 1012 (2005).
13. T.B. van Erp, L.E. Govaert, and G.W.M. Peters, *Macromol. Mater. Eng.*, 298, 348 (2013).
14. Y. Shinohara, K. Yamazoe, T. Sakurai, S. Kimata, T. Maruyama, and Y. Amemiya, *Macromolecules*, 45, 1398 (2012).
15. X. Yu, H. Wu, J. Li, S. Guo, and J. Qiu, *Polym. Eng. Sci.*, 49, 703 (2009).
16. J.-W. Housmans, M. Gahleitner, G.W.M. Peters, and H.E.H. Meijer, *Polymer*, 50, 2304 (2009).
17. G. Machado, E.L.G. Denardin, E.J. Kinast, M.C. Goncalves, M.A. de Luca, S.R. Teixeira, and D. Samios, *Eur. Polym. J.*, 41, 129 (2005).
18. P. Zipper, A. Janosi, W. Geymayer, E. Ingolic, and E. Fleischmann, *Polym. Eng. Sci.*, 36, 467 (1996).
19. C. Stern, A. Frick, and G. Weickert, *J. Appl. Polym. Sci.*, 103, 519 (2007).
20. M. Fujiyama, Y. Kitajima, and H. Inata, *J. Appl. Polym. Sci.*, 84, 2142 (2002).
21. X. Xiao, *Polym. Test.*, 27, 164 (2008).
22. M. Zrida, H. Laurent, V. Grolleau, G. Rio, M. Khlif, D. Guines, N. Masmoudi, and C. Bradai, *Polym. Test.*, 29, 685 (2010).

23. K.-M. Tsai and J.-K. Lan, *Int. J. Adv. Manuf. Technol.*, 79, 273 (2015).
24. C.N. Barbosa, J.C. Viana, M. Franzen, and R. Simoes, *Polym. Eng. Sci.*, 52, 1845 (2012).
25. Y.-K. Yang, *Mater. Manuf. Process.*, 21, 915 (2006).
26. K. Park and J.-H. Ahn, *J. Mater. Process. Technol.*, 146, 221 (2004).
27. J. Antony, *Design of Experiments for Engineers and Scientists*, Elsevier Science & Technology Books, Oxford, UK; (2003).
28. J.C. Viana, A.M. Cunha, and N. Billon, in *Annual Conference of the Polymer Processing Society*, Guimarães, Portugal, June 16–20, 90 (2002).
29. C.N. Barbosa, F. Carvalho, J.C. Viana, M. Franzen, T. Baranowski, and R. Simoes, *Int. J. Mater. Prod. Technol.*, 52, 76 (2016).
30. J.C. Viana, N. Billon, and A.M. Cunha, in *Annual Conference of the Polymer Processing Society*, Guimaraes, Portugal, June 16–20, 105 (2002).
31. M. Farah and R.E.S. Bretas, *J. Appl. Polym. Sci.*, 91, 3528 (2004).
32. B. Monasse and J.M. Haudin, *Colloid Polym. Sci.*, 266, 679 (1988).
33. Stat-Ease Inc, *Design-Expert 7.1 User's Guide*, Stat-Ease Inc., Minneapolis, USA; (2007).
34. O.O. Mykhaylyk, A.J. Parnell, A. Pryke, and J.P.A. Fairclough, *Macromolecules*, 45, 5260 (2012).
35. J.C. Viana, *Polymer*, 45, 993 (2004).
36. J.C. Viana, A.M. Cunha, and N. Billon, *Polymer*, 43, 4185 (2002).

### 3. MECHANICAL PROPERTIES DEPENDENCY ON TIME, TEMPERATURE AND MOLDING CONDITIONS FOR A PP

This chapter is based on the scientific paper submitted to Polymer Testing (20018).

#### Abstract

This study investigates the dynamical-mechanical response of an injection molded polypropylene (PP), with different process induced morphologies, by dynamic-mechanical thermal analysis (DMTA). PP samples were obtained through controlled injection molding design of experiments with 25 different processing condition settings (with variations of the flow rate, melt and mold temperatures, and holding pressure). DMTA tests were run in a broad temperature range ( $T = -30 \dots 50 \text{ }^\circ\text{C}$ ) at various frequencies ( $f = 0.01 \dots 10 \text{ s}^{-1}$ ) according to the stepped isothermal method. The time-temperature superposition principle was adopted and master curves in the form of storage modulus vs. frequency ( $f = 10^{08} \dots 10^{12} \text{ s}^{-1}$ ) were built to predict the elastic modulus of all PP moldings at different strain rates. The horizontal shift factors were modelled by the Arrhenius equation. The response surface methodology has been applied to identify the influence of the processing conditions on the storage modulus of the molded samples. Among the factors considered, the mold wall temperature was found to have the highest influence on the storage static modulus and frequency sensitivity coefficient.

#### 3.1 Introduction

Viscoelasticity, featured to some degree by all thermoplastics, means that polymers have solid-like characteristics such as elasticity, strength, and form stability, but also have liquid-like characteristics (such as flow) depending on time, temperature, rate, and amount of loading [1]. Dynamic-mechanical thermal analysis (DMTA) is a useful technique to understand the viscoelastic behavior of solid state polymers over a wide range of temperatures and frequencies, or response times [2-4].

In DMTA, a sinusoidal strain is applied to a sample and the resulting sinusoidal stress is measured. Under this circumstance, a viscoelastic material (e.g. polypropylene, PP) presents stress and strain responses out of phase. The phase lag, or phase angle ( $\delta$ ), is due to the time necessary for molecular motions and relaxations to occur, expressing an indication of the viscoelastic balance (damping) of the material behavior. An ideal elastic solid (obeying Hooke's law) reports a phase angle equal to  $0^\circ$ . Conversely, an ideal viscous fluid (obeying Newton's law) gives a phase angle equal to  $90^\circ$ . Therefore, a viscoelastic material shows a combination of elastic and viscous/flow behaviors.

DMTA is widely employed to determine the stiffness and damping characteristic of polymers for various applications. The dynamic mechanical properties are generally expressed in terms of storage modulus, loss modulus and damping factor, which are dependent on time (strain-rate) and temperature [2]. Modulus data in the form of the storage modulus is conceptually equivalent to that collected from traditional mechanical tests [5]. In fact, uniaxial tensile tests have been already used as a mechanical spectroscopic technique to build material master curves [6]. The frequency,  $f$ , on DMTA tests can be converted into an average strain-rate,  $\dot{\epsilon}$ , considering  $\frac{1}{4}$  of the sinusoidal loading program and assuming a linear increase of strain over time; this is mathematically translated by Equation 3-1, as follows:

$$\dot{\epsilon} = \frac{d_0}{l_0} / \frac{1}{4f} \quad \text{Equation 3-1}$$

where,  $d_0$  is the displacement amplitude imposed and  $l_0$  is the specimen reference length (considering grip distance). Moreover, DMTA gives valuable insights into the relationship between structure, morphology and properties of polymers. DMTA provides also a convenient measure of polymer transition temperatures that may influence other important properties, such as fatigue and impact resistance.

For technical use, an important aspect of developing components made of PP is the prediction of its mechanical behavior (e.g., elastic modulus) over a wide range of time and temperatures. However, there are difficulties in attaining the adequate range of temperatures and frequencies, or strain rates, in the laboratory conditions to fully describe the material properties for a specific application [3, 7, 8]. The time-temperature superposition (TTS) principle helps to obtain the information about frequencies outside the range that cannot be achieved experimentally [3]. The conventional approach to the analysis of linear viscoelastic response of polymers is based on the TTS principle [9]. Within the linear region, loading a polymer at a high strain-rate can be considered equivalent to loading at a low temperature and vice versa. The strain-rate dependence of the modulus of elasticity,  $E$ , can be fit to an empirical relationship as described by Equation 3-2.

$$E = E_0 \left( \frac{\dot{\epsilon}}{\dot{\epsilon}_0} \right)^m$$

Equation 3-2

where,  $E_0$  and  $\dot{\epsilon}_0$  are reference elastic modulus and strain-rate, respectively, and  $m$  is the strain-rate sensitivity coefficient [ $m = \partial \ln(E) / \partial \ln(\dot{\epsilon})$ ]. By assuming equivalence between time and temperature, the viscoelastic behavior of a polymer at a chosen reference temperature can be related to the viscoelastic behavior of the polymer at a different temperature by a shift factor in the timescale (horizontal shift).

Based on the TTS principle, the construction of a fully overlapped curve – master curve – involves shifting the time scale of the measured curves (e.g. storage modulus) to match the behavior at a reference temperature [10]. Evolution of the shift factor with temperature is traditionally approximated by the Arrhenius law [8, 9]. Williams-Landel-Ferry (WLF) or Vogel-Fulcher-Tamman equations provide other empirical relations for the shift factor as a function of temperature. The WLF equation is not valid for semi-crystalline polymers well below their melting points; in this case, the description of the shift factor follows typically an Arrhenius equation [10].

Most of the studies on the viscoelasticity of PP have dealt with PP-based composites and/or blends [2-4, 8, 11-16], TTS principle (master curves) [2, 3, 8, 9, 12, 17-20], morphological effects via molecular parameters [4, 14-16, 18, 20-22], and chemical treatments [2, 11, 14, 16, 18]. Some have investigated the viscoelastic properties of injection molded PP parts [11, 18, 23], and the morphological effects via processing conditions [17, 24]. To the author's best knowledge the literature on this topic is rather scarce. Some authors investigated the dynamic mechanical properties and morphology of parts from multicavity injection mold [23]. It was observed that the storage modulus was higher for moldings placed in colder zone (last filled cavity). These moldings presented wider oriented core zone (not relaxed as much as in hotter cavities), and thus better mechanical properties. PP molded at relatively low mold temperature has different mechanical properties depending on the cavity location. Another study reveals the influence of the processing conditions (melt and mold temperatures, melt filling velocity, gas pressure and gas injection delay time) on the dynamic mechanical properties of gas-assisted injection molded parts [24]. The gas injection time imparts the biggest influence on the storage modulus and mechanical loss factor. This was related to the macromolecule packing density. The considered molding conditions have main impact on viscoelastic properties of injection molded PP parts.

The present study aims at describing the effect of the injection molding conditions on the viscoelastic behavior of PP samples over a range of temperatures and frequencies. The range of temperatures was chosen to cover the entire interval of operating temperatures ( $T = -30 \dots 50 \text{ }^\circ\text{C}$ ) and strain rates ( $\dot{\epsilon} =$

$10^4 \dots 10^3 \text{ s}^{-1}$ , corresponding to frequencies in the range of 0.01 to 10 Hz). The  $\beta$ -relaxation process is characterized for all moldings. Master curves were created using the TTS principle for characterization of viscoelastic behavior of all PP samples, allowing to investigate the effect of processing conditions. This approach also allows assessing the variations of the elastic modulus with strain-rate and temperature for PP molded with different processing conditions, as required in technical best practices (e.g. numerical simulations of the mechanical behavior of thermoplastic materials).

### 3.2 Experimental and data analysis

#### 3.2.1 Materials and test specimen geometries

A commercial isotactic PP (iPP), typically used in automotive interior parts and coded as PP81, was injection molded. Table 1 summarizes the PP main characteristics. The molding geometry is an axisymmetric dumbbell like specimen with dimensions shown in Figure 1.

Table 3-1. Main features of the PP81 material.

Mel flow index (g/10 min)	10
Melt density (g/cm <sup>3</sup> )	0.734
Solid density (g/cm <sup>3</sup> )	0.911
Viscosity ( $\dot{\gamma} = 10^4 \text{ s}^{-1}$ and $T = 240 \text{ }^\circ\text{C}$ ) (Pa.s)	14.7

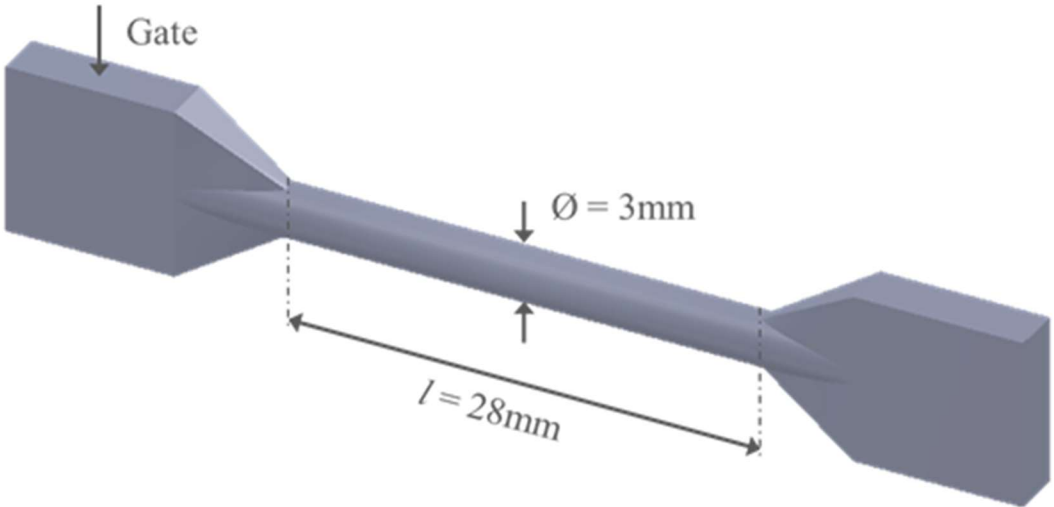


Figure 3-1. Geometry of the injection molded test specimens.



### 3.2.2 Injection molding experimental design

An injection molding (IM) machine Ferromatik Milacron K85-S/2F with a clamping force of 850 kN and maximum hydraulic injection pressure of 160 bar was used to produce all specimens. The IM boundary conditions were assessed through molding window analysis (MWA) available in the Autodesk Moldflow Insight software package. An example of MWA can be found elsewhere [25]. Based on the MWA results, a DOE plan was created to further investigate the influence of the molding parameters on the dynamic mechanical response of the tested specimens.

Table 3-2. Injection molding experimental plan based on a FCC orthogonal array ( $v_i$  – injection velocity,  $T_i$  - melt temperature,  $T_w$  – mold temperature,  $P_h$  – holding pressure).

Experiment	$v_i$		$T_i$		$T_w$		$P_h$ (*)	
	level	mm/s	level	°C	level	°C	Level	MPa
E01	-1	10	-1	200	-1	10	-1	7
E02	+1	100	-1	200	-1	10	-1	7
E03	-1	10	+1	280	-1	10	-1	7
E04	+1	100	+1	280	-1	10	-1	7
E05	-1	10	-1	200	+1	70	-1	7
E06	+1	100	-1	200	+1	70	-1	7
E07	-1	10	+1	280	+1	70	-1	7
E08	+1	100	+1	280	+1	70	-1	7
E09	-1	10	-1	200	-1	10	+1	42
E10	+1	100	-1	200	-1	10	+1	42
E11	-1	10	+1	280	-1	10	+1	42
E12	+1	100	+1	280	-1	10	+1	42
E13	-1	10	-1	200	+1	70	+1	42
E14	+1	100	-1	200	+1	70	+1	42
E15	-1	10	+1	280	+1	70	+1	42
E16	+1	100	+1	280	+1	70	+1	42
E17	-1	10	0	240	0	40	0	25
E18	+1	100	0	240	0	40	0	25
E19	0	55	-1	200	0	40	0	25
E20	0	55	+1	280	0	40	0	25
E21	0	55	0	240	-1	10	0	25
E22	0	55	0	240	+1	70	0	25
E23	0	55	0	240	0	40	-1	7
E24	0	55	0	240	0	40	+1	42
E25	0	55	0	240	0	40	0	25

(\*) pressure at the nozzle.

The current DOE plan was based on a response surface method (RSM) adopting a Face Central Composite (FCC) design. FCC is a fractional factorial design with center points, augmented with a group of axial (star) points that lets to estimate non-linearities on the response surface. It is a very efficient method to estimate linear (1<sup>st</sup> order terms) and non-linear (interaction between two terms, 2FI, and 2<sup>nd</sup> order terms, X<sup>2</sup>) variations, becoming the most commonly used RSM [26].

The following processing conditions were selected as variables (or model terms):  $v_i$  – injection velocity or flow rate;  $T_i$  – material injection temperature;  $T_w$  – mold wall temperature; and  $P_h$  – holding pressure. These factors were varied in three levels: minimum (coded as “-1”), center (coded as “0”), and maximum (coded as “+1”), as shown in Table 3-2. This makes a total of 25 different processing conditions.

### 3.3 Dynamic mechanical thermal analysis

#### 3.3.1 Equipment and test conditions

Tensile specimens' shoulders were cut off and the remaining circular cross-sections ( $\theta \approx 3$  mm and  $l \approx 28$  mm) were analyzed. Dynamic mechanical tests were performed in a Dynamic Mechanical Analyzer from Triton Technology. The analyses were run in a tensile testing mode at different frequencies ( $f = 0.01 \dots 10$  s<sup>-1</sup>) over a wide range of temperatures ( $T = -30 \dots 50$  °C). Grip distance,  $l_0$ , of 22 mm was defined. The stepped isothermal method was selected to minimize both scattering effects (due to material variability) and testing time. In this method, a single test specimen is tested under a constant strain, but at a sequence of stepwise increased temperature levels. Prior to any test, the equipment was calibrated according to the manufacturer's recommendations. The test specimens were cooled down to -30 °C and then the furnace was heated in steps of 10 °C at a rate of 1 °Cmin<sup>-1</sup> until 50 °C. In each plateau the temperature was allowed to stabilize for 1 min and the frequency of oscillation was varied from 0.01 to 10 Hz (4 points per decade in a log range) with a displacement amplitude of 15 μm (which was verified to stand within the linear viscoelastic region).

#### 3.3.2 Dynamic mechanical investigations

The storage modulus ( $E'$ ) and damping factor ( $\tan\delta$ ) were determined during the stepped isothermal test and plotted against temperature and frequency.  $E'$  is the ratio of the elastic stress to the strain and the represents the ratio of  $E''$  (loss modulus, the ratio of the viscous stress to strain) to  $E'$ , where  $\delta$  stands for the phase angle between the stress and strain curves. Generally, the peaks represent transition

or relaxation processes [3]. For PP, typically, there are three different relaxation processes due to molecular motions activated by thermal energy: the  $\gamma$ -relaxation (occur at around -50 °C, corresponding to side-chain ends methyl group rotation), the  $\beta$ -relaxation (dominant relaxation, corresponding to the glass transition temperature and associated to motions of the amorphous fraction) and  $\alpha$ -relaxation (occurring at about 100 °C, corresponding to molecular motions in the interphase of crystallites) [18]. Due to the studied temperature range, only the  $\beta$ -relaxation is scanned in the present work. Additionally, the magnitude the  $\beta$ -relaxation process ( $A_\beta$ ), the glass transition temperature ( $T_g$ ) and the homogeneity of the amorphous phase (assessed by the full width at half maximum, ) can be obtained from the analysis of  $\beta$ -relaxation process curves.

### 3.3.3 Time-temperature superposition (TTS) principle

From the DMTA data, master curves were generated to predict the elastic modulus of all PP moldings over a wide range of frequencies. Master curves construction is based on the TTS principle that assumes time-temperature equivalence, i.e. the viscoelastic behavior at a chosen temperature of reference ( $T_{ref}$ ) can be related to the viscoelastic behavior at a different temperature multiplying by a shift factor ( $a_T$ ). At  $T_{ref}$  the value of  $a_T$  is equal to 1 ( $\log a_T = 0$ ). The master curves in the form of  $E'$  vs.  $f$  were generated using only horizontal time-scale shifts. The 23 °C was selected for the superposition-shifting process.

In this study, the TTS was implemented based on the following assumptions [12]:

- i) the material is thermo-rheological simple (thus, no vertical curve shifts are required);
- ii) the material exhibits a linear viscoelastic response, i.e. the material response is stress level independent;
- iii) the structure of material remains the same in the temperature range of interest (-30 to 50 °C), so that similar molecular relaxation/retardation mechanisms are active at different temperatures, i.e. no changes in the PP degree of crystallinity and no occurrence of micro cracking or aging;
- iv) the change in density and dimensions of the material with temperature is negligible.

The shift factors of a master curve have a relationship with temperature, which can be described by the Arrhenius Equation 3-3.

$$\ln a_T = \frac{E_a}{R} \left( \frac{1}{T} - \frac{1}{T_{ref}} \right) \quad \text{Equation 3-3}$$

where  $R$  is the universal gas constant ( $8.314 \text{ Jmol}^{-1}\text{K}^{-1}$ ),  $T_{ref}$  is the reference temperature,  $T$  is the temperature, and  $E_a$  ( $\text{Jmol}^{-1}$ ) stands for the activation energy. The Arrhenius equation requires only one constant to be determined,  $E_a$ , which describes the minimum energy needed to molecular motions take place [27], i.e. the  $E_a$  of the glass transition relaxation corresponds to the energy barrier that must be overcome for the occurrence of the molecular relaxation process [12].

Many studies investigated the possibility of applying the TTS to semi-crystalline polymers (e.g. PP and high density polyethylene), supporting that the temperature dependence of the shift factors could be described by the Arrhenius law [7, 20, 28]. For semi-crystalline polymers well below their melting temperatures, the description of the shift factors follows an Arrhenius rather than a WLF model (more suitable for amorphous polymers above the glass transition temperature) [10]. Nevertheless, the WLF approach was also applied to generate master curves describing the behaviour of high density polyethylene resin over a wider range of frequencies from  $35 \text{ }^\circ\text{C}$  to  $120 \text{ }^\circ\text{C}$  [29].

### 3.4 Results and discussion

Detailed plots of the storage modulus and damping factor are represented as a function of the temperature for a representative selection of the IM conditions. In this case, the DMTA results are presented for a representative frequency ( $f = 0.1 \text{ s}^{-1}$ ). The experiments E06 and E11 (see Table 3-2), having opposite molding parameters levels and extreme values of  $E'$ , were selected to demonstrate the effect of the frequency on the storage modulus and damping factor. Here, for overall graphical clearness, only  $f(\text{s}^{-1}) = 0.03, 1$  and  $10$  are shown.

#### 3.4.1 Storage modulus, $E'$

In Figure 3-2,  $E'$  is plotted against the temperature at frequencies of  $0.03, 1$  and  $10 \text{ s}^{-1}$  for two representative IM experiments, E06 and E11.  $E'$  increases with increasing frequency, as represented by the vertical dashed arrow, and the decreasing of the temperature. This tendency is replicated for all 25 experiments.  $E'$  is highly temperature-dependent. At temperatures below  $0 \text{ }^\circ\text{C}$  (the glass transition region of PP is  $-10$  to  $0 \text{ }^\circ\text{C}$ ),  $E'$  values are fairly high, and as the temperature decrease the increase of  $E'$  becomes less significant. Above the  $T_g$  region,  $E'$  values drop significantly and, for very high temperatures, they start to decrease slowly. For the lowest frequency, the maximum percentage of

variation of  $E'$  found among the 25 experiments is  $\Delta E'(T_{f_{min}}) \approx 350\%$ , and  $\Delta E'(T_{f_{max}}) \approx 258\%$  for the highest frequency. Thus, the variation of  $E'$  with temperature is smaller at higher frequencies. Observing particularly the results of experiment E06, at low temperatures ( $T = -30\text{ }^\circ\text{C}$ ) there is a variation of  $E'$  with the frequency of about 10% ( $E'[f(10\text{ s}^{-1})] \approx 2800\text{ MPa}$  and  $E'[f(0.03\text{ s}^{-1})] \approx 2540\text{ MPa}$ ) and, at high temperatures ( $T = 50\text{ }^\circ\text{C}$ ) there is a variation of about 33% ( $E'[f(10\text{ s}^{-1})] \approx 860\text{ MPa}$  and  $E'[f(0.03\text{ s}^{-1})] \approx 645\text{ MPa}$ ). Considering the E11, at  $T = -30\text{ }^\circ\text{C}$  there is a variation of ca. 11% ( $E'[f(10\text{ s}^{-1})] \approx 2440\text{ MPa}$  and  $E'[f(0.03\text{ s}^{-1})] \approx 2200\text{ MPa}$ ) and, at  $T = 50\text{ }^\circ\text{C}$  there is a variation of about 39% ( $E'[f(10\text{ s}^{-1})] \approx 682\text{ MPa}$  and  $E'[f(0.03\text{ s}^{-1})] \approx 491\text{ MPa}$ ). The maximum percentage of variation of  $E'$  found among the 25 experiments corresponds to  $\Delta E'(f_{T_{min}}) \approx 14\%$ , for the lowest temperature, and  $\Delta E'(f_{T_{max}}) \approx 41\%$ , for the highest temperature. The results reveal a stronger strain-rate-sensitivity of PP at higher temperatures.

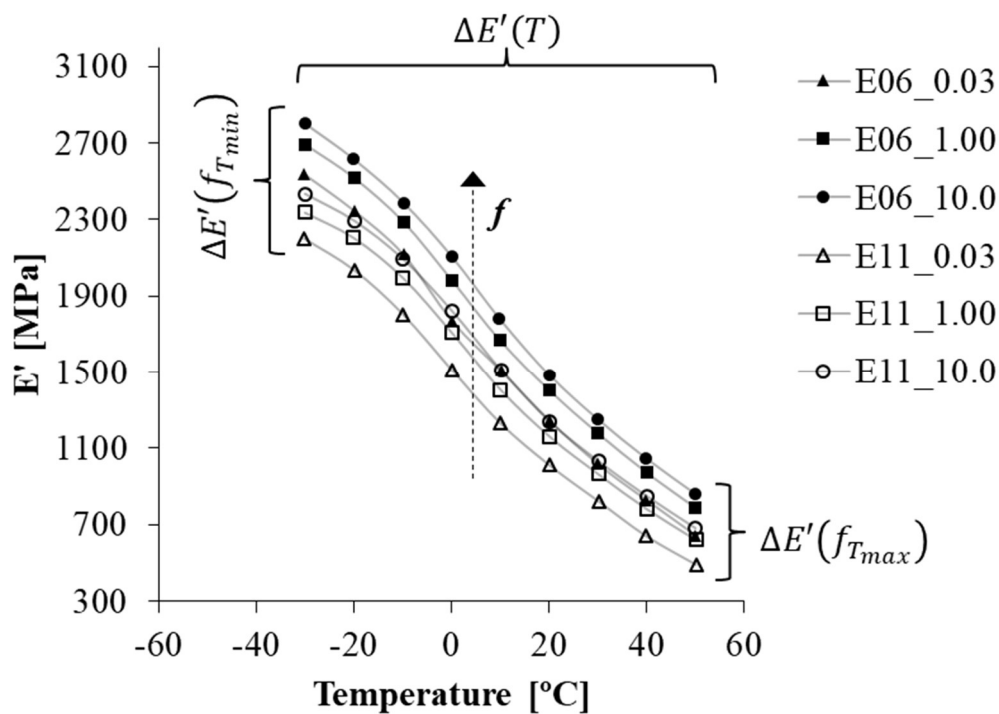


Figure 3-2.  $E'$  as a function of temperature and frequency (0.03, 1 and 10 s<sup>-1</sup>) for selected IM experiments.

Figure 3-3 shows the  $E'$  as a function of temperature for the particular IM at a chosen frequency ( $f = 0.1\text{ s}^{-1}$ ). Only few experiments from Table 3-2 are plotted for a better graphical comprehension, but extreme variations are shown. A distinct behavior among IM experiments is observed reflecting a clear

effect of the processing conditions on  $E'$  values. The experiments E05, E06 and E13 [all with  $T_i$  (-1) and  $T_w$  (+1)] show the maximum  $E'$  values. On the other hand, the experiments E04, E11 and E12 [all with  $T_i$  (+1) and  $T_w$  (-1)] present the lowest results for  $E'$ . This is observed either for the highest (50 °C) and lowest (-30 °C) test temperatures. For the same temperature and frequency, the  $E'$  results show a total variation of  $\Delta E' \left( IM_{f_{min}}^{T_{max}} \right) \approx 31\%$ . The results reveal that  $E'$  is significantly dependent on the processing conditions and this sensitivity is maximized for lower temperatures.

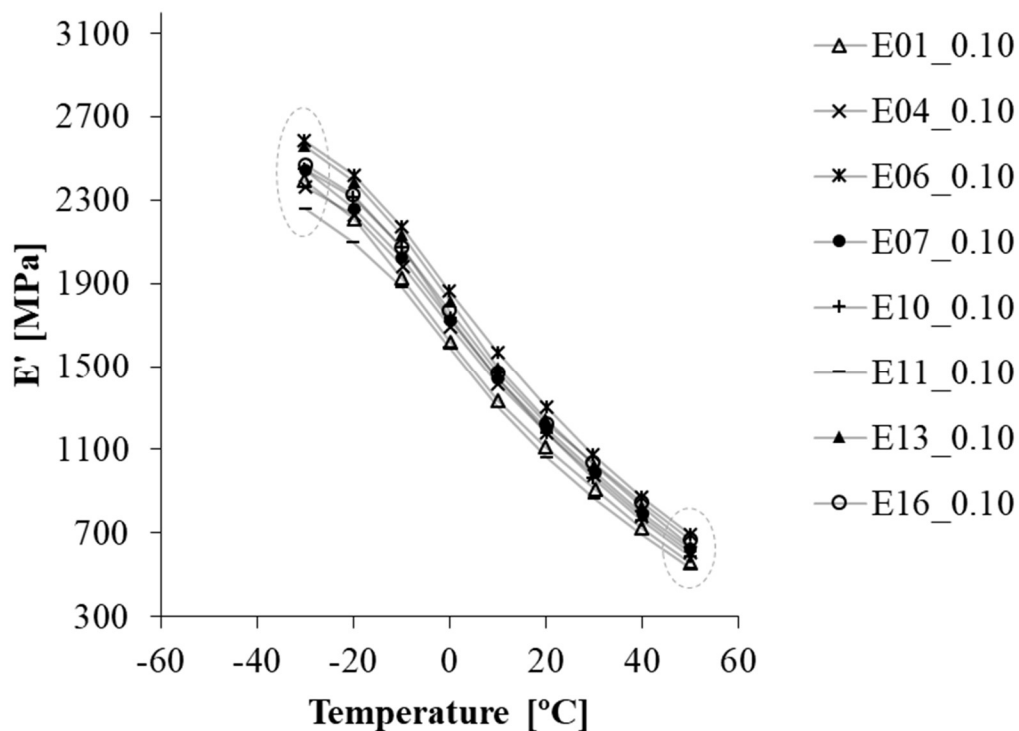


Figure 3-3.  $E'$  as function of temperature for the selected IM experiments at  $f = 0.1 \text{ s}^{-1}$ .

### 3.4.2 Loss or damping factor, $\tan\delta$

The  $\tan\delta$  indicates how good a material is at absorbing mechanical energy. It depends on the state of the material, its temperature, and applied frequency. Figure 3-4 shows the  $\tan\delta$  as a function of temperature at frequencies of 0.03, 1 and 10  $\text{s}^{-1}$  for the representative experiments, E06 and E11. It is obvious that the test temperature has a large effect on the changes of  $\tan\delta$ . Higher temperatures lead to higher loss factor values, as expected. For the lowest frequency, the maximum percentage of variation of  $\tan\delta$  with the temperature among the 25 experiments is  $\Delta \tan\delta(T_{f_{min}}) \approx 408\%$ , and for the highest

frequency is  $\Delta \tan \delta(T_{f_{max}}) \approx 142\%$ . Also, the plot shows that the higher the frequency the lower the loss factor, i.e. there is a vertical shift down of the  $\tan \delta$  by increasing the frequency, as represented by the vertical dashed arrow. This tendency is replicated for all the 25 experiments. The maximum percentages of variation of  $\tan \delta$  as a function of frequency, among the 25 experiments,  $\Delta \tan \delta(f_{T_{min}}) \approx 78\%$  are for the lowest temperature and  $\Delta \tan \delta(f_{T_{max}}) \approx 138\%$  for the highest temperature. Also, the results reveal a significant frequency-sensitivity of the  $\tan \delta$  of the molded samples due to processing.

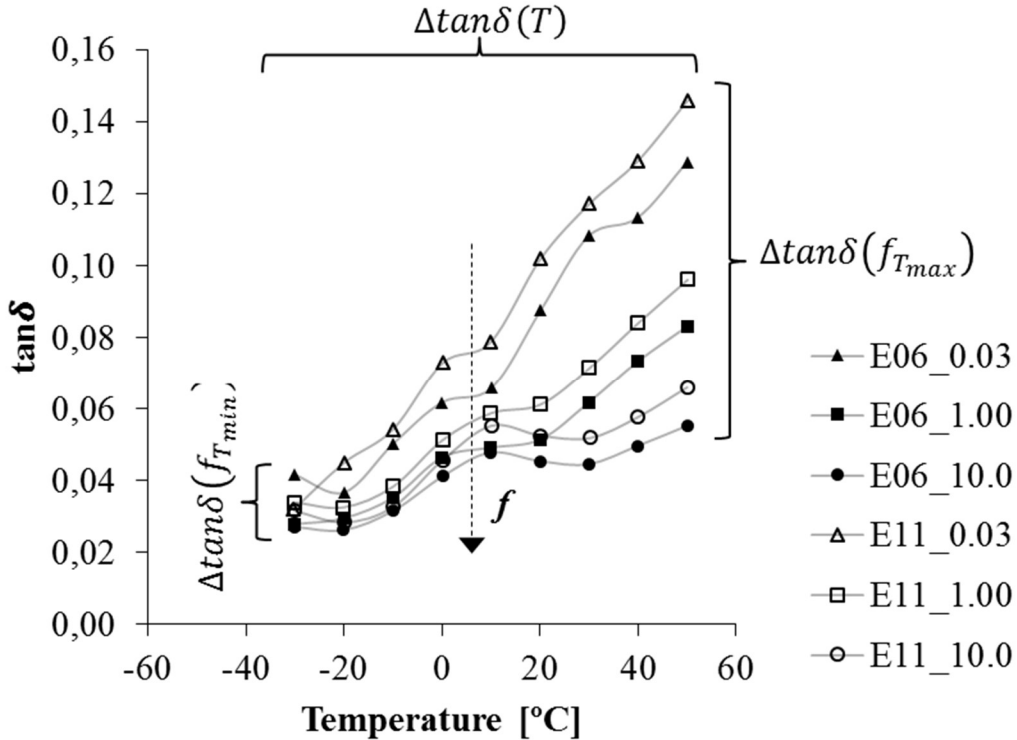


Figure 3-4.  $\tan \delta$  as a function of temperature and frequency (0.03, 1 and 10 s-1) for the selected IM experiments.

Figure 3-5 shows the  $\tan \delta$  as a function of temperature and IM conditions at  $f = 0.1$  s-1. As in the case of  $E'$ , only selected experiments from Table 3-2 are plotted for better comprehension. The  $\tan \delta$  is significantly affected by the processing conditions. For the same temperature and frequency, the results show a total  $\Delta \tan \delta (IM_{f_{max}}^{T_{min}}) \approx 45\%$ . These results reveal that  $\tan \delta$  is significantly dependent on the processing conditions and its sensitivity is more significant at higher temperatures.

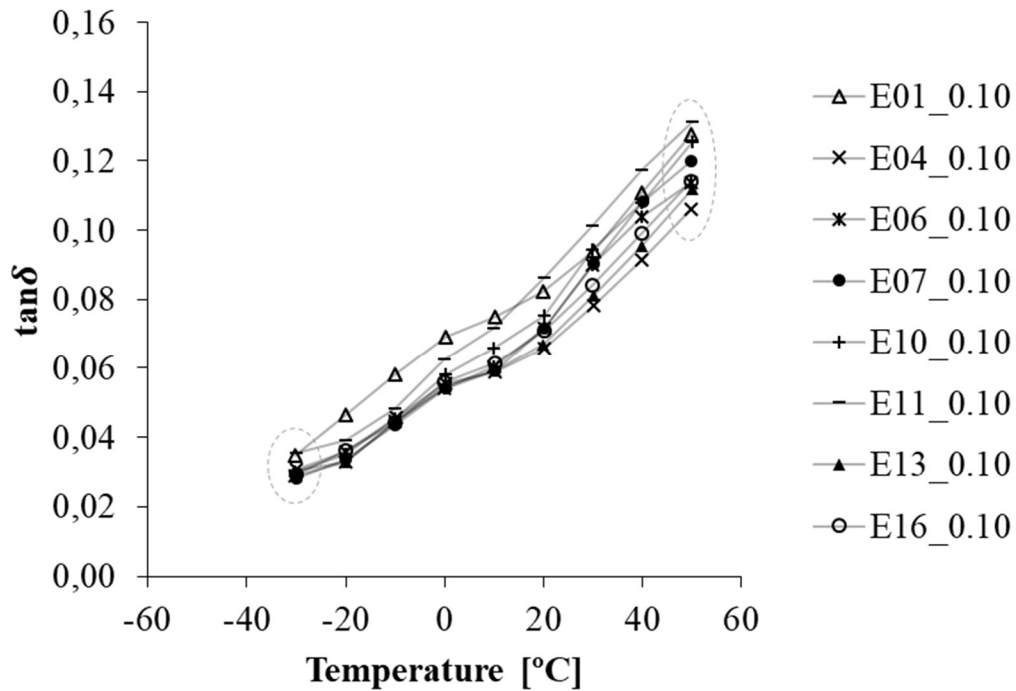


Figure 3-5.  $\tan\delta$  as a function of the temperature for the selected IM experiments at  $f = 0.1 \text{ s}^{-1}$ .

### 3.4.3 Magnitude of the $\beta$ -relaxation process, $A_\beta$

Some peaks can be observed in the previous damping curves around -10 to 10 °C, i.e. the  $T_g$  region of the PP. These peaks were investigated to quantify the  $\beta$ -relaxation process. Due to the low number of points in the scattered curves, a polynomial function was used for fitting. Then, curves were shifted, i.e. converted to the same linear basis by doing a baseline subtraction. The magnitude of the  $\beta$ -relaxation process ( $A_\beta$ ) is quantified by calculating the area below the peak [18].

Still, from these peaks the full-width-at-half-maximum,  $FWHM$ , can be calculated. This is related to the homogeneity of the amorphous phase, so that a larger value implies a higher inhomogeneity of the amorphous phase (broader peak) [11].  $T_g$  concerns to the mobility within the amorphous regions and may be difficult to determine since the peaks are rather broad [8]. However,  $T_g$  can be defined as the maximum of the transition in the loss modulus curve or in the loss factor curve [11]. The results presented in this work correspond to this latter definition, i.e.  $T_g$  corresponds to the position of the center of the loss factor peaks.

Figure 3-6 shows the  $\beta$ -relaxation curves (fitting results with baseline correction) for the selected experiments at representative frequencies ( $f = 0.1 \text{ s}^{-1}$  and  $10 \text{ s}^{-1}$ ). A marked difference in the  $A_\beta$  exists



when comparing experiments at a given frequency, for instance at  $10 \text{ s}^{-1}$ . The  $\beta$ -relaxation peaks are shifted to higher temperature region as the frequency increases. Moreover, the magnitudes of  $\beta$ -relaxation peaks are higher for higher frequencies.

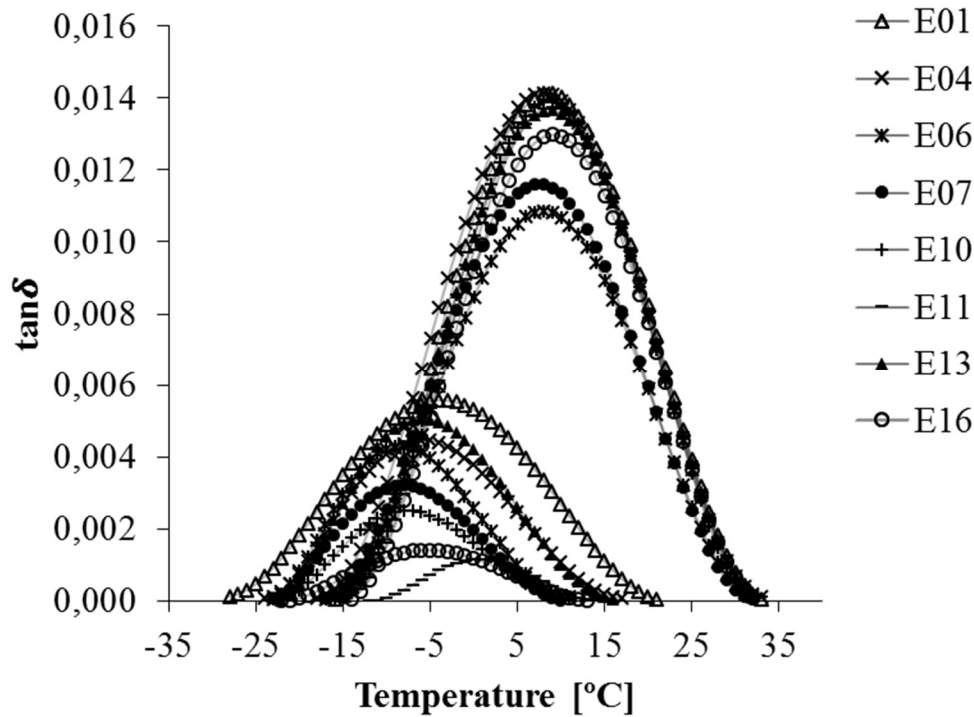


Figure 3-6.  $\beta$ -relaxation curves obtained for 8 selected experiments at  $0.1 \text{ s}^{-1}$  (dataset of lower amplitude curves) and  $10 \text{ s}^{-1}$  (dataset of higher amplitude curves).

Table 3-3 summarizes the results of  $T_g$ ,  $FWHM$  and  $A_\beta$  for all PP moldings at  $f = 0.1 \text{ s}^{-1}$  and  $10 \text{ s}^{-1}$ . At  $f = 0.1 \text{ s}^{-1}$ ,  $A_\beta$  has a total variation of 822%,  $FWHM$  varies 91% and  $T_g$  shows a change of about 1000%. The total variations of these parameters are significantly reduced when assessed at high strain rates ( $f = 10 \text{ s}^{-1}$ ), respectively, 108%, 10% and 43%. The results reveal a strong influence of the IM conditions on the  $\beta$ -relaxation peaks characteristics; such effect is magnified for lower frequencies.

An increase on the frequency leads to increased intensity of the  $\tan \delta$  and shifts the position of the  $\beta$ -relaxation region to higher temperatures (higher magnitude of the  $\beta$ -relaxation process and higher mobility of the amorphous phase).  $FWHM$  and  $A_\beta$  are also larger when assessed at high strain rates. The inhomogeneity of the amorphous phase is well disclosed at high frequencies.

Table 3-3.  $\tan\delta$  parameters for all IM conditions at distinct frequencies ( $T_g$  – glass transition temperature,  $FWHM$  – full width at half maximum of the  $\beta$ -relaxation peak, and  $A_\beta$  – area of the  $\beta$ -relaxation peak).

Run	$T_g$ (°C)		$FWHM$ (°C)		$A_\beta$	
	0.1 s <sup>-1</sup>	10 s <sup>-1</sup>	0.1 s <sup>-1</sup>	10 s <sup>-1</sup>	0.1 s <sup>-1</sup>	10 s <sup>-1</sup>
<u>1</u>	-4	9	26,69	25,68	0,147	0,361
2	-4	9	23,68	26,24	0,147	0,398
3	-2	9	20,11	24,60	0,032	0,368
<u>4</u>	-6	8	21,55	26,13	0,094	0,366
5	-6	7	21,02	25,47	0,094	0,304
<u>6</u>	-8	8	18,14	25,39	0,077	0,273
<u>7</u>	-8	7	18,09	25,44	0,057	0,292
8	-6	8	21,78	25,52	0,118	0,358
9	-7	9	20,07	24,53	0,049	0,311
<u>10</u>	-8	9	17,75	24,75	0,043	0,339
<u>11</u>	1	9	13,94	24,75	0,016	0,337
12	-4	8	24,90	25,76	0,107	0,389
<u>13</u>	-6	9	20,74	25,54	0,106	0,348
14	-6	9	23,26	26,07	0,114	0,385
15	-7	7	20,13	26,07	0,074	0,347
<u>16</u>	-5	9	19,46	24,90	0,028	0,323
17	-8	9	17,91	24,58	0,080	0,247
18	-7	7	19,98	26,44	0,049	0,349
19	-4	8	23,46	25,95	0,088	0,409
20	-9	10	19,48	25,89	0,059	0,356
21	-3	9	24,24	26,86	0,087	0,513
22	-8	8	19,73	26,04	0,070	0,340
23	-1	8	22,00	26,12	0,075	0,394
24	-6	8	21,99	26,11	0,077	0,371
25	-6	8	20,73	26,48	0,090	0,365
Var.%	111,1	42,9	91,5	120	818,8	107,7

#### 3.4.4 Time-temperature superposition (TTS) and master curves

The variations of  $E'$  for a temperature range between -20° C and 50 °C, at frequencies ranging from 0.03 s<sup>-1</sup> to 10 s<sup>-1</sup>, are shown in Figure 3-7, for experiments E06 and E11. There is an increase in  $E'$  with increasing frequency and decreasing temperature. The effect of processing on  $E'$  is again clearly revealed – E06 shows higher than E11.

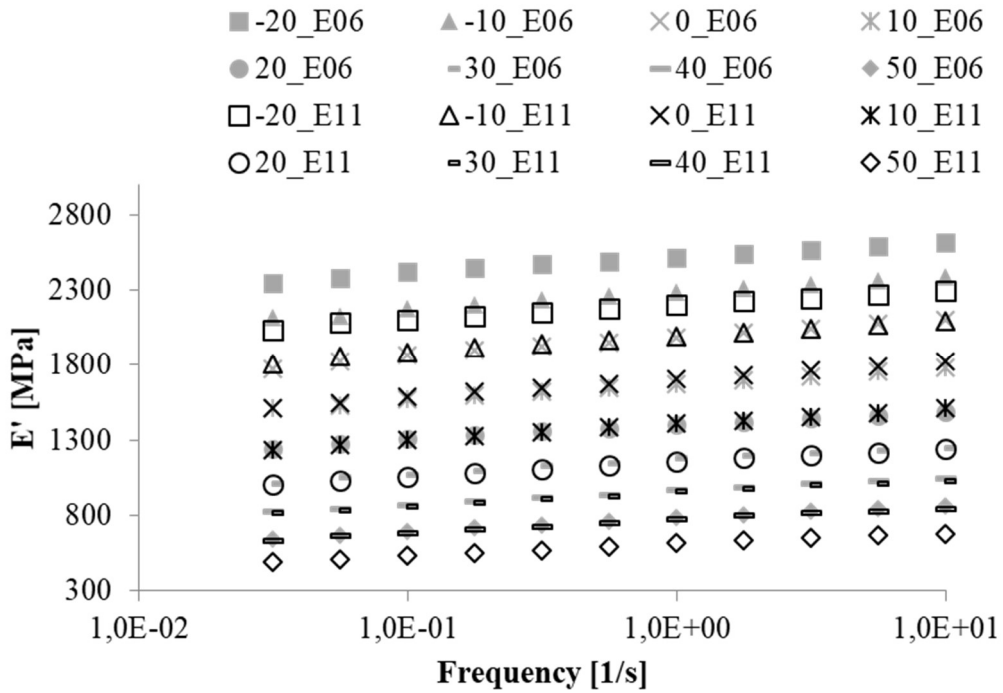


Figure 3-7.  $E'$  vs.  $f$  for a range of temperatures and for E06 and E11 samples.

Based on DMTA results, the TTS principle was adopted and master curves constructed in the form of storage modulus vs. frequency ( $E'$  vs.  $f$ ) for all PP moldings. The variation of the storage modulus with frequency/strain-rate is then obtained over a wide range of frequencies/strain-rates, outside the range normally experimentally achievable with standard tensile machines.

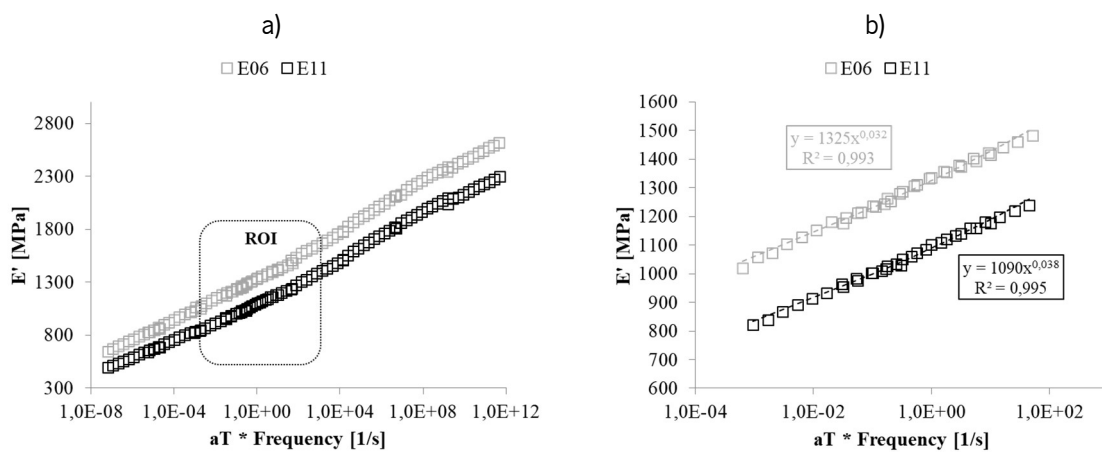


Figure 3-8.  $E'$  master curves for the E06 and E11 at a reference temperature of 23 °C: a)  $E'$  vs.  $f$  over a wide range of frequencies; and b)  $E'$  vs.  $f$  covering only the range of  $10^3$  to  $10^2$  s<sup>-1</sup>.

The  $E'$  vs.  $f$  master curves created at a reference temperature of 23 °C are shown in Figure 3-8. The later shows a detail of the region of interest (ROI), corresponding to frequencies ranging from  $10^3$  to  $10^2$  s<sup>-1</sup>. These are representative frequency limits observed in quasi-static and dynamic loadings of automotive crash tests (e.g. 3 ms<sup>-1</sup>). Molding E06 presents the highest  $E'$  values and differences are magnified for higher frequencies.

Table 3-4. Parameters from the  $E'$  vs  $f$  curves for all molding conditions [ $E'_0$  – storage static modulus ( $f = 0$  Hz at 23 °C),  $m$  – frequency (strain-rate) sensitivity coefficient, and  $E_a$  – activation energy].

Run	$E'_0$ (MPa)	$m$	$E_a$ (kJmol <sup>-1</sup> )
1	1140	0,0398	370
2	1280	0,0319	367
3	1145	0,0381	365
4	1198	0,0327	369
5	1291	0,0312	369
6	1325	0,0325	368
7	1218	0,0326	370
8	1265	0,0317	368
9	1186	0,0354	368
10	1204	0,0355	369
11	1090	0,0383	369
12	1166	0,0374	367
13	1274	0,0332	368
14	1274	0,0330	366
15	1265	0,0318	368
16	1251	0,0323	367
17	1238	0,0349	369
18	1234	0,0319	371
19	1234	0,0324	370
20	1178	0,0361	368
21	1124	0,0378	365
22	1282	0,0310	368
23	1259	0,0314	367
24	1283	0,0337	368
25	1260	0,0330	369
Var.%	21,6	28,4	1,6

In the considered ROI, a linear dependence of  $E'$  on the frequency is obtained. The slope,  $m$ , of this straight line gives the frequency (or strain-rate) sensitivity of  $E'$ . Also, the ordinate at the origin,  $E'_0$ , provides the value for a theoretical  $f = 0$  s<sup>-1</sup> (static modulus), at 23 °C (reference temperature). Table 3-4 summarizes the values of  $m$  and  $E'_0$  for all molded specimens. Processing induces variations of ca.

22 and 28%, on  $m$  and  $E_0$  values, respectively. Finally, the applicability of horizontal shifts reveals that the used PP is a thermo-rheological simple material (in the range of temperatures studied), i.e. all its relaxation times have the same dependence on the temperature.

The shift factors,  $\log(a_T)$ , used for the generation of the master curves for all the PP moldings are plotted in Figure 3-9 against the reciprocal of the absolute temperature difference. The Arrhenius equation was applied to these data and the dashed lines show the best-fit straight line to the plotted data. These equations (of the type  $y = slope \times x$ ) represent the linearization of Equation 3-3. The  $R^2$  (coefficient of correlation) fit parameter value is adequate, indicating that applied shifts are valid. The  $E_a$  calculated from the slope of the regression curves of E06 and E11 are both approx.  $368 \text{ kJmol}^{-1}$ , which is within the range reported previously in the literature [3, 8]. Table 3-4 summarizes the  $E_a$  values for all molded specimens. Interestingly,  $E_a$  is not affected by processing conditions (that induces a maximum variation of only 1.6%). This activation energy is the energy required for cooperative molecular movements of the amorphous phase at  $T_{ref}$ . This value being constant means a similarity of these local movements of the amorphous phase, regardless the morphology developed during processing (in the range varied in this study).

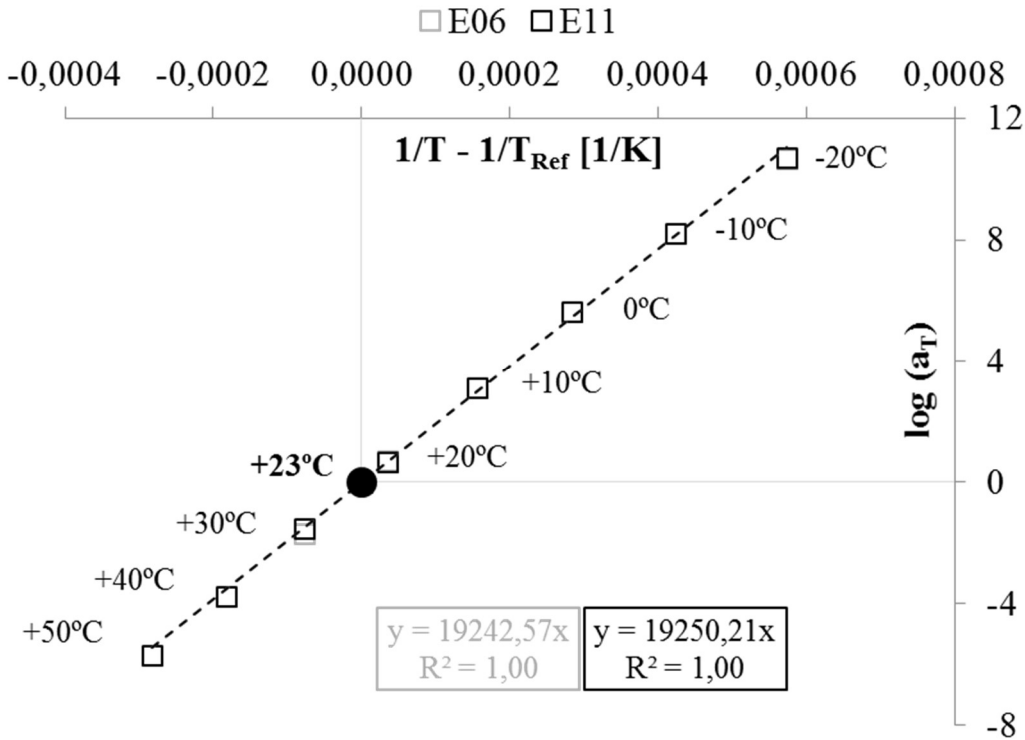


Figure 3-9. Variation of  $\log a_T$  with  $1/T - 1/T_{ref}$  for the molded specimens of E06 and E11 [dashed lines represent the linear fits for each experiment (grey  $\square$  – E06, black  $\square$  – E11) and  $\bullet$  stands for the  $T_{ref}$ , where  $a_T = 1$  (no shift), thus  $\log a_T = 0$ ].

### 3.4.5 Dependency on processing

The dependency on processing of the  $\beta$ -relaxation parameters ( $T_g$ ,  $FWHM$  and  $A_\beta$ ) and  $E'$  vs  $f$  master curve parameters ( $E'_0$ ,  $m$ ,  $E_a$ ) are analyzed, separately, through an analysis of variance, ANOVA. The significant processing conditions ( $v_i$ ,  $T_i$ ,  $T_w$  and  $P_h$ ), their quadratic effects and interactions were selected with a confidence level of 95%. In most cases, the residuals were considerably higher, meaning that the estimated experimental errors are higher. This occurs mainly for the case of the  $\beta$ -relaxation parameters, whose calculations are more difficult (e.g. low and broad  $\beta$ -relaxation peaks).

$T_g$  is only affected by  $T_w$  at both frequencies (Figure 3-10), with a percentage of contribution of 21% and 17%, at low and high frequencies, respectively. In this case the percentage of residual is higher, around 80%. The trend is a decrease of  $T_g$  as  $T_w$  increases. This decrease of  $T_g$  is higher at low frequencies.  $T_w$  was found to influence the degree of crystallinity of the skin layer, increasing with it [30]. It has been shown that  $T_g$  shifts to higher temperatures with increasing level of orientation of the amorphous phase [8] and decreasing degree of crystallinity [31].  $T_g$  decreases therefore with the increase of the degree of crystallinity of the skin layer.

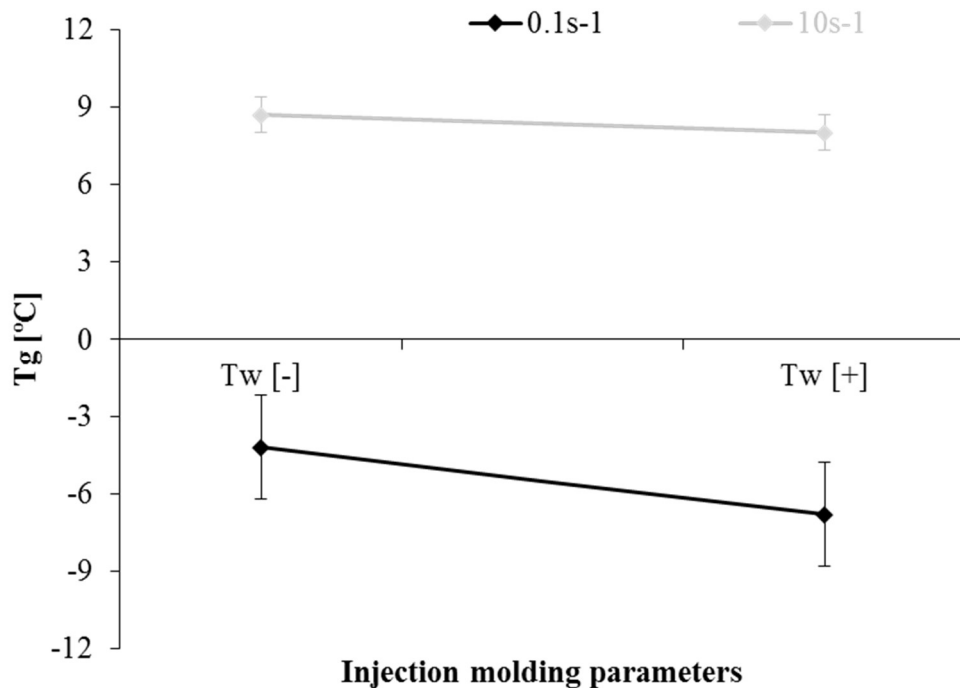


Figure 3-10. Variation of  $T_g$  with  $T_w$  at frequencies of 0.1 and 10  $s^{-1}$ .

The variation of *FWHM* reveal high interactions between the injection molding variables (Figure 3-11). At low frequency, main influent interactions were  $v_i \times T_i$  and  $T_w \times P_h$ , with percentages of contribution of 16 and 14%, respectively, but the residuals are again high (70%). These interactions are strong. At low  $T_i$  and  $P_h$ , *FWHM* decreases with  $v_i$  and  $T_w$ . However, at high  $T_i$  and  $P_h$  the opposite happens, i.e. *FWHM* increases with  $v_i$  and  $T_w$ . At high frequencies, the *FWHM* values are higher, but the effect of processing is rather smaller. The injection flow rate becomes a significant factor with 40% of contribution for the variations of *FWHM*, mainly its quadratic effect ( $\%p \approx 29\%$ ). Also, interactions found to be significant are  $v_i \times T_w$  ( $\%p \approx 10\%$ ) and  $T_w \times P_h$  ( $\%p \approx 8\%$ ).

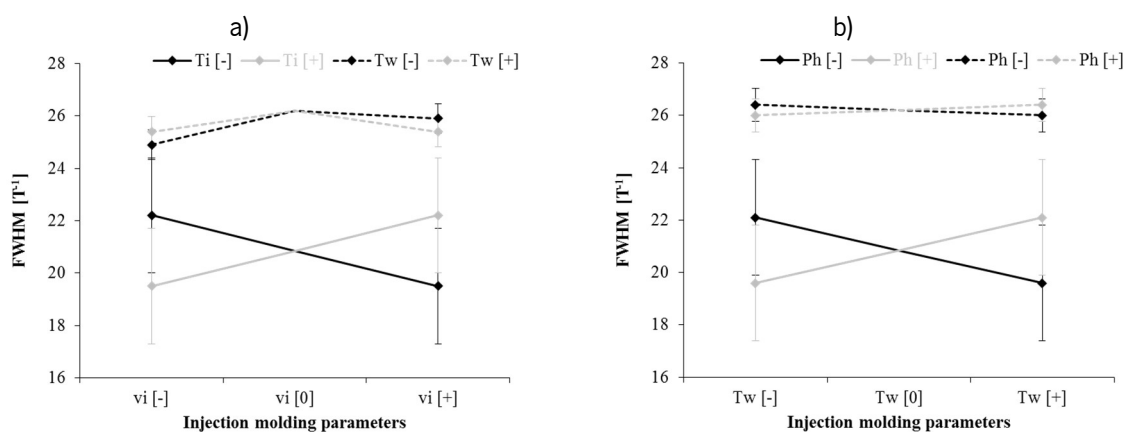


Figure 3-11. Variations of *FWHM* with the significant processing conditions for frequencies: a) 0.1 s<sup>-1</sup> and b) 10 s<sup>-1</sup>.

Generally, higher *FWHM* values are obtained for the low setting of all the processing conditions or for their opposed high setting. *FWHM* is an indication of the “breath” of the  $T_g$ , i.e. the broader the *FWHM* the higher the inhomogeneity of the amorphous phase. For iPP annealed at different temperatures, the broadness of  $\tan \delta$  peak increased with decreasing of the degree of crystallinity ( $T_g$  increased) [32]. As the degree of crystallinity increases, the composition of the amorphous materials changes by segregation of atactic PP from the crystallites. Also, *FWHM* was found to increase with the crystallization temperature for PLLA (simultaneously,  $T_g$  decreased), indicating an increase of the broadness of the distribution of relaxation times [31]. It has been argued that as the thickness of the rigid amorphous phase (RAF) increases,  $T_g$  decreases and the broadness of the time spectrum is higher. The RAF induces easier conformational motions in the mobile amorphous phase, reducing  $T_g$  but broadening the relaxation time spectrum. Injection molded samples produced under different processing conditions

show an intricate hierarchical microstructure development along the total three-dimensional domain of the moldings. A complex distribution of relaxation times characteristics, representative of determined molecular motions, is then expected. This type of relationships is not yet fully understood.

Figure 3-12 shows the variations of  $\beta$ -relaxation peak area,  $A_\beta$ , i.e. the magnitude of the  $\beta$ -relaxation process, with the processing conditions. At low frequencies,  $A_\beta$  decreases slightly with increasing  $T_i$  and  $P_h$  (% $p$  of 16 and 14%, respectively; residuals are ca. 73%). At high frequencies, the  $A_\beta$  values are higher, and showing a different dependence of the processing parameters:  $v_i$  and  $T_w$  are the significant processing conditions, with % $p$  of 34% (from a  $v_i^2$  dependence) and 26% (from which 11% are from  $T_w^2$ ), respectively.  $A_\beta$  shows a maximum for intermediate  $v_i$  and low  $T_w$  settings. For this material, it has been shown that high  $T_i$ , low  $T_w$  and  $v_i$  led to a lower degree of crystallinity and less oriented skin layer [30]. This may increase the magnitude of the glass transition (low degree of crystallinity) or decrease it (low level of orientation). It has been shown that the magnitude of glass transition peak is lower for highly oriented PP (e.g. fibers) rather than for isotropic PP, due to the fact that taut-tie amorphous molecular chains are less free to move [8]. The height of the  $\beta$ -relaxation peak was also found to decrease with increasing the degree of crystallinity [31].  $A_\beta$  seems then to be determined by the degree of crystallinity of the skin layer.

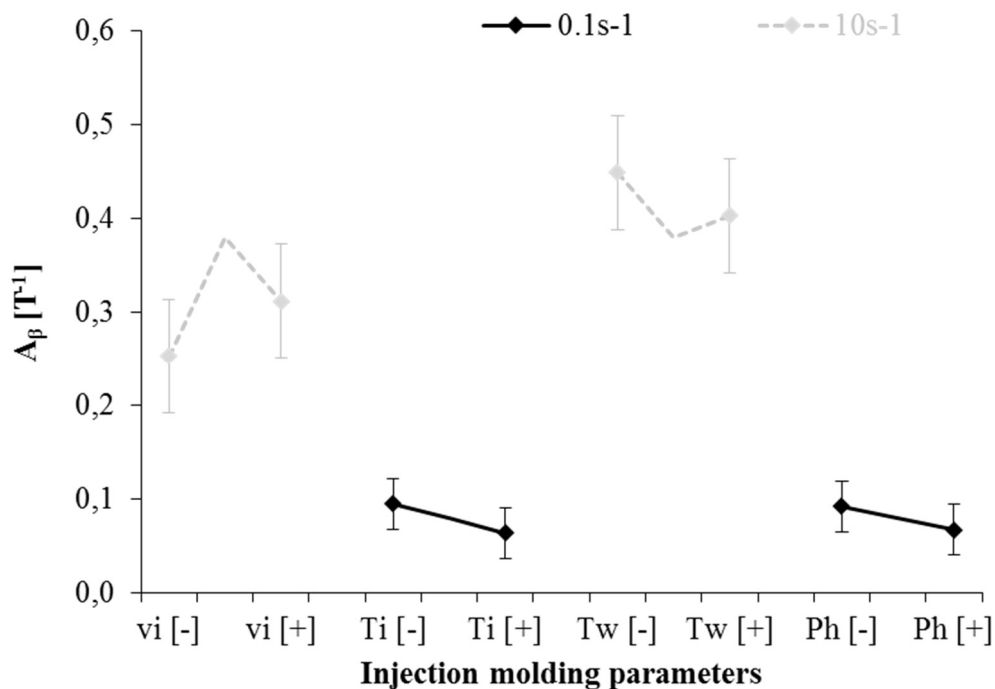


Figure 3-12. Variations of  $\beta$ -relaxation peak area,  $A_\beta$ , with the significant processing conditions for frequencies: a) 0.1 s<sup>-1</sup> and b) 10 s<sup>-1</sup>.



The above complex dependencies reveal the diversity of states of the amorphous phase due to variations of the processing conditions. The established relationships evidence the complex behavior of the  $\beta$ -relaxation process and its dependence on processing conditions. At the origin of the  $\beta$ -relaxation process are cooperative molecular motions in the mobile amorphous regions, within the lamellar stacks (e.g. inside spherulites, between kebabs in highly oriented shish-kebab structures) and in the amorphous zones between supra lamellar structures (e.g. interfaces between spherulites, shish-kebabs). Rigid amorphous phase and tie-tau molecules will play also a role on amorphous phase mobility. The establishment of relationships between the  $\beta$ -relaxation process and the morphology of injection molded semi-crystalline polymers is a huge scientific challenge, while with a great practical importance as this process shall determine the mechanical behavior of molded products.

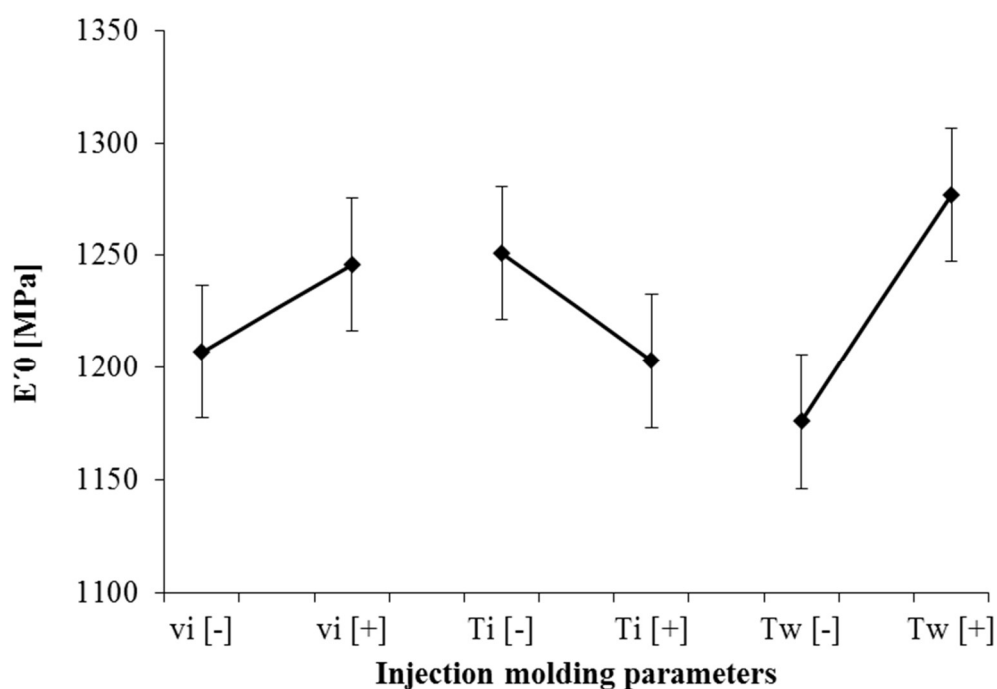


Figure 3-13. Variations of the static modulus  $E'_0$  (at  $f = 0$  and at 23 °C) with the significant processing conditions.

In Figure 3-13 the variations of  $E'_0$  are shown with the molding variables. Main contributions arise from  $v_i$  ( $\%p \approx 8\%$ ),  $T_i$  ( $\%p \approx 12\%$ ) and  $T_w$  ( $\%p \approx 54\%$ ), with a residual of 26%. As already abovementioned, higher  $T_w$  values result in higher degree of crystallinity of the skin layer [30]. Also, low  $T_i$  and high  $v_i$  lead to high degree of crystallinity of the skin layer and of its level of molecular orientation.

The  $E'_0$  appears to be closely related to the degree of crystallinity and level of molecular orientation of the skin layer. Apparently, the elastic modulus (at very low strain of 15  $\mu\text{m}$ ) is determined by the morphology of the skin layer.

The variations of the frequency (strain-rate) sensitivity coefficient,  $m$ , with the significant processing conditions are shown in Figure 3-14. Only  $v_i$  ( $\%p \approx 9\%$ ) and  $T_w$  ( $\%p \approx 49\%$ ) and their interaction  $v_i \times T_w$  ( $\%p \approx 9\%$ ) are significant factors, with a residual of 33%. The coefficient  $m$  decreases with the increase of  $v_i$  and  $T_w$ , see Figure 3-14a. At high  $T_w$ ,  $m$  does not change with variations of  $v_i$ , see Figure 3-14b. These variations of  $m$  with  $v_i$  and  $T_w$  are opposed to that of the index of crystallinity of the skin layer [30]. A more oriented skin layer seems to be less sensitive to variations of the strain-rate.

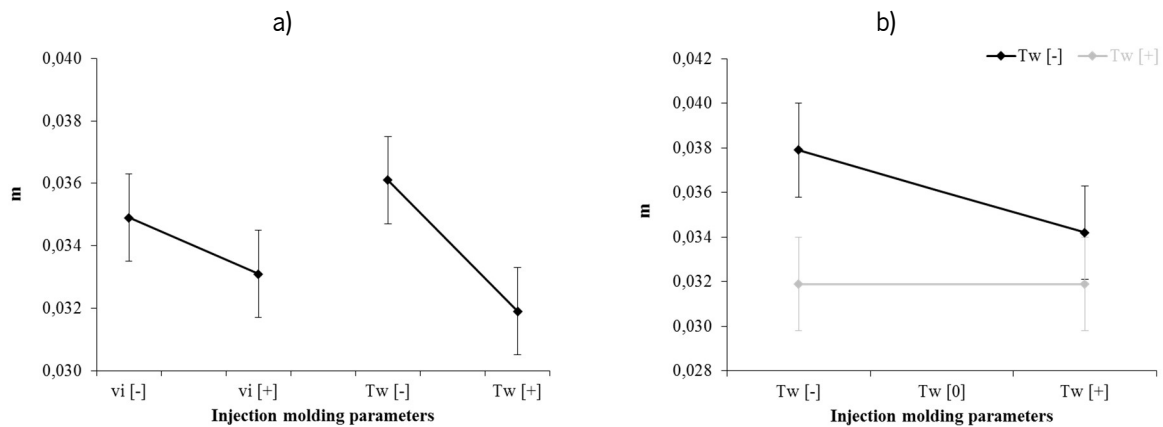


Figure 3-14. Variations of the frequency (strain-rate) sensitivity coefficient,  $m$ , with: a) significant processing conditions; and b) 2FI.

Interestingly, there are no variations of the activation energy,  $E_a$ , with the processing conditions. In fact, and as shown in Figure 3-9, all the  $a_T$  values for samples molded with different processing conditions lie on a straight line of the same slope. The variations of  $E_a$ , for all 25 different processing conditions are 1.6% (see Table 3-4), with an average value of  $368,1 \pm 1,5 \text{ kJmol}^{-1}$ . The constancy of  $E_a$ , suggests, as abovementioned, a similitude of the macromolecular movements of the amorphous phase regardless the morphology induced by processing.

Table 3-5 shows that the variables  $v_i$  and  $T_w$  (ranked in ascending order of relevance) are the most significant parameters in respect to the evaluated properties.  $P_h$  has a marginal effect. Surprisingly,  $T_i$  does not appear as a significant factor in spite of its normal great contribution for the properties of the moldings.  $v_i$  has a strong non-linear (quadratic) effect, mainly at high frequencies. The dependencies of

the  $\beta$ -relaxation  $\tan\delta$  parameters on the processing conditions exhibit high residuals (e.g. insignificant factors and interactions), i.e. the experimental scatter is high.

Table 3-5. Summary of the linear (1<sup>st</sup>-order) and non-linear ( $X^2$  and 2FI) effects of the processing conditions on the selected properties ( $\blacktriangle$  increase and  $\blacktriangledown$  decrease).

	$T_g$		$FWHM$		$A_\beta$		$E'_0$	$m$
	0.1 s <sup>-1</sup>	10 s <sup>-1</sup>	0.1 s <sup>-1</sup>	10 s <sup>-1</sup>	0.1 s <sup>-1</sup>	10 s <sup>-1</sup>		
$v_i$				$\blacktriangle$ (11)		$\blacktriangle \blacktriangledown$ (15)	$\blacktriangle$ (8)	$\blacktriangledown$ (9)
$T_i$					$\blacktriangledown$ (16)		$\blacktriangledown$ (12)	
$T_w$	$\blacktriangledown$ (21)	$\blacktriangledown$ (17)					$\blacktriangle$ (54)	$\blacktriangledown$ (49)
$P_h$					$\blacktriangledown$ (11)			
2FI			$v_i \times T_i$ (16) $T_w \times P_h$ (14)	$v_i \times T_w$ (10) $T_w \times P_h$ (8)				$v_i \times T_w$ (9) $v_i \times P_h$ (6)
$X^2$				$v_i^2$ (29)		$v_i^2$ (34) $T_w^2$ (11)		
Residuals	0,79	0,83	0,70	0,42	0,73	0,51	0,26	0,27

Data between parentheses stand for the % of contribution.

For this material, ANOVA results relate these quantities ( $E'_0$  and  $m$ ) with the significant processing conditions by a polynomial fits, as follows:

$$E'_0(\text{proc.}) = 1226.6 + 19.4 \times [v_i] - 24.0 \times [T_i] + 50.7 \times [T_w], R^2 = 0.74 \quad \text{Equation 3-4}$$

$$m(\text{proc.}) = 0.034 - 9.1e^{-4} \times [v_i] - 2.1e^{-3} \times [T_w] + 9.3e^{-4} \times [v_i] \times [T_w] + 7.8e^{-4} \times [v_i] \times [P_h], \\ R^2 = 0.73 \quad \text{Equation 3-5}$$

In Equation 3-4 and Equation 3-5, the values of the processing conditions are coded, i.e.  $[x] = 2 \left( \frac{v_j - \bar{v}}{d_j} \right)$ , where  $v_j$  is the uncoded factor value,  $\bar{v}$  the mean of the uncoded factors and  $d_j$  is the amplitude of variations of the factor.  $R^2$  is the coefficient of correlation of the model. These empirical relationships can be used for engineering practice.

### 3.5 Conclusions

The viscoelastic behavior of injection molded PP samples is evaluated by DMTA (isothermal frequency sweeps), over a range of temperatures and frequencies, and related to key injection molding conditions through an analysis of variance. The storage modulus ( $E'$ ) and damping factor ( $\tan\delta$ ) are investigated. The latter evidences the  $\beta$ -relaxation process from which, its magnitude ( $A_\beta$ ), the glass transition temperature ( $T_g$ ) and the homogeneity of the amorphous phase ( $FWHM$ ) are determined. Using the TTS principle (approximated by the Arrhenius law), the limited set of results obtained from the DMTA are expanded around a reference temperature to construct master curves ( $E'$  vs.  $f$ ) that provide a much wider frequency range.

A distinct behavior among injection molding experiments is observed reflecting a clear effect of the processing conditions on dynamic mechanical properties. Also, a marked effect of time and temperature on those properties is observed. The following conclusions are drawn from the analysis of experimental results:

- The storage modulus increases with decreasing temperature, while the damping factor decreases. But, by increasing the frequency the storage modulus increases, whereas the damping factor decreases. It is clear that  $E'$  and  $\tan\delta$  are strongly dependent and vary oppositely for frequency and temperature conditions. The relative variation of both  $E'$  and  $\tan\delta$  with temperature is higher at lower frequencies, and the variation with frequency is higher at higher temperatures.
- The absolute values of  $T_g$ ,  $FWHM$  and  $A_\beta$  among the 25 moldings are maximized when assessed at high frequencies. However, the relative variation of these parameters as a function of processing conditions is reduced for higher test frequencies.  $T_g$  decreases for higher  $T_w$  (higher degree of crystallinity of the skin layer) and this effect is magnified for lower frequencies.
- The results reveal that  $E'$  and  $\tan\delta$  are significantly dependent on the processing conditions. The sensitivity of  $E'$  on the processing conditions is maximized for lower test temperatures. On the other hand,  $\tan\delta$  sensitivity on processing is maximized for higher temperatures. Experiments with lower process thermal amplitudes, i.e. low injection temperature and high mold temperature, show the maximum  $E'$  values.

The storage static modulus ( $E'_0$ ), strain-rate sensitivity coefficient ( $m$ ) and activation energy ( $E_a$ ), were calculated within the representative frequency limits ( $10^{-3}$  to  $10^2$  s $^{-1}$ ) of the master curves. Among the 25 process induced morphologies, it is found a variation of 22% and 28% for the  $E'_0$  and  $m$ , respectively. Surprisingly, the  $E_a$  showed a neglected variation. The most significant factors, among the four controlled

injection moulding process parameters, for the response of  $E'_0$  and  $m$  is the mold wall temperature with a contribution of 54% and 49% for  $E'_0$  and  $m$ , respectively.

## References

1. V. Shah. Handbook of Plastics Testing and Failure Analysis, 3rd Edition. John Wiley & Sons, Inc. (2007).
2. P.V. Joseph, G. Mathew, K. Joseph, G. Groeninckx, and S. Thomas. Composites: Part A, 34, 275 (2003).
3. T. Abraham, K. Banik, and J. Karger-Kocsis. eXPRESS Polymer Letters, 1, 519 (2007).
4. M. Gahleitner, C. Grein, K. Bernreitner, B. Knogler, and E. Hebesberger. Journal of Thermal Analysis Calorimetry, 98, 623 (2009).
5. K.P. Menard. Dynamic Mechanical Analysis: Encyclopedia of Polymer Science and Technology. John Wiley & Sons, Inc. (2004).
6. J.F. Mano and J.C. Viana. Polymer Testing, 25, 953 (2006)
7. N.K. Dutta and G.H. Edward. Journal of Applied Polymer Science, 66, 1101 (1997).
8. B. Alcock, N.O. Cabrera, N.-M. Barkoula, C.T. Reynolds, L.E. Govaert, and T. Peijs. Composites Science and Technology, 67, 2061 (2007).
9. A.D. Drozdov. Mechanics of Time-Depend Materials, 14, 411 (2010).
10. F. Achereiner, K. Engelsing, M. Bastian, and P. Heidemeyer. Polymer Testing, 32, 447 (2013).
11. S. Díez-Gutiérrez, M.A. Rodríguez-Pérez, J.A. De Saja, and J.I. Velasco. Polymer, 40, 5345 (1999).
12. S. Tamrakar, R.A. Lopez-Anido, A. Kiziltas, and D.J. Gardner. Composites: Part A, 42, 834 (2011).
13. Y. Ji-Ru, X. Xiao-Lin, Z. Xing-Ping, Z. Hua-Min, and L. De-Qun. Chemical Research in Chinese Universities, 25, 573 (2009).
14. M. Hoyos, P. Tiemblo, and J.M. Gómez-Elvira. Polymer, 48, 183 (2007).
15. J. Li, H. Li, C. Wu, Y. Ke, D. Wang, Q. Li, L. Zhang, and Y. Hu. European Polymer Journal, 45, 2619 (2009).
16. C. Grein, K. Bernreitner, and M. Gahleitner. Journal of Applied Polymer Science, 93, 1854 (2004).
17. E. Andreassen. Polymer, 40, 3909 (1999).
18. C. Stern, A. Frick, and G. Weickert. Journal of Applied Polymer Science, 103, 519 (2007).
19. F.-J. Wortmann and K.V. Schulz. Polymer, 36, 1611 (1995).
20. T. Ariyama, Y. Mori, and K. Kaneko. Polymer Engineering and Science, 37, 81 (1997).
21. M. Hoyos, P. Tiemblo, and J.M. Gómez-Elvira. European Polymer Journal, 45, 1322 (2009).

22. S. Danesi, L. Baldi, and G. Ballini. *Rheologica Acta*, 13, 613 (1974).
23. E. Bociąga and T. Jaruga. *Journal of Achievements in Materials and Manufacturing Engineering*, 23, 83 (2007).
24. P. Postawa, T. Stachowiak, and T. Jaruga. *Archives of Materials Science and Engineering*, 44, 104 (2010).
25. C.N. Barbosa, F. Carvalho, J.C. Viana, M. Franzen, T. Baranowski, and R. Simoes. *International Journal of Materials and Product Technology* 52, 76 (2016).
26. J. Antony. *Design of Experiments for Engineers and Scientists*, 1st Edition. Elsevier Science & Technology Books (2003).
27. N.I.M. Yusoff, E. Chailleux, and G.D. Airey. *International Journal of Pavement Research and Technology*, 4, 324 (2011).
28. M. Tajvidi, R.H. Falk, and J.C. Hermanson. *Journal of Applied Polymer Science*, 97, 1995 (2005).
29. Steven Eric Zeltmann, B.R. Bharath Kumar, Mrityunjay Doddamani, and Nikhil Gupta. *Polymer*, 101, 1 (2016).
30. C.N. Barbosa, R. Simoes, M. Franzen, T. Baranowski, and J.C. Viana. *Polymer Engineering and Science*, DOI: 10.1002/pen.24650 (2017).
31. R. Picciochi, Y. Wang, N. Alves, and J.F. Mano. *Colloid and Polymer Science*, 285, 575 (2007).
32. E. Passaglia and G.M. Martin. *Journal of Research of the National Bureau of Standards – A. Physics and Chemistry*, 68A, 529 (1964).

## 4. APPLYING FLOW SIMULATIONS IN THE DEVELOPMENT PROCESS OF INJECTION MOLDED THERMOPLASTIC PARTS

This chapter is based on the scientific paper published elsewhere:

C.N. Barbosa, F. Carvalho, J.C. Viana, M. Franzen, T. Baranowski, and R. Simoes. *Int. J. Mater. Prod. Tec.*, 52, 76 (2016).

### Abstract

The main challenge of this contribution pertains to the local prediction of mechanical properties over the entire domain of an injection moulded unreinforced thermoplastic component as a function of process settings by means of flow simulations. Current state-of-the-art prediction capabilities are limited and thus hamper the advantage of simulations in the product development process. In the proposed approach, a dedicated computer application allows importing computer aided flow study results from the Autodesk Moldflow Insight package and locally, i.e. per element of the meshed model, characterising the thermo-mechanical environment (TME). Cooling and thermo-stress indices (at the end of filling, packing, and cooling phases), are used to characterise the local thermal and mechanical environment during the injection moulding process. The prediction of the Young's modulus through the TME assessment for certain regions of the thermoplastic automotive component (door panel) was accomplished and compared to experimental results, having shown good agreement, thus validating the proposed approach.

### 4.1 Introduction

The process of designing, developing and producing plastic components is currently rather undertaken by computer-aided software. Particularly in the case of plastic injection moulding industry, these software packages play a major role in product design and development processes. In the automotive industry, plastic components are mandatory to accomplish important and tight requirements concurrently (e.g. crash safety, durability, toughness, resiliency, low cost, design flexibility, etc.) which demands for

continuous research and improvement. Although limited, such engineering requirements are nowadays foreseen through computer-aided engineering (CAE) software, avoiding costly prototypes and extensive lab testing.

The plastic injection moulding industry has been recognising that CAE enhances engineers' ability to handle all aspects of the polymer moulding, benefiting productivity, product quality, and profitability ratios. The simulation of injection moulding process is fairly the most successful example of simulation for any plastic forming process [1]. In this case, CAE analysis provides important design data of the moulding process, such as spatial distributions of pressure, temperature, shear rate and stress, and velocity. These outputs are the combined effect of the processing conditions, the part geometry, and the intrinsic thermo-rheological properties of the material, causing a specific thermo-mechanical environment (TME). Such inter-relations tailor the local mechanical properties of an injection moulded thermoplastic part [2].

The notion that processing technology and process settings have a dramatic effect on the quality of the moulded article is known since plastic processing began. There is extensive evidence to relate the mechanical properties of plastic components to the morphology developed on the polymer (e.g. crystalline structure, degree of crystallinity, molecular orientation, skin ratio, etc.) during the injection moulding process. Relationships between moulding conditions and properties [3], and morphology [4, 5] have been generally reported. Some studies have shown the relationships between polymer structure and final properties [6] and others have focused on the relationships between the thermo-mechanical processing environment and the mechanical properties [7-9].

The prediction of mechanical properties based on injection moulding simulation was investigated in for static loads and for simple parts using a micro model-based calculation [10]. Even as those results were promising, the calculation time and further limitation did not enable this approach to be implemented into industrial practice. Kagan et al. used the injection moulding simulation as a fundamental engineering tool to discuss the mechanical properties of glass fibre reinforced nylon in local and bulk areas of automotive cooling fans under the influence of moulding and end-use conditions [11]. Other researchers have validated experimentally the morphology simulation in glass fibre polycarbonate discs as a function of melt temperature and flow rate using Moldflow simulations [12]. It was reported a qualitative agreement in terms of the evolution of fibre orientation along the flow path and a quantitative agreement between predictions and experimental fibre orientation results was observed close to the wall and at the midplane. Other authors aimed at predicting the mechanical properties of injection moulded short fibre reinforced thermoplastics through an integrated approach starting from rheology of the material, orientation equation, interaction parameter and closure approximation [13]. In this work, the resulting local fibre



orientation distribution is used to predict anisotropic mechanical properties of the part using classical analytical homogenisation theories based on the computed orientation tensors and numerical homogenisation by generating a representative elementary volume.

Most of the interior automotive components are made of injection moulded polypropylene (PP) and, therefore, this type of material and processing technology were selected for this study. Autodesk Moldflow Insight (AMI) software was used to perform injection moulding simulations. A computer application was developed to compute the thermo-mechanical indices (TMI) and translate specific TME in local mechanical properties.

In this study, the authors have expanded the TMI methodology, initially proposed by Viana et al. [9] and more recently published by Barbosa et al. [8], to consider the complete injection moulding cycle, i.e. filling, packing and cooling phases. This methodology is fully embedded in the developed predictive computer application. Though mature, the available CAE software solutions are still limited in their capabilities to predict local mechanical properties, mainly for unreinforced materials. The proposed integrated approach can be thought of as a valuable and powerful engineering tool for complementing existing CAE solutions.

## **4.2 Injection moulding simulation**

The effects of mould/part design features, changes in process variables and/or type of material on the final part quality can be inferred by means of CAE analysis without extensive experimentation. The available software packages calculate physical phenomena such as pressure drops, shrinkage, warpage, cooling characteristics, part defects, etc. However, such predictions are still under continuous optimisation.

Most of the CAE software for polymer processing (e.g. injection moulding) use finite or discrete element methods. Basically, the continuum is divided into a finite number of parts (elements) and the solution of the complete system is an assembly of its elements [14]. In AMI simulations, the part model must have an appropriate finite element discretisation in the form of a mesh. Elements divide the geometry (domain) of the part into a large number of very small domains. Elements, categorised as beam, triangle or tetrahedron, are defined by nodes and are used for the calculations inside AMI which uses three mesh types for analysis: midplane, fusion (sometimes also called modified 2.5D mesh), or 3D. For midplane and fusion meshes, the solvers are based on the generalised Hele-Shaw flow model and follow the assumptions [1]:

- laminar flow of a generalised Newtonian fluid;
- inertia and gravity effects can be ignored;
- in-plane heat conduction is negligible compared to conduction in the thickness direction;
- thermal convection in the thickness direction is neglected;
- heat loss from edges can be ignored for the triangular element type.

In the fusion mesh type, triangles (three-node elements) are defined on the surface of the plastic cross section. An analysis method called *Dual Domain*<sup>™</sup> is applied which removes the need to midplane the geometry and significantly reduces the model preparation time. It works by simulating the flow of the melt on both the top and bottom parts of the mould cavity [15]. The aforesaid mesh and method have been used in this research. An interesting work describes the practical and scientific aspects of the injection moulding simulation [2]. It provides an introduction to the history of injection moulding simulation from both academic and commercial viewpoints. The geometry and material data problem are examined and solutions are provided to increase usage of simulation and to improve accuracy of shrinkage and warpage prediction.

### 4.3 Thermo-mechanical environment in injection moulding

In the case of injection moulding process, the combined effect of the processing variables, the part geometry, the type of flow and the thermo-rheological properties of the material should be taken into account while characterising the TME, since they create specific profiles of pressure, heat transfer (melt and mould temperatures, viscous dissipation), shear rate, shear stress [8]. These are designated thermo-mechanical variables (TMV) and are responsible for the development of different TME within the spatial domain of the moulding parts.

#### 4.3.1 Thermo-mechanical variables

The TMV can be estimated by computer simulations of the injection moulding process or by adequate mould instrumentation (local pressures and temperatures). In this study, the local specific profiles of pressure, temperature, and shear stress as well as the frozen layer developed over the whole injection moulding process cycle were computed, based on the outputs of the AMI simulation package.

### 4.3.2 Thermo-mechanical indices

The use of the TMI methodology has been suggested to correlate the processing conditions with the developed microstructure and the resulting mechanical properties [5, 8]. In this study, we have expanded the TMI methodology to study the filling, packing and cooling phases, considering two indices:

- a) cooling index (CI), that quantifies the thermal level of the core and serves as an indirect evaluation of the crystallisation process of the core region;
- b) thermal-stress index (TSI), that indirectly assesses the orientation level of the skin.

The computation of both TMI is estimated along the timeline of the injection moulding cycle and enables the prediction of the mechanical properties per mesh element, based on the outputs of the AMI simulation package.

#### a. Cooling index, $Y_c$

The CI,  $Y_c$ , is defined as the ratio between the overheating and the cooling temperature difference. The cooling index at the end of the moulding cycle is calculated locally (at mesh element) as a weighted average, by the relative duration of the filling, packing and cooling phases. The specific cooling index at the end of filling is given by Equation 4-1.

$$Y_c^f = \frac{T_b^f - T_c^f}{T_b^f - T_i^f} \quad \text{Equation 4-1}$$

$T_b^f$  is the local bulk temperature at the end of filling phase;  $T_c^f$  is the crystallization temperature, given by Equation 4-2;  $T_i^f$  is the temperature at the mould/polymer interface at the end of filling phase, given by Equation 4-3.

$$T_c^f = T_c^* + b_6 \times P^f \quad \text{Equation 4-2}$$

$T_c^*$  is the crystallization temperature of the material (assumed constant);  $b_6$  is a rheological constant;

$P^f$  is the local maximum pressure during the filling phase.

$$T_i^f = \frac{\left( \sqrt{k^f \rho^f C_p^f} \right)_p \times T_b^f + \left( \sqrt{k \rho C_p} \right)_m \times T_w}{\left( \sqrt{k^f \rho^f C_p^f} \right)_p + \left( \sqrt{k \rho C_p} \right)_m} \quad \text{Equation 4-3}$$

Where <sub>p</sub> stands for the polymer materials; <sub>m</sub> stands for the mould material.  $k^f$ ,  $\rho^f$ , and  $C_p^f$  are the thermal conductivity, the density, and the specific heat of the polymer, at the end of the filling phase.  $k^f$  and  $C_p^f$  are variables dependent on the bulk temperature ( $T_b^f$ ) and,  $\rho^f$  is a function of the pressure ( $P^f$ ) and  $T_b^f$ ; all are calculated at mesh element.  $k$ ,  $\rho$ , and  $C_p$  stand for the thermal conductivity, the density, and the specific heat of the mould material (generally steel).  $T_w$  is the cooling fluid (mould wall) temperature.

The cooling index at the end of packing phase is calculated as a weighted average, by the relative duration of the filling and packing phases, according to Equation 4-4.

$$Y_c^{fp} = \frac{Y_c^f \times t^f + Y_c^p \times t^p}{t^f + t^p} \quad \text{Equation 4-4}$$

$Y_c^p$  means the specific cooling index of the packing phase and is given by Equation 4-5.  $t^f$  and  $t^p$  are the specific time of the filling and packing phases, respectively.

$$Y_c^p = \frac{T_b^p - T_c^p}{T_b^p - T_i^p} \quad \text{Equation 4-5}$$

$T_b^P$  is the local bulk temperature at the end of packing phase;  $T_c^P$  is the crystallization temperature, given by Equation 4-6;  $T_i^P$  is the temperature at the mold/polymer interface at the end of packing phase, given by Equation 4-7.

$$T_c^P = T_c^* + b_6 \times P^P \quad \text{Equation 4-6}$$

$P^P$  is the local averaged pressure during the packing stage.

$$T_i^P = \frac{\left( \sqrt{k^P \rho^P C_p^P} \right)_p \times T_b^P + \left( \sqrt{k \rho C_p} \right)_m \times T_w}{\left( \sqrt{k^P \rho^P C_p^P} \right)_p + \left( \sqrt{k \rho C_p} \right)_m} \quad \text{Equation 4-7}$$

$k^p$ ,  $\rho^p$ , and  $C_p^p$  represent the thermal conductivity, the density, and the specific heat of the polymer, at the end of packing phase.  $k^p$  and  $C_p^p$  are variables dependent on the bulk temperature ( $T_b^P$ ) and,  $\rho^p$  is a function of the pressure ( $P^P$ ) and  $T_b^P$ ; all are calculated at mesh element.

The cooling index at the end of cooling phase is calculated as a weighted average, by the relative duration of the filling, packing and cooling phases, and is given by Equation 4-8.

$$Y_c^{fpc} = \frac{Y_c^f \times t^f + Y_c^p \times t^p + Y_c^c \times t^c}{t^f + t^p + t^c} \quad \text{Equation 4-8}$$

$Y_c^c$  means the specific cooling index of the cooling phase and is given by Equation 4-9.  $t^c$  is the specific time of the cooling phase.

$$Y_c^c = \frac{T_b^c - T_c^c}{T_b^c - T_i^c} \quad \text{Equation 4-9}$$

$T_b^c$  represents the local bulk temperatures at  $t^c$ ;  $T_c^c$  mean the crystallization temperature at  $t^c$ , given by Equation 4-10;  $T_i^c$  stands for the temperature at the mould/polymer interface at  $t^c$ , given by Equation 4-11.

$$T_c^c = T_c^* + b_6 \times P^c \quad \text{Equation 4-10}$$

$P^c$  is the local averaged pressure during  $t^c$ ; commonly reports residual/holdover and/or null values.

$$T_i^c = \frac{\left( \sqrt{k^c \rho^c C_p^c} \right)_p \times T_b^c + \left( \sqrt{k \rho C_p} \right)_m \times T_w}{\left( \sqrt{k^c \rho^c C_p^c} \right)_p + \left( \sqrt{k \rho C_p} \right)_m} \quad \text{Equation 4-11}$$

$k^c$ ,  $\rho^c$ , and  $C_p^c$  mean the thermal conductivity, the density, and the specific heat of the polymer, at  $t^c$ .  $k^c$  and  $C_p^c$  are variables dependent on the bulk temperature ( $T_b^c$ ) and,  $\rho^c$  is a function of the pressure ( $P^c$ ) and  $T_b^c$ ; all are calculated locally at mesh element.

All mesh elements share the same time instant at the end of filling phase. On the other hand, the packing and cooling times are determined independently for each mesh element. The instant at the end of packing is given by the instant immediately before the shear stress at wall reaches the first null report.  $t^c$  designates the cooling phase at the instant of a full solidified layer (i.e. the bulk temperature of a given cross section of the part is well below the polymer crystallization temperature) or maximum reported value post-packing (it can happen not reaching a full solidified layer before ejection).

**b. Thermo-stress index,  $\tau_Y$**

The TSI,  $\tau_{Ys}$ , is associated to the flow-induced orientation of the melt (indirectly inferred by the maximum wall shear stress) and to the molecular relaxation occurring before polymer crystallization temperature is reached. The thermo-stress index is calculated at the end of each injection moulding phase. At the end of filling, the TSI is determined by Equation 4-12.

$$\tau_{Ys}^f = \frac{\tau_w^f \times O_s^{xyz}}{e^{\frac{Y^f}{c}}} \quad \text{Equation 4-12}$$

The exponential decay has been used as an arithmetic artifice to avoid negative values.  $\tau_w^f$  is the local maximum shear stress at wall reported during the filling phase.  $O_s^{xyz}$  stands for the direction of flow (or shear direction) that is the most probable molecular orientation at skin.

The TSI at the end of packing is calculated as a weighted average, by the relative shear stress at wall during the filling and packing, according to Equation 4-13.

$$\tau_{Ys}^{fp} = \frac{\tau_w^{fp}}{e^{\frac{Y^{fp}}{c}}} \quad \text{Equation 4-13}$$

$\tau_w^{fp}$  is the weighed shear stress at wall at the end of packing and is obtained through Equation 4-14.

$$\tau_w^{fp} = \frac{\tau_w^f \times L_s^f \times O_s^{xyz} + \tau_w^p \times (L_s^p - L_s^f)}{L_s^p} \quad \text{Equation 4-14}$$

$L_s^f$  and  $L_s^p$  are the frozen layer fraction ( $0 \leq L_s \leq 1$ ) at the end of filling and packing phases, respectively;  $\tau_w^p$  is the local averaged shear stress at wall reported during the packing phase.

At the end of cooling phase, the TSI is determined by Equation 4-15.

$$\tau_{Ys}^{fpc} = \frac{\tau_w^{fpc}}{e^c} \quad \text{Equation 4-15}$$

$\tau_w^{fpc}$  Equation 4-16 represents the relative shear stress at wall at  $t^c$  ( $Ls^c = 1$  or maximum value reported during cooling). Note that during cooling no flow is presented in the mould cavity, thus the shear stress at wall values at  $t^c$  ( $\tau_w^c$ ) are null.

$$\tau_w^{fpc} = \frac{\tau_w^f \times Ls^f \times O_s^{xyz} + \tau_w^p \times (Ls^p - Ls^f) + \tau_w^c \times (Ls^c - Ls^p)}{Ls^c}$$

$$\Leftrightarrow \tau_w^{fpc} = \frac{\tau_w^f \times Ls^f \times O_s^{xyz} + \tau_w^p \times (Ls^p - Ls^f)}{Ls^c} \quad \text{Equation 4-16}$$

#### 4.4 TMI predictive tool

The TMI predictive tool was developed in native C language programming to parse simulation outputs which, in turn, are stored in an embedded database. A frontend application has also been developed in C#, allowing faster results analysis. This software consists of importing relevant results from plastics computer flow simulations and, accordingly, predicting the local mechanical properties of a midplane or dual domain finite element model meshes. The integrated computational flow chart and all mandatory parameters are summarised in Figure 4-1.

All relevant Moldflow data, at the finite element level and at the end of each injection moulding phase, can be exported into different formats (txt, xls, xml). This application computes the mechanical properties (per mesh element) based on the previous TMI methodology and a set of regression equations resulting from both Moldflow simulations and experimental analyses. It is simply required to import into a single root directory a set of mandatory outputs from AMI study reports. The required files are grouped in three distinct functional clusters:

- 1) the geometrical definition of the component;
- 2) set of processing conditions, including material (polymer and mould material) specific properties;
- 3) the TMV for all the time instants of the injection moulding process.



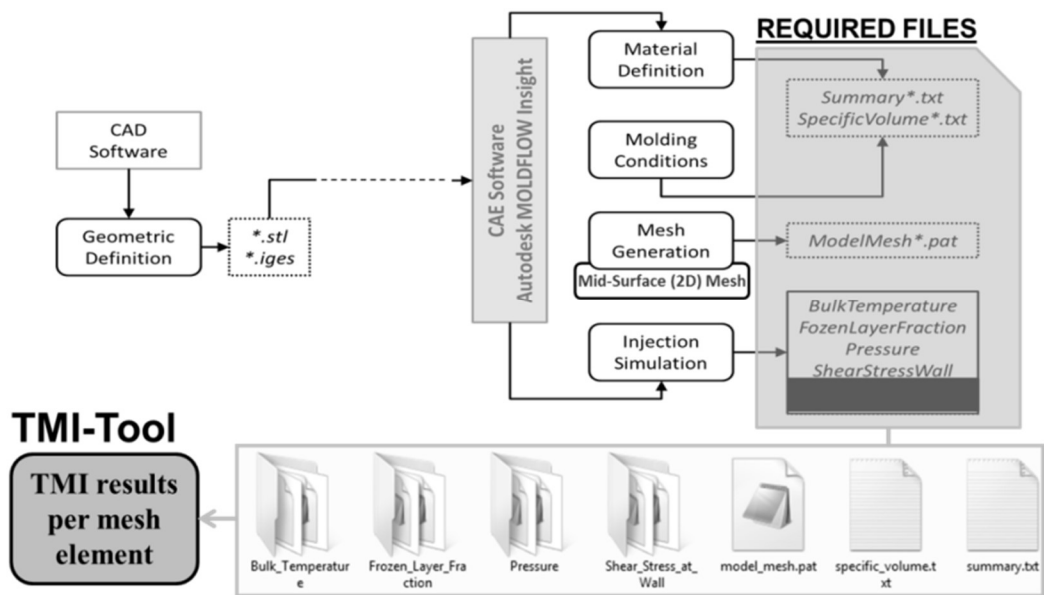


Figure 4-1. Flow chart scheme for the TMI computation and prediction of the mechanical properties at model mesh element level (see online version for colours).

## 4.5 Experimental design

### 4.5.1 Importing and meshing

The injection moulding process of a thermoplastic door panel used in the automotive industry was simulated with the software Autodesk Moldflow Insight [15].

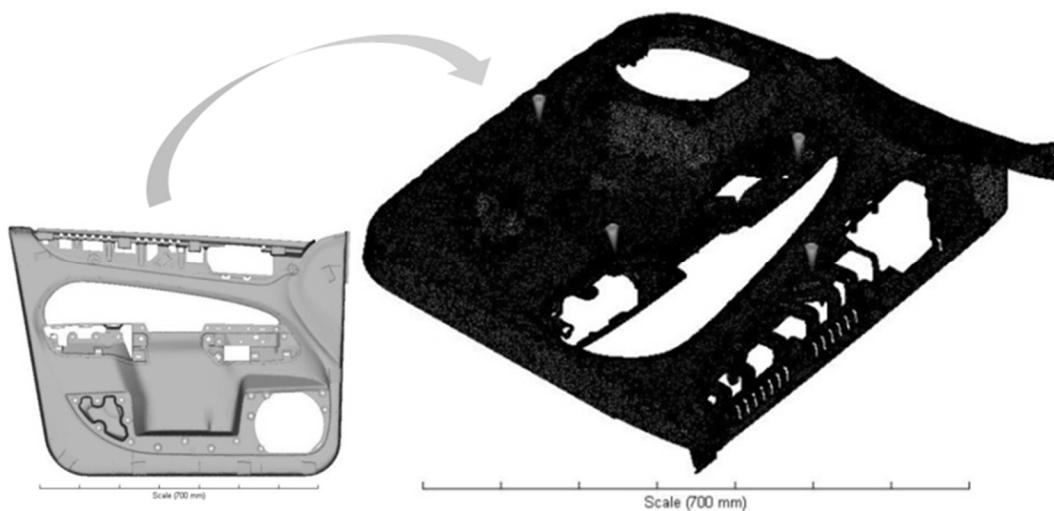


Figure 4-2. CAD model to mesh, (a) the imported STL file and the scaled-up image (b) the finite element post-processed mesh model with four gate locations (yellow cones) (see online version for colours).

The part's geometry was imported into AMI and the finite element mesh required to run a simulation was generated (see Figure 4-2). A fusion mesh type was then postprocessed, according to the best practices [1]. It is noticeable the fineness of the finite element mesh model. The part has as fairly an average wall thickness of 3.0 mm. Next, it is shown the diagnosis of the most important statistic results of the post-processed mesh.

- triangles: 242,462
- nodes: 121,073
- surface area: 12,813.9 cm<sup>2</sup>
- volume: 1,538.18 cm<sup>3</sup>
- average aspect ratio: 2.23
- maximum aspect ratio: 19.0
- free edges: 0
- manifold edges: 363,693
- non-manifold edges: 0
- elements not oriented: 0
- element interceptions: 0
- fully overlapping elements: 0
- match percentage: 89.0%
- reciprocal percentage: 85.2
- minimum mesh thickness: 0.42 mm
- maximum mesh thickness: 6.2 mm

#### 4.5.2 Moulding window size and simulation design

The moulding window (MW) analysis was carried out on the door panel to assess the boundary/feasible conditions of the injection moulding process for a given material, in this case an unfilled PP. The selected injection moulding machine specifies 180 MPa of maximum injection pressure and 7,000 tonne of maximum clamp force. The part was moulded with four gates indicated by the marked cones in Figure 4-2b; sprues and runners are excluded from the analysis. The injection moulding locations have been previously defined by the mould maker company. For better visualisation, the nodes of the triangular elements have been hidden from the model.

Varying the processing temperatures (melt and mould) and injection time, the analysis recommends an acceptable moulding window for the part. The preferred moulding zone (or 'green region') is confined by the following specifications [1]:

- pressure less than 50% of machine capacity;
- flow front temperature, within  $\pm 10^{\circ}\text{C}$  from the melt temperature;
- shear stress, less than the shear stress limit for the material;
- shear rate, less than the shear rate limit for the material;
- clamp force, less than 80% of the machine capacity.

The injection melt temperature ( $T_i$ ) range was defined as 200 °C for the minimum value and 280 °C for the maximum value. The mould temperature ( $T_w$ ) range was specified as 10 °C for the minimum level and 70 °C for the maximum level. The range of both processing temperatures was defined according to the recommended processing conditions provided by the material supplier.

First of all, it is mandatory to check how the injection pressure varies with changes in the mould temperature, melt temperature, and injection time. The maximum required injection pressure should be less than 50% of machine capacity. Figure 4-3 plots the injection pressure (or pressure drop) as a function of the injection time ( $t_i$ ) for all combinations of the processing temperatures. It is observed that the melt temperature is the processing parameter that most affects the injection pressure response. The upper curves correspond to lower melt temperatures which lead to higher viscosities thus higher pressures. The injection time shows an apparent effect on the pressure, i.e. lower injection times corresponds to higher flow rates (or injection velocity) which requires higher pressures. Finally, the mould temperature plays a minor role on the development of the injection pressure profile: at lower injection times, the effect of the mould temperature is neglected due to the viscous dissipation effect prevented from high flow rates; and at higher injection times the significance of the mould temperature arises, mainly combined with low melt temperatures, due to the rapid solidification process of the material inside the mould cavity.

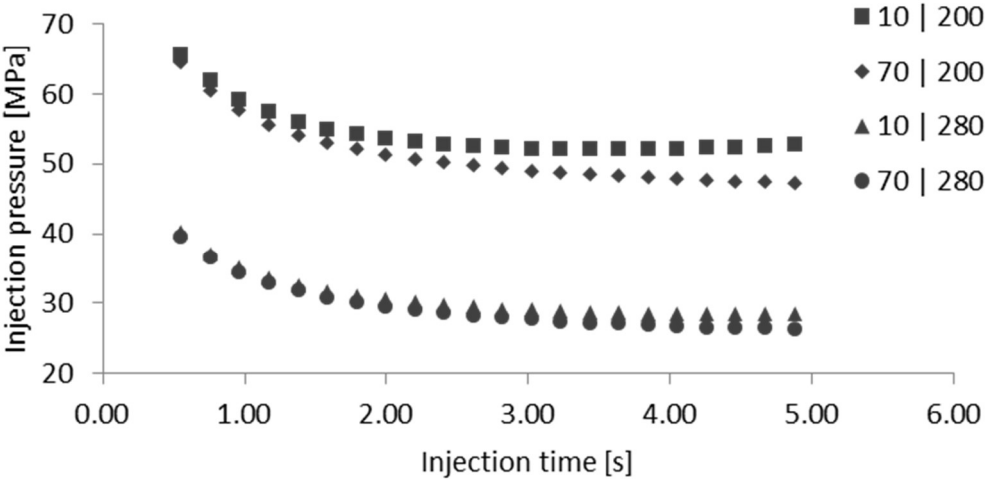


Figure 4-3. XY plot of the maximum pressure drop as a function of the injection time for the considered combinations of processing temperatures.

The highest injection pressure was 64 MPa and sticks to the combination of low levels of processing temperatures and injection time. On the other hand, the lowest injection pressure required is of 26 MPa and corresponds to the combination of high levels of processing temperatures and  $t_i$ . Therefore, the

maximum injection pressure needed to fill the part within these processing conditions is still less than 50% of the maximum pressure (180 MPa) of the machine.

Another important ‘green region’ specification is related to the temperature at the flow front. Figure 4-4 shows the flow front temperature over a range of injection times and processing temperatures, abovementioned. In this plot it is observed a wide processing window concerning melt and mould temperatures as well as an acceptable range of injection moulding times.

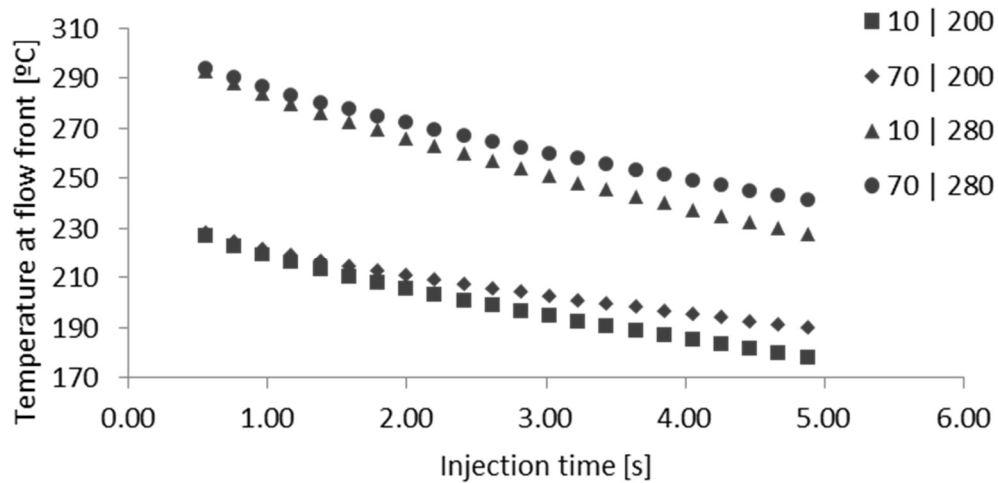


Figure 4-4. XY plot of the flow front temperature as a function of the injection time for the considered combinations of processing temperatures.

The higher the thermal amplitudes ( $T_i - T_w$ ) the more restricted is the  $t_i$  window, i.e. the difference between  $t_i^{max}$  (low flow rate) and  $t_i^{min}$  (high flow rate) is smaller. As a result, a more flexible processing molding window is achieved by combining high  $T_w$  with low  $T_i$ . Table 4-1 complements the plot above and resumes the minimum injection times,  $t_i^{min}$ , and maximum injection times,  $t_i^{max}$ , to keep the temperature at the flow front within  $\pm 10$  °C from the melt temperature.

Table 4-1. Boundary injection times as a function of the processing temperatures.

Injection time (s)	Mould temperature ( $T_w$ )   Melt temperature ( $T_i$ )			
	10   200 (°C)	10   280 (°C)	70   200 (°C)	70   280 (°C)
$t_i^{min}$	1.623	0.657	2.088	0.755
$t_i^{max}$	3.505	1.735	4.880	2.156

According to the data sheet of this material, the maximum shear rate value is  $100,000 \text{ s}^{-1}$  and the maximum shear stress was found to be 0.26 MPa. Figures 5 and 6 plot the evolution of shear rate and

shear stress, respectively, as a function of the injection time and processing temperatures. The shear rate only depends on the flow rate and no material degradation is foreseen since the maximum value reported (12,791 s<sup>-1</sup>) is well below the maximum shear rate for this material. The shear stress plot is similar to the XY plot of the maximum pressure shown above. Higher injection times, or lower flow rates, reduce somehow the shear stress. Also, higher melt temperatures induce less viscosity to the material which reduces significantly the shear stress. The mould temperature shows as well an effect on the shear stress, mainly for lower melt temperatures conditions, and decreases by increasing  $T_w$ . Therefore, neither the shear rate nor the shear stress, are limiting factors to achieve a preferred moulding zone.

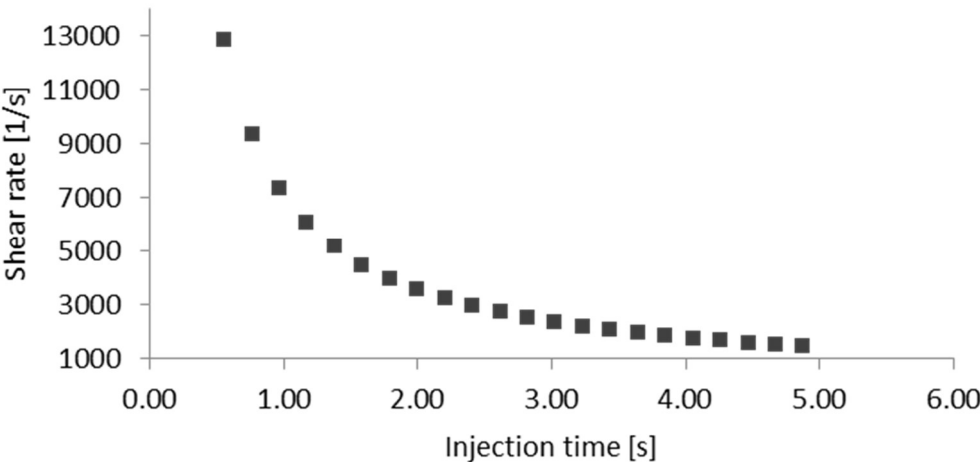


Figure 4-5. XY plot of the shear rate as a function of the injection time.

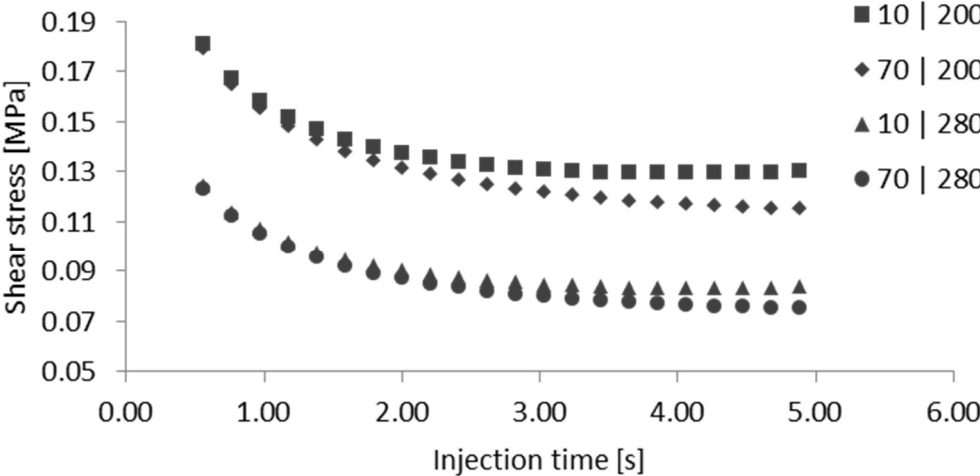


Figure 4-6. XY plot of the shear stress as a function of the injection time for the considered combinations of processing temperatures.

Regarding the packing (or holding) pressure,  $P_h$ , this is generally considered as 80 to 100% of the pressure required to fill the part, however can be much higher or lower and is often changed in the process of optimisation [1]. Taking in consideration the process settings at their minimum levels ( $t_i = 0.755$  s,  $T_w = 10$  °C and  $T_i = 200$  °C), the packing pressure was defined as 50 MPa (ca. 80%).

The holding time,  $t_h$ , was determined by sequentially increase  $P_h$  time from 5 to 30 seconds in order to identify the instant at which the part weight no longer increases, i.e. the gate freezes. For this exercise, the processing temperatures were defined at their maximum levels ( $T_w = 70$ °C and  $T_i = 280$ °C) and the injection time at lower level ( $t_h = 0.755$ s). The part weight stabilises at 20 s, as seen in Figure 4-7. This has been defined as the end of packing instant.

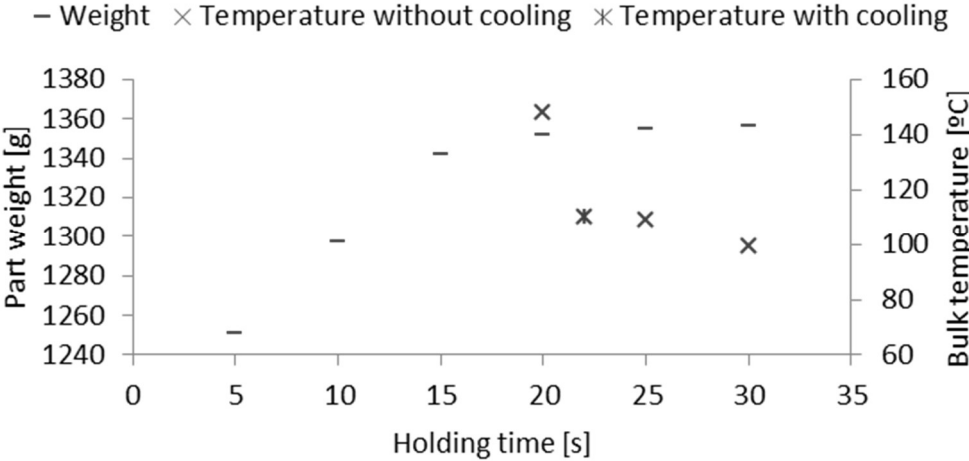


Figure 4-7. 95<sup>th</sup> percentile results of the holding/packing time versus part weight and bulk temperature.

The cooling time was defined according to the 95<sup>th</sup> percentile results of the frozen layer fraction and bulk temperature. The frozen layer fraction result, ranging from zero (polymer melt or flow layer) to one (part thickness fully frozen), is used in conjunction with the time to reach ejection temperature which should falls below the transition temperature. It was verified that at the instant at the end of packing (20 s) 95% of the thickness in the entire domain of the door panel was already frozen. Indeed, the bulk temperature was found to be the limiting factor rather than the frozen layer fraction. Figure 4-7 shows that at the instant 20 s, the 95<sup>th</sup> percentile of the bulk temperature is above the transition temperature which is around 120 °C for this specific material. Then, a cooling time ( $t_c$ ) of 2 seconds was specified and the bulk temperature dropped below the objective temperature.

Finally, the clamp force is a function of injection pressure and the projected area of the part observed during filling and packing. Higher injection pressures lead to higher clamping forces. In this way, it was considered to analyse this result by performing a simulation with the processing conditions set at their minimum levels. The result (ca. 1,100 tonne) was far less than 80% of the maximum machine capacity allowing a good resultant value of the pressure distribution over the entire part.

In summary, for this specific material and geometry, and imposed boundary conditions, the injection moulding times must  $\in ]1.623s, 2.156s[$  to achieve a preferred moulding window (high quality part) avoiding that shear rate and shear stress reach the maximum values, as well as to keep the flow front temperature at  $\pm 10^\circ\text{C}$  maximum from the melt temperature. Based on this, two extreme set of processing conditions were chosen to evaluate their effect on the TMI and thus on the predicted mechanical properties of the door panel within injection simulation. Table 4-2 summarises the experimental design.

Table 4-2. Injection moulding simulation design.

Simulation	$t_i$ (s)	$T_{mould}$ ( $^\circ\text{C}$ )	$T_{melt}$ ( $^\circ\text{C}$ )	$P_h$ (MPa)	$t_h$ (s)	$t_c$ (s)
#1	2.15	10	200	50	20	2
#2	1.63	70	280	50	20	2

Simulation#1 uses high injection time (low flow rate) and processing temperatures at their minimum level. Inversely, simulation#2 uses low injection time (high flow rate) and processing temperatures at their maximum level. For both simulations the packing/holding pressure ( $P_h = 50\text{ MPa}$ ), packing/holding time ( $t_h = 20\text{ s}$ ), and cooling time ( $t_c = 2\text{ s}$ ) were kept constant. The switch-over pressure was fixed at 99% of the volume filled.

### 4.6 Results and discussion

Fill and subsequent pack analyses were carried out according to the previous injection moulding simulation design. The TMI were computed in specific regions of the door panel for both injection simulations. Figure 4-8 shows the 3D model (STL file) of the door panel and the respective areas of interest (AOI) labelled from 1 to 5, and the theoretical injection locations represented by black spots.

Table 4-3 summarises the TMI results at the end of each injection moulding phase (filling, packing and cooling) for the AOI#1-4 of both moulding simulations. Each AOI is defined by at least 150 finite mesh elements and the tabulated results represent the average values of both TMI, normalised relatively to the

maximum, for both simulations. According to the data, sharp differences between the TMI are detected between conditions and selected areas.

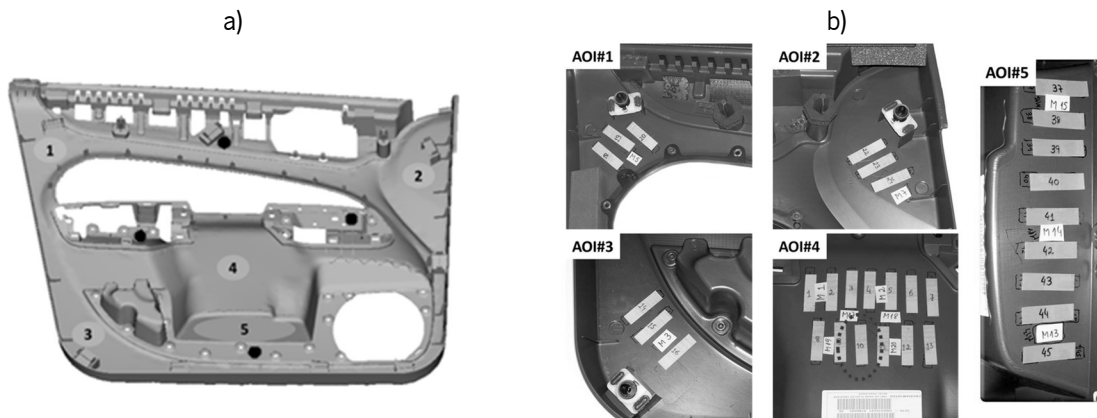


Figure 4-8. a) STL model of the door panel with the respective labels of the AOI and the injection moulding locations marked in black spots; b) AOI labelling in the physical component: AOI#1 (tags 18-20); AOI#2 (tags 22-24); AOI#3 (tags 14-16); AOI#4 (tag 10 marked with a dashed line); and AOI#5 (tags 37-45).

Table 4-3. TMI (normalized) results of the two extreme processing conditions for all regions of interest.

TMI	Simulation	Area of interest (AOI)			
		1	2	3	4
$Y_c^f$	1	1.00	0.94	0.93	0.84
	2	1.00	0.98	0.98	0.97
$Y_c^{fp}$	1	0.78	0.79	0.85	1.00
	2	0.91	1.00	0.81	0.69
$Y_c^{fpc1}$	1	0.85	0.83	0.88	1.00
	2	0.93	1.00	0.90	0.78
$\tau_{Ys}^f$	1	1.00	0.85	0.70	0.62
	2	1.00	0.83	0.79	0.60
$\tau_{Ys}^{fp}$	1	0.99	1.00	0.60	0.63
	2	0.77	1.00	0.50	0.63
$\tau_{Ys}^{fpc1}$	1	1.00	0.95	0.50	0.55
	2	0.87	1.00	0.58	0.80

It was previously mentioned that different processing conditions (mainly: processing temperatures, injection speed and packing pressure), gate locations, runners and feed systems, raw materials and part geometry lead to different TMEs, consequently to specific morphology development and, therefore, to different mechanical responses. Also, different regions of the part may show specific local properties. The main objective of the TMI methodology is to reflect trustworthily these variations. Mechanical



characterisation was carried out on small tensile (see Figure 4-8b). The samples were obtained from the drawn AOI using a punch press. Just one sample was tested due to the unavailability of extra door panels, making statistical analysis unfeasible.

The computation of the TMI for the specific AOI#5 was carried out and the correlation with the mechanical properties (in this case the Young's modulus) was found using a linear regression surface through a computer program *TableCurve 3D 4.0 free trial version* that combines a powerful surface filter with the ability of finding the ideal equation to describe three dimensional empirical data. The equation that describes this relationship was then used to predict the same property for the remaining AOI.

Based on the experimental results, a 3D plot surface was drawn to find the best-simplest relationships between the TMI and the Young's modulus of AOI#5, as aforementioned. The resultant mathematical equation [ $z = a + bx + cy$ , where  $a = 0.71001$ ,  $b = -0.13276$ , and  $c = 4.13105$ ] was applied to compute the envisaged property for the AOI#1-4. Figure 4-9 shows that the thermo-stress index governs the Young's modulus response and that higher TSI values lead to stiffer (higher Young's modulus) regions.

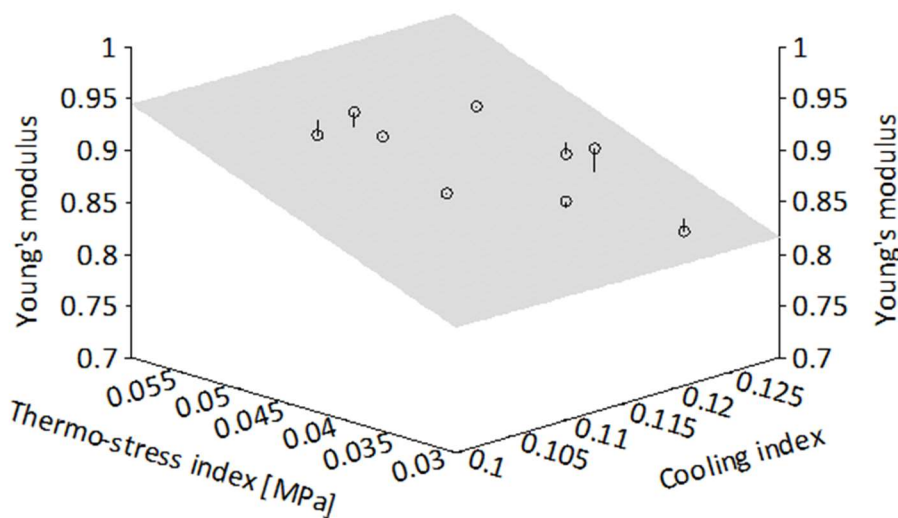


Figure 4-9. Variation of the Young's modulus with the TMI for the AOI#5 ( $R^2 = 0.83$ ).

Figure 4-10 summarises the measured and predicted values obtained experimentally and computationally. The predicted values result from the processing conditions of simulation#1. The presented graph shows the deviation between the measured values and the predicted ones; 82% of the outspread regions show a deviation less than 10% and just one region show deviation higher than 10% (sample 10). In our opinion this is related to the presence of weld lines resulting from three different melt fronts which may indicate a structural weakness.

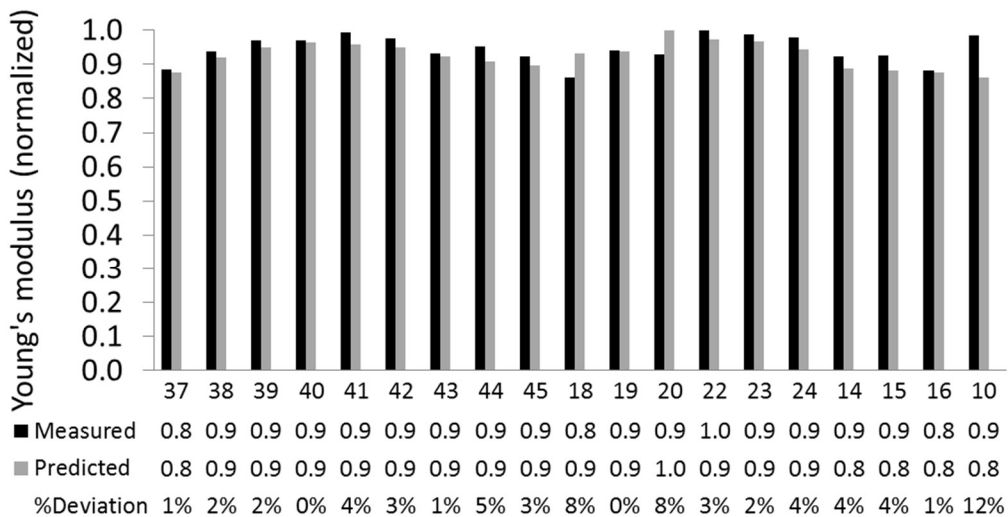


Figure 4-10. Measured and computed Young's modulus results for the envisaged AOI.

The accuracy of predictions of mechanical properties through the TME assessment is highly dependent on the quality of the model mesh as well as the accuracy of the moulding process settings (e.g. material selection, processing conditions, gate locations and geometry, runners, mould and machine characteristics). The door panel has been mesh-modelled according to the best practices and the gate locations correctly defined. The feed system was not modelled in this study due to the absence of such project info. The moulding conditions that were used at the shop floor level to produce such a part were not disclosed.

#### 4.7 Conclusion remarks and future work

The main goal of TMI values estimation is lined to the necessity of accurate mechanical properties prediction at a design phase. Aside from the academic interest, this challenge meets the needs of engineers involved on a daily basis with the design of plastic parts.

From the proposed methodology, the predicted properties from TMI is made available in the form of an output file (in a specific defined format), or in an analytical user interface that shows estimated values. Despite the unavailability of some information of the project (e.g. gates and runners) and process (e.g. moulding conditions and machine characteristics) that could lead to more accurate results, the response of the developed computer application and TMI methodology was satisfactory.

This approach will be made available, in a near future, with a mapping interface that allows the distribution of the local properties throughout the entire domain of a finite-element model, leading to more accurate

simulations results. Moreover, a methodology to integrate/combine the approach presented in this paper with structural mechanical simulations has been defined and is being developed.

## References

1. Shoemaker, J. (Ed.) *Moldflow Design Guide: A Resource for Plastics Engineers*, Hanser Gardner Publisher, Portland (2006).
2. Kennedy, P.K. *Practical and Scientific Aspects of Injection Molding Simulation*, PhD Thesis, Technische Universiteit Eindhoven, Eindhoven, The Netherlands (2008).
3. Daiyan, H., Andreassen, E., Grytten, F., Lyngstad, O.V., Luksepp, T. and Osnes, H. *Polymer Testing*, 29, 894 (2010).
4. Mendoza, R., Régnier, G., Seiler, W. and Lebrun, J.L. *Polymer*, 44, 3363 (2003).
5. Viana, J.C., Cunha, A.M. and Billon, N. *Polymer*, 43, 4185 (2002).
6. Housmans, J.W., Gahleitner, M., Peters, G.W. and Meijer, H.E. *Polymer*, 50, 2304 (2009).
7. Barbosa, C.N., Viana, J.C., Franzen, M. and Simoes, R. *Polymer Engineering and Science*, 52, 1845 (2012).
8. Barbosa, C.N., Simoes, R., Franzen, M. and Viana, J.C. *Journal of Material Science*, 48, 2597 (2013).
9. Viana, J.C., Billon, N. and Cunha, A.M. *Polymer Engineering and Science*, 44, 1522 (2004).
10. Michaeli, W., Hopmann, C., Bobzin, K., Arping, T., Baranowski, T., Heesel, B., Laschet, G., Schafer, T. and Oete, M. *International Journal of Materials Research*, 103, 120 (2012).
11. Kagan, V.A., Mazza, J. and Roth, C. *Society of Automotive Engineers World Congress*, Detroit, Michigan, 110, 500 (2001).
12. Neves, N.M., Pontes, A.J., and Pouzada, A.S. *Journal of Reinforced Plastics and Composites*, 20, 452 (2001).
13. Miled, H., Silva, L., Coupez, T. and Agassant, J.F. *International Polymer Processing*, 27, 547 (2012).
14. Zienkiewicz, O.C. and Taylor, R.L. (Eds.) *The Finite Element Method: The Basis*, Butterworth-Heinemann Publisher, Oxford (2000).
15. Autodesk Inc. *Autodesk Moldflow Insight*, Autodesk Moldflow Help Manager (2012).



## 5. INTEGRATIVE SIMULATION CHAIN FOR DESIGNING AUTOMOTIVE INJECTION MOULDED THERMOPLASTIC COMPONENTS: LINKING PROCESS AND STRUCTURAL SIMULATIONS

This chapter is based on the scientific paper submitted Materials & Design (2018).

### Abstract

Computer Aided Engineering (CAE) is common standard in the development process within the automotive industry. For thermoplastic components, for example, the manufacturing process is commonly simulated with injection molding simulation software and passive safety with explicit crash software. Currently both disciplines are only linked within the simulation of fiber reinforced thermoplastics to take into account the fiber orientation from injection molding simulation within crash simulation due to the significant influence of the fiber orientation on mechanical part properties. This work proposes a methodology that allows consideration of molding conditions on the mechanical behavior of unreinforced injection molded components by coupling injection molding simulation (Moldflow) and crash simulation (LS-DYNA®/RADIOSS®). A newly developed dedicated computer application allows to directly consider results from injection simulation within crash simulations. The manufacturing boundary conditions that most influence the mechanical behavior are combined within the thermomechanical indices (TMI) methodology, and mapped onto each finite element within the crash simulation. Mathematical functions have been used to correlate the TMI to important mechanical properties of the molded polymer. A user defined material model can read those indices and translate them to local mechanical properties.

Different combinations of molding conditions were selected to manufacture components that were subjected to impact tests. The mechanical response of the polymeric parts under crash was analyzed by simulations and validated by experimental testing. A set of quasi-static (1 mm/s) and dynamic impact (3 m/s) tests were performed, the force-displacement curves being experimentally and numerically assessed. The simulations under quasi-static loads overestimate the attained peak force, but the overall material response (elastic and hardening) is representative of the expected trend. In the case of dynamic

loads, the crash simulations can predict realistically the overall force-displacement curves in complex molded geometries.

## 5.1 Introduction

Companies orbiting the automotive industry as OEMs (Original Equipment Manufacturers), 1<sup>st</sup> and 2<sup>nd</sup> tiers, raw-material suppliers, etc., are continuously challenged to develop and produce more reliable and lighter-weight components. This is mainly accomplished through product design innovations that encompasses high-performance materials. Over the last few decades, there has been a trend towards the use of advanced technopolymers. These materials have a pivotal impact on the weight reduction as well as on innovative design features of automotive components. Indeed, plastic materials are distinguished by the amazing physical adaptability and impressive breadth of technical/aesthetical performance, allowing product designers to create extraordinarily complex and highly fluid forms [1].

The development process of plastic automotive components is highly supported by sophisticated CAD (Computer-Aided Design) and CAE (Computer-Aided Engineering) software. These have extended the formal and functional possibilities of the engineering design and manufacturing processes. For instance, mold filling and crashworthiness simulations are fundamental computer-aided applications in the development of lighter and more reliable automotive injection molded components. Nevertheless, there is a room for improvements. Besides the increasing need for super computation power, computer-aided tools integration [2-4] and the complex modelling of thermoplastics' mechanical behavior [5-7] are of crucial importance for better-quality simulation results.

Commonly, structure analyses of injection-molded plastics parts are based on materials' isotropic characteristics. As known, their mechanical properties are extremely dependent on the process induced microstructures (e.g. molecular orientation and degree of crystallinity) resulting from the combination of the injection molding conditions [8-11]. Therefore, this statement has oriented companies and academics to develop improved CAE techniques through the integration of molding and structural simulations. Academics have been working on methodologies for improved prediction of the thermomechanical properties of injection molded fiber-reinforced thermoplastics through the integration of fiber orientation and mechanical properties computation [12-17].

Car manufacturers are improving their intelligent plastic engineering design principles based on the intensifying use of such virtual development integrative methodologies. For instance, an applied research

work has presented a method for transferring injection molding outputs into structural FEA (finite element analysis) for a thermoplastic engine part [18]. The molding-induced anisotropic material properties were readable in structure FEA by using the fiber orientation and mechanical properties of the material. Therefore, a more realistic behavior of the part could be predicted. Nowadays, examples of standalone commercial software such as Converse [19] or Digimat [20] allow the orientation mapping and anisotropic material property data generation through fibers' orientation. Such data exchange interfaces tools are more useful when simulating fiber filled than non-filled materials.

Presently, there is a limited usage of coupling interfaces for unfilled semi-crystalline polymers. An attempted was made to combine injection molding (Moldflow) and structural analysis (Abaqus) in order to improve the mechanical response prediction for unreinforced polymers [21]. The combined effect of crystalline growth and molecular orientation were considered the key features to couple both disciplines. A multilayered FEM (finite element model) was built and those microstructural features assigned for each through-thickness material layer. The authors reported a good agreement between the numerical and experimental results.

Besides the complex coupling process issues, a good description of the component's material behavior in a wide range of loading conditions is determinant to achieve satisfactory simulation results. In the existing numerical tools for structural simulations (e.g. commercial crash software packages) the mechanical properties are described by numerical constitutive material numerical models. A comparative review of material models for polymers (elastomers, foams and thermoplastics) with special focus on crashworthiness analysis is presented by Bois et al. [7]. An overview on existing material models for thermoplastics applicable on shell mesh elements in LS-Dyna is given by Huberth et al. [22]. Arriaga and co-authors [23] evaluated the validity of elasto-plastic strain rate sensitive constitutive models implemented in both Ansys and LS-Dyna commercial codes. Other relevant works have been improving the state-of-the-art on the constitutive material modelling for amorphous [24] and semi-crystalline [25-28] polymers.

Accurate modelling of thermoplastics structural behavior is still a challenge due to several factors, enumerated elsewhere [6]. The complex material – yield or elasto-plastic and fracture – behavior of thermoplastic materials has hitherto been described with limited accuracy, leading to obvious deviations between the physical and the simulated material behavior. For this reason, Ford Research and Innovation Center Aachen, Germany, has chosen an advanced material model developed by MATFEM [29] to enhance the crash simulation of thermoplastic materials. This material model, MF-GenYld+CrachFEM, which accounts for the major yield, hardening and failure issues of thermoplastics, is already validated

for automotive applications [30-33]. Despite the good results achieved so far, there is a significant potential for improvement in crash simulations (e.g. efficient CAE tools integration).

This work proposes an approach so that data from injection molding process simulation can be interpreted correctly by the commercial crash code LS-Dyna through the material model MF-GenYld+CrachFEM. The main objective is to evaluate the influence of the injection molding conditions on the material properties [stiffness (Young's Modulus), strength (yield stress), stress-strain behavior, fracture] at CAE level. This combines experimental and computational efforts to improve design and processing of thermoplastic components for impact load cases by predicting the mechanical properties through CAE tools integration. Practical experiences shows the benefits of the integrative simulation process.

## 5.2 Materials and moldings production

This study exposes the results of impact tests performed on plastic boxes with different processing induced morphologies. Next sections report the relevant data for the material and its processing.

### 5.2.1 Thermoplastic material

A commercial isotactic polypropylene (iPP), coded as PP81, typically used in automotive interior parts, was used on this investigation. Table 5-1 summarizes the material's main characteristics. Due to confidentiality agreement terms, the specific PP grade cannot be released.

Table 5-1. Technical data of the PP81 (Moldflow database).

Mel flow index (g/10 min)	10
Melt density (g/cm <sup>3</sup> )	0.735
Solid density (g/cm <sup>3</sup> )	0.911
Viscosity ( $\dot{\gamma} = 10^4 \text{ s}^{-1}$ and $T = 240 \text{ }^\circ\text{C}$ ) (Pa.s)	14.7

### 5.2.2 Moldings production

The geometry and basic dimensions of the plastic boxes are shown in Figure 5-1. The moldings were produced using a valve-gated hot runner system. The plastic box has two injection locations, four auxiliary pressure points, two front needles and a central pin.



The ideal preliminary molding settings were determined, according to the material technical datasheet and processing recommendations, by conducting a molding window analysis available in the Autodesk Moldflow Insight (AMI) 2012 software. This preliminary analysis comprises a set of specifications which are fully reported elsewhere [34].

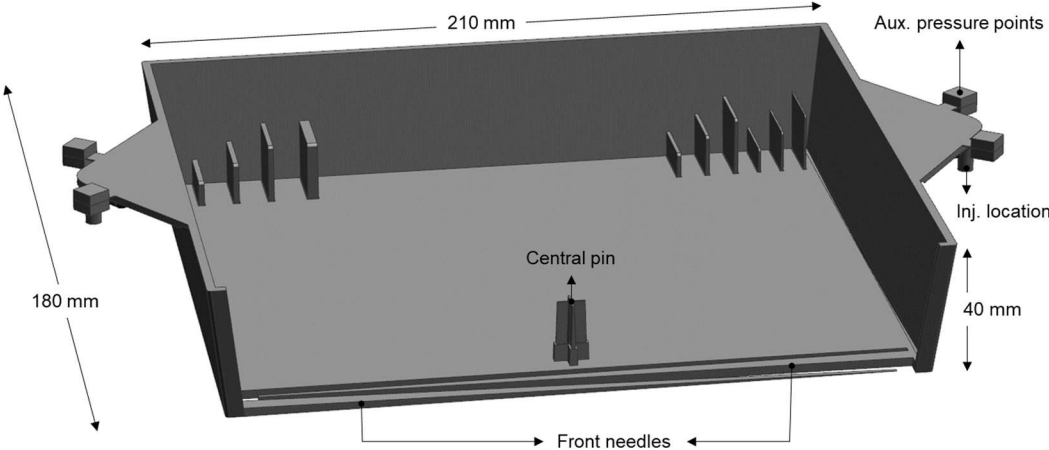


Figure 5-1. Geometry of the injection molded plastic box case study part.

Table 5-2. Boundary injection times as a function of the processing temperatures.

Parameters	Mold wall temperature ( $T_w$ )   Melt injection temperature ( $T_i$ )	
	70   210 (°C)	10   280 (°C)
$t_i^{min}$	1.19	0.47
$t_i^{max}$	3.52	1.47
$t_i$ (s)	1.33	1.33
$P_h$ (MPa)	18	11
$t_h$ (s)	15	15
$t_c$ (s)	30	22

Table 5-2 summarizes the processing/simulation design. Basically, the range of mold wall and melt injection temperatures,  $T_w$  and  $T_i$ , was defined according to the recommended processing conditions provided in the Moldflow database. The injection time ( $t_i$ ) was determined as a function of these processing temperatures. The higher the thermal amplitudes ( $T_i - T_w = max$ ) the more restricted is the injection time window, i.e. the difference between  $t_i^{max}$  (low flow rate) and  $t_i^{min}$  (high flow rate) is smaller ( $t_i^{max} - t_i^{min} = min$ ).

The switch-over pressure, i.e. the shift from filling to packing, was fixed at 99% of the volume filled. For each specific simulation, the packing pressure,  $P_h$ , was defined as 80% of the maximum injection pressure. The packing time,  $t_h$ , was determined by sequentially increase the packing pressure time from

5 to 30 seconds in order to identify the time at which the predicted part weight no longer increases, i.e. the gate freezes. The cooling time,  $t_c$ , was defined by combining the frozen layer fraction and maximum bulk temperature analyses. This enabled determining necessary time to obtain parts below the recommended ejection temperature, i.e. fully frozen parts.

The processing temperatures (70|210 and 10|280, shown in Table 5-2) were considered for analysis due to the higher and lower thermal amplitudes ( $T_i - T_w = max$  and  $T_i - T_w = min$ ) induced during processing that may lead to extreme mechanical properties, as reported by other authors in [8-11]. The injection time was defined as the mean value of the corresponding  $t_i^{max}$  and  $t_i^{min}$  from boundary conditions, 70|210 and 10|280, respectively. Therefore, the injection time was defined as 1.33 s for all molding conditions.

### 5.3 Samples preparation and physical testing

In the following paragraphs the laboratorial procedure for the quasi-static and dynamic testing is described. Before fixing the toolboxes in the customized clamping devices, the internal central pin, front needles, the auxiliary pressure points and the small sprue gate were cut off from the moldings, as shown below in Figure 5-2.

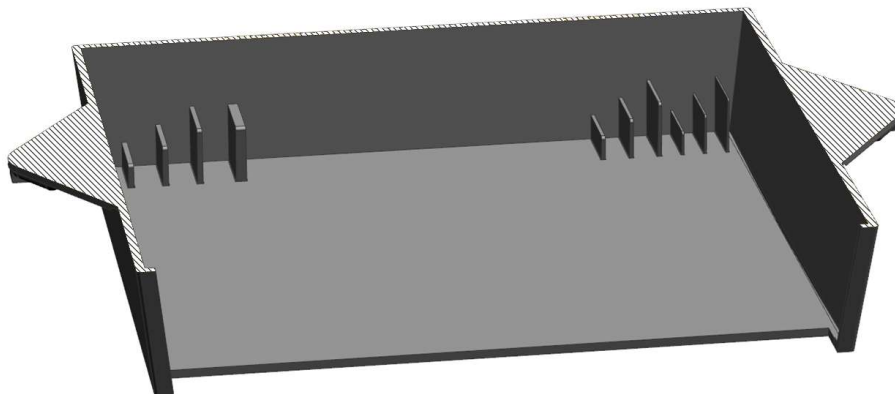


Figure 5-2. Simplified injection molded plastic box for laboratorial testing (dashed lines region represents the glued area; see dynamic tests).

#### 5.3.1 Quasi-static tests

The toolboxes were tested with a load cell of 10 kN, 50 Hz, maximum displacement of 30 mm and impactor velocity of 1 mm/s. The number of tested parts was at least 5 per material/condition, making

a total of 30 trials. The temperatures rounded 29 °C in the lab. The clamping device was built in order to allow the toolbox to be placed centrally under the impactor. A video camera was used to shoot images at 24 frames per second. Figure 5-3 illustrates the most relevant quasi-static tests setup elements.

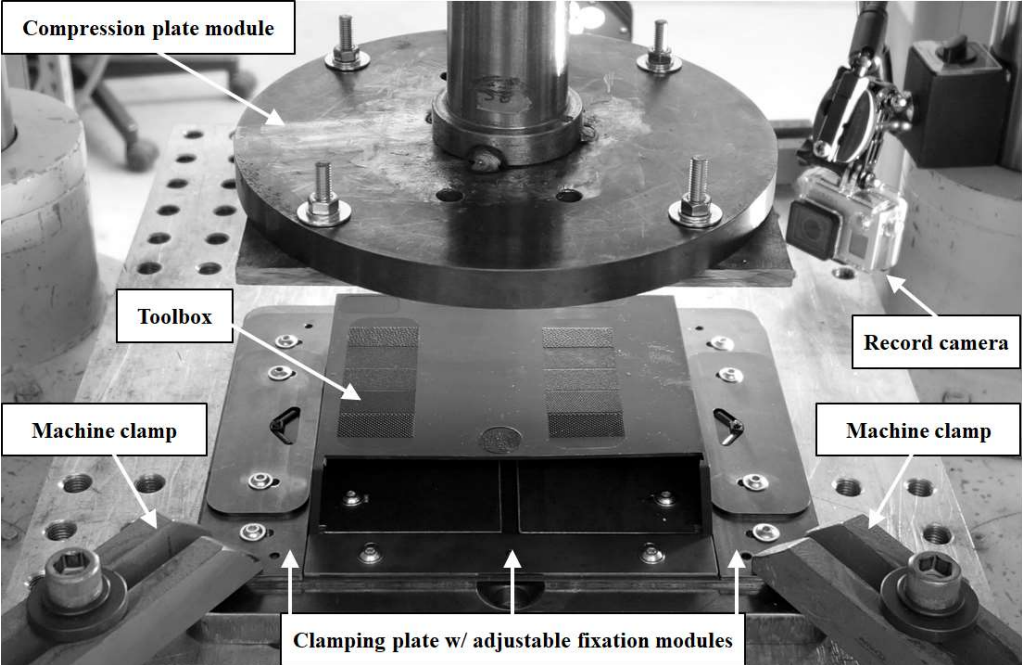


Figure 5-3. Identification of the most relevant setup elements for a quasi-static compression test.

### 5.3.2 Dynamic tests

In addition to the quasi-static tests, the toolboxes were crashed in a drop tower testing machine. An impact mass of 69.5 kg was placed at 0.46 m height from the toolbox, which resulted in an average impact velocity of around 2.96 m/s. The number of tested parts was at least 5 per material/condition, making a total of 30 trials. The temperatures rounded 29 °C in the lab. In this case, the toolbox was completely glued into the fixation plate, i.e. the toolbox and the fixation plate represent together a single body (see Figure 5-2 and and Figure 5-4).

The fixation plate is then screwed against the clamping plate of the drop tower which hosts the load cell system underneath. A video camera was used to shoot images at 4k frames per second. Halogen lamps of 1,000 W were synchronized with the drop tower machine and high-speed camera to record videos in perfect clarity with negligible motion blur. Figure 5-5 depicts the most relevant dynamic tests setup elements.

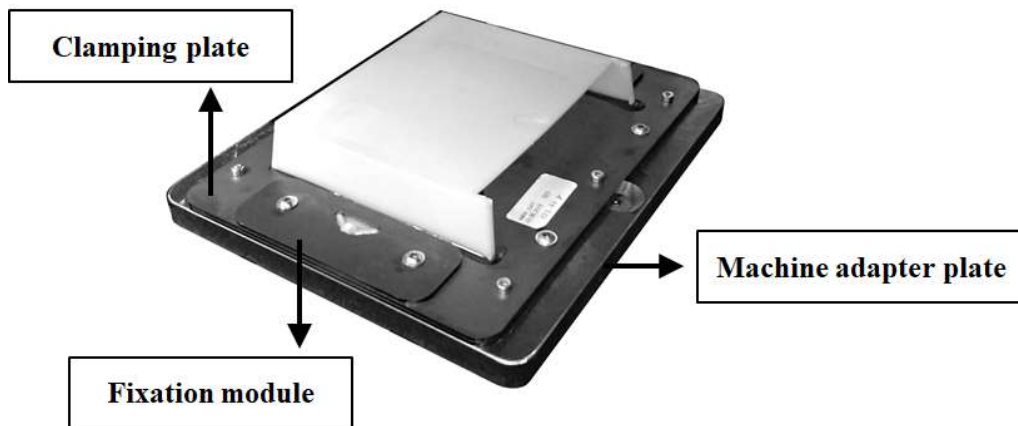


Figure 5-4. Representation of the single body – toolbox glued against the fixation plate (clamping plate and fixation modules).

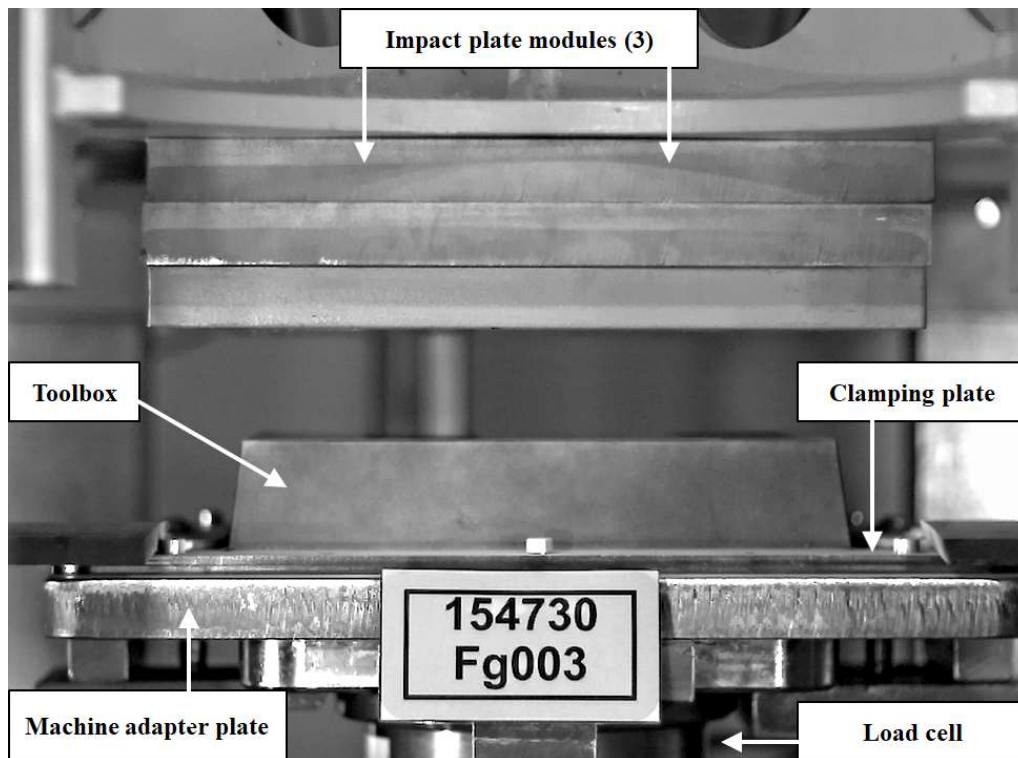


Figure 5-5. Identification of the most relevant setup elements for a dynamic (drop tower) test.

## 5.4 Simulation techniques and mapping tools

### 5.4.1 Moldflow simulations

The injection molding process of the plastic boxes was replicated through the Autodesk Moldflow Insight (AMI) 2012 software. The program is able to report valuable results that are generally used to improve plastic part designs, injection mold designs and the manufacturing process.

The CAD model was discretized into a mid-plane finite element mesh type according to best practices [35]. The part has an average wall thickness of around 2.5 mm, thin ribs of 0.5 mm and injection gate regions 4 mm thick. The accuracy and reliability of injection molding simulation has an important effect on the structural simulation performed afterwards. Factors affecting AMI accuracy may include: solver technology; component modeling (mesh type and density of part, gate and feed system); material data; machine characteristics and process conditions.

The AMI midplane model used in this project has several simplifications. A 2.5D or 3D mesh type would lead to a more accurate results. However, the computation time would exponentially increase and the link to the structural simulations would be unfeasible.

#### **5.4.2 Structural FEA and material model**

The purpose of the crash analysis is to observe how the plastic boxes behave under quasi-static and dynamic impact loadings. The LS-Dyna crash code is used for the analysis. Figure 5-6 represents the mesh file used in the LS-DYNA simulations. Prior to any simulation it was necessary to perform a set of tasks and analysis, including:

- Creating the mid-mesh based on CAD data;
- Detailed consideration of local thicknesses (CAD2FE tool);
- Modeling the fixations for quasi-static and dynamic tests. In case of dynamic tests the fixation plate and the toolbox were glued and considered as one single body (connected with rigid bodies);
- Modeling the impactors for both tests: quasi-static and dynamic tests (rigid wall);
- Creating the load case scenarios [boundary conditions for fixation and impactor (degree of freedom, DOFs), contact modelling between all parts, test velocities] for both quasi-static and dynamic tests.

After the establishment of the previous tasks, a set of investigations were performed in order to understand the effect of the considered variables (friction, initial velocity, relative contact between impactor plate and toolbox, and geometric issues) on the force-displacement curve of dynamic tests. Regarding the quasi-static simulations, an investigation on the nodes position of the side wall of the toolbox was carried out to study the side-wall buckling effect. These investigations were performed in order to achieve the best correlation between simulation and physical tests.

In order to truthfully predict the mechanical performance of a component via simulations, FEA codes requires detailed information about the geometry, loads, boundary conditions, and of course the material. The material model must describe precisely the complete stress-strain behavior curve of the polymer (elastic, plastic and fracture characteristics).

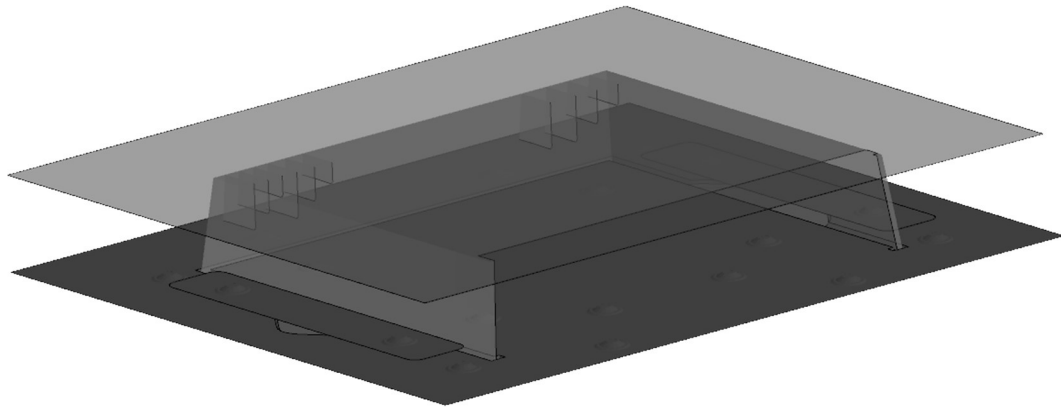


Figure 5-6. Finite element model used in the LS-Dyna simulations (semi-transparent top plate represents the compression/impact plate).

Most models are currently based on data from the tensile materials tests. The ISO 18872:2007 specifies procedures for determining the tensile properties of molding plastics over a wide range of strain rates also appropriate to impact-loading situations [36]. Properties are determined through the use of mathematical functions to model the experimental results, considering rate-dependence of parameters; tensile properties at very high strain rates are then derived by calculation. The MF-GenYld+CrachFEM selected for this work is a user-defined material model developed by MATFEM [30-33].

#### 5.4.3 Computer applications for properties prediction and mapping

The AMI results have been combined in two semi-empirical mathematical equations (thermomechanical indices, TMI) to characterize the thermomechanical environment imposed by molding conditions. The most important process induced changes are based on the level of molecular orientation (thermo-stress index, TSI) and the degree of crystallinity (cooling index, CI) of the molded samples [8, 9, 11].

The computation of the TMI has been performed with a computer application, denominated TMI-App, specifically developed for this project. The TMI-App was developed in native C language to parse AMI simulation outputs and store them in an embedded database. A frontend application has also been developed in C#, allowing faster results analysis and TMI calculation for every single molding mesh element. Each mesh element contains the specific TMI info. A previous study has shown the development process of the TMI methodology and ensuing application, demonstrating the usefulness of this tool [9, 34].

A specific thickness is exported from the TMI-App to FEA packages (e.g. LS-Dyna) through MAPIT application. MAPIT is a Ford Motor Company in-house developed software, presented elsewhere [37]. In

the scope of the present work, its function is to map the element properties from mold-filling-specified mesh to structure-specified mesh. The mapping tool matches the elements' geometric data and maps relevant information, even though the mesh characteristics are totally different, i.e. while the rheological mesh is given by triangle elements the structural mesh is represented by square elements. Consequently, every single structural mesh element contains the specific TMI info that decodes the process induced changes.

Figure 5-7 and Figure 5-8 show the element properties (nodes ID and coordinates, as well as elements ID and TMI info) mapping between mold-filling and structural meshes of a simple geometry for data exchange validation process. It must be noticed that, the best results can be obtained, if the geometrical difference between both meshes (rheological and structural) are small; large deviations in the mesh size discretization can lead to significant errors [16, 33].

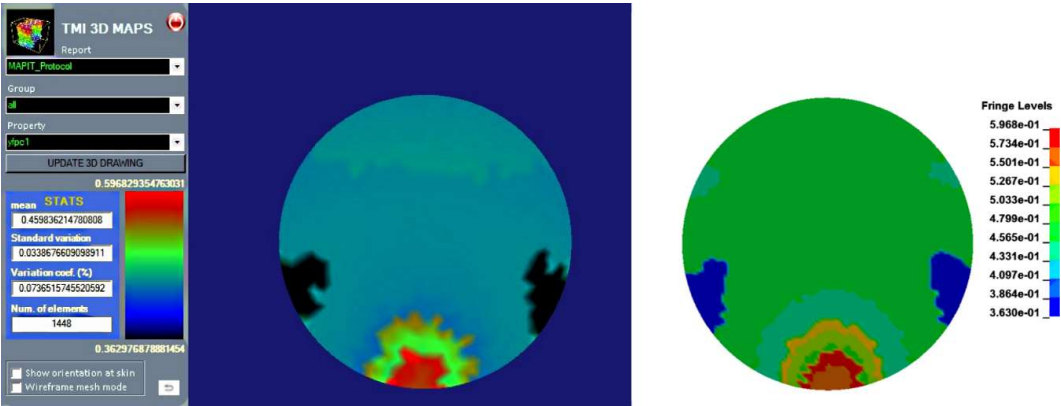


Figure 5-7. Cooling index as mapped by TMI-App (left image as per rheological mesh) and by MAPIT (right image as per structural mesh) for a simple disc geometry.

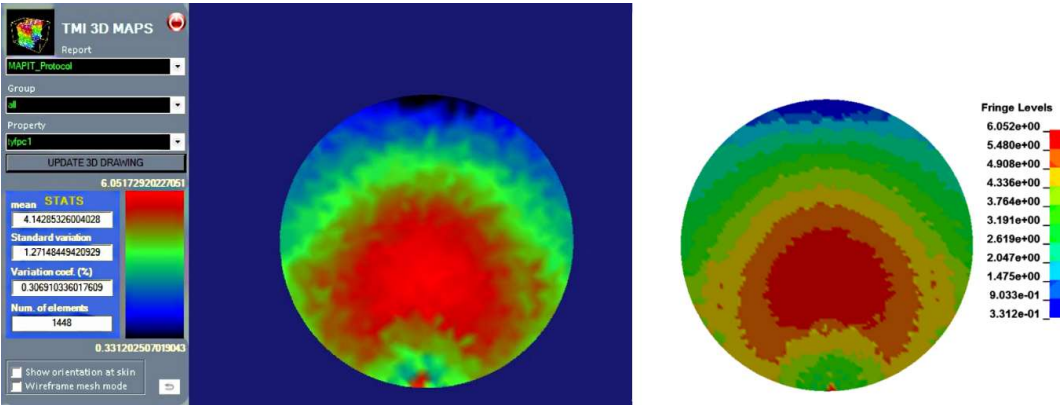


Figure 5-8. Thermo-stress index as mapped by TMI-App (left image as per rheological mesh) and by MAPIT (right image as per structural mesh).

## 5.5 Integrative simulation approach

An integrative simulation chain has been established for assessing the deformation and failure behavior of unreinforced injection molded thermoplastics parts under mechanical load. For this purpose, dedicated (TMI and MAPIT) and commercial (AMI and LS-Dyna in combination with a user defined material model MF-GenYld+CrachFEM) computer applications have been applied. The data exchange procedure is shown in Figure 5-9.

The relevant AMI outputs are transferred to the TMI-App. This application generates a specific format mesh report file `mapit.prot.txt` which is synchronized with the MAPIT-App. Beforehand the FE mesh model file `fe-model.k` is uploaded to the MAPIT-App. This application maps moldflow computed data onto crash mesh and generates the initial stress shell file `inc_tmi-info.k.map` that is required to run structural simulations. The crash finite element mesh contains, therefore, the thermomechanical environment imposed by the molding conditions.

Besides, the TMI-App computes the CI and TSI for each processing simulation mesh element, and generates the `tmi.txt` report file. Three dimensional correlations between the computed TMI and properties measured experimentally (e.g. Young modulus, yield stress, fracture strain, etc.) can be determined through statistical design of experiment tools. The TMI methodology, here applied, basically finds straightforward mathematical relationships to model/predict the mechanical behavior of molded parts by considering the process induced thermomechanical environment. However, the basis to achieve reasonable predictive models is by performing a comprehensive characterization of the materials under different temperatures, strain rates and manufacturing conditions. The thermomechanical properties of the materials presented in this work were obtained through dynamic mechanical analyses and high-velocity tensile tests.

The mathematical model equations are then normalized, scaled and implemented in the user-defined-code file `mfuser-tmi*.c` and in the material card file. The normalization and scaling factors adjustment of the predictive models are executed by considering the reference material properties of a specific user-defined material card. The material card MF-GenYld + CrachFEM, already introduced, was used in this investigation. The reference material properties are achieved through a systematic procedure that combines laboratorial testing (e.g. mechanical characterization of injection molded samples) and mathematical fitting approach (e.g. force-displacement curves). The geometric features of the test samples as well as the boundary injection molding conditions used for production must be used as AMI simulation inputs. As a result, the gap between material properties captured in the lab environment and those experienced in actual molding conditions is empirically reduced.



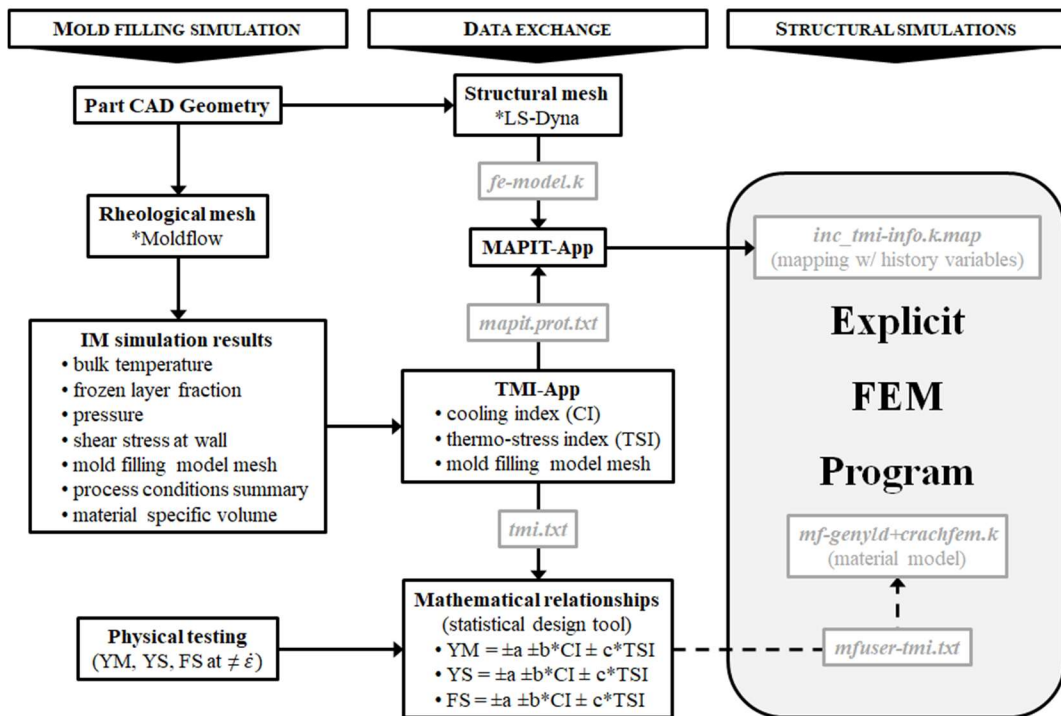


Figure 5-9. Integrative user-defined simulation chain to link the processing induce material changes with commercial explicit finite element codes.

The boundary injection molding conditions of the studied thermoplastic induces a specific thermomechanical environment – characterized by the TMI – that leads to the reference material properties. These are the reference TMI . For improved understanding, the output of a structural simulation for a reference material grade without TMI data would result in an equivalent force-displacement response if the material card contains the reference TMI values. Any other combination of TMI leads to different mechanical response and the properties are scaled accordingly.

Finally, MF-GenYld+CrachFEM provides a shared object interface enabling the modification of the user defined material model. Within Linux, the makefile writes out the final shared object file mfuser-tmi.so and the crash simulation outputs are computed, reflecting the effects of the molding conditions. The above described integrative user-defined simulation chain contributes to improved virtual product/process development.

## 5.6 Results and discussion

In order to validate the new developed functionality, i.e. include the injection molding simulation results in the crash simulation material card through TMIs, a basic component (tensile sample) simulation was

firstly carried out. With this approach, the capability of the developed simulation chain can be tested with reduced computation time. Moreover, functional issues can be easier identified than with complex simulation models. Secondly, experimental test results are compared to the simulated deformation behavior of the toolboxes, following the same simulation chain approach. The analysis results have been proved valuable.

### 5.6.1 Integrative methodology validation through simpler simulations

Simulations were performed in a tensile sample model using different inputs. The boundary conditions and results are shown in Figure 5-10. At first, the simulation was run without any injection molding history assigned to the material card (black curve) of the tensile sample. Then, another simulation was carried out with the material card containing the reference thermomechanical history (red dashed line) that is equivalent to the first force-displacement curve. Other simulations were performed in order to evaluate the effect of different thermomechanical histories on the hardening response of the material. In this case, minimum (green curve), maximum (blue curve) and random (violet curve) TMI values were used. The random TMI values are the result of thermomechanical history values (within minimum and maximum referenced TMIs) calculated from a specific injection molding condition. As a result of these tensile tests it can be concluded that the method of taking into account the thermomechanical history within crash simulations is correctly working.

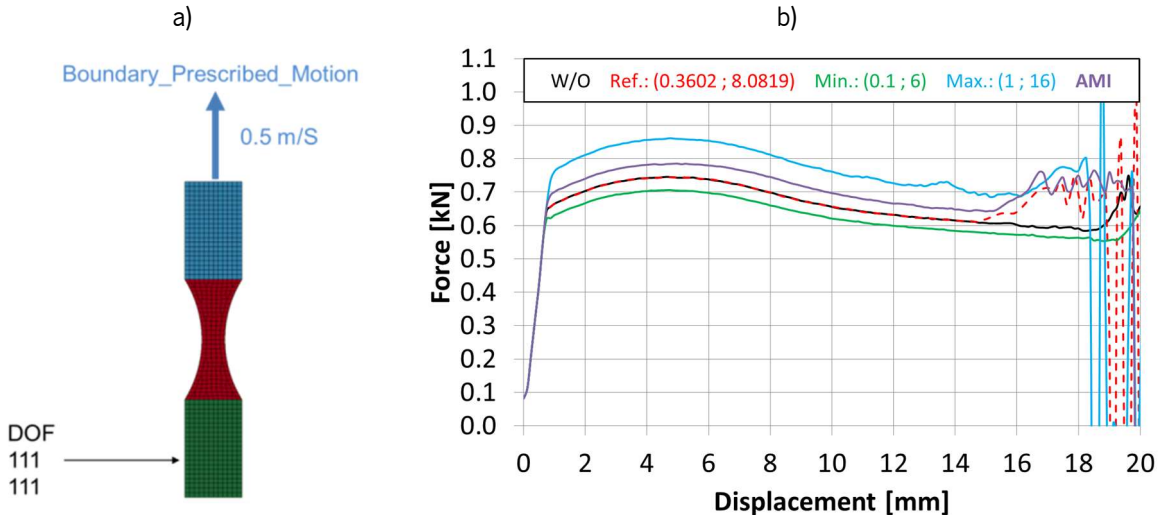


Figure 5-10. a) boundary prescribed motion for tensile simulation; b) comparative results for different inputs.

### 5.6.2 Quasi-static (compression) experiments and simulations

Figure 5-11 shows the representative curves of the quasi-static physical tests as well as the simulation results. Three different molding conditions at shop floor level (Run\_01, Run\_02 and Run\_03) were used to produce the toolboxes. Injection molding simulations were run as close as possible to the shop floor injection molding conditions (AMI\_01.1, AMI\_02 and AMI\_03).

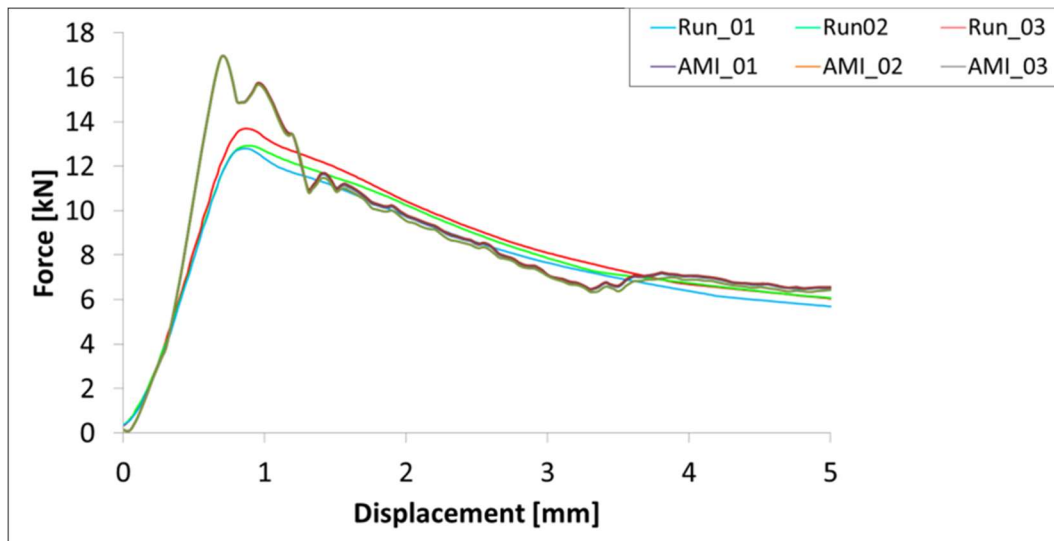


Figure 5-11. Comparative results between simulation and experimental quasi-static tests for the toolbox, as a function of the processing conditions.

Observing the Figure 5-11, it is obvious that there are minor differences between the peak forces within the physical tests results. The thermomechanical environment do not imposed significant changes neither in the simulations nor in the physical test results. In addition, the simulations overestimate the peak force of the material, as represented by the dashed circle. The source of this difference is not yet identified.

### 5.6.3 Dynamic (impact) tests experiments and simulations

Figure 5-12 shows the representative curves of the dynamic physical tests as well as the related simulation results. Three different injection molding conditions (Run\_01, Run\_02 and Run\_03) were used, at shop floor level, to produce the toolboxes. Injection molding simulations (AMI\_01, AMI\_02 and AMI\_03) were performed as close as possible to the real manufacturing settings.

Observing the Figure 5-12, the simulation results (AMI\_01-02-03) are all similar evidencing a neglected effect of the thermomechanical environment imposed by the simulation inputs. However, the tests of Run\_01-03 are well described (initial slope and peak force) by the simulations of AMI\_01-03. On the

other hand, it was expected to see a different simulation curve response for the AMI\_02, following somehow the real curve. This is not observed which reveals that the TMI approach is not describing completely the material behavior as a function of the injection molding conditions for this drop tower test scenario.

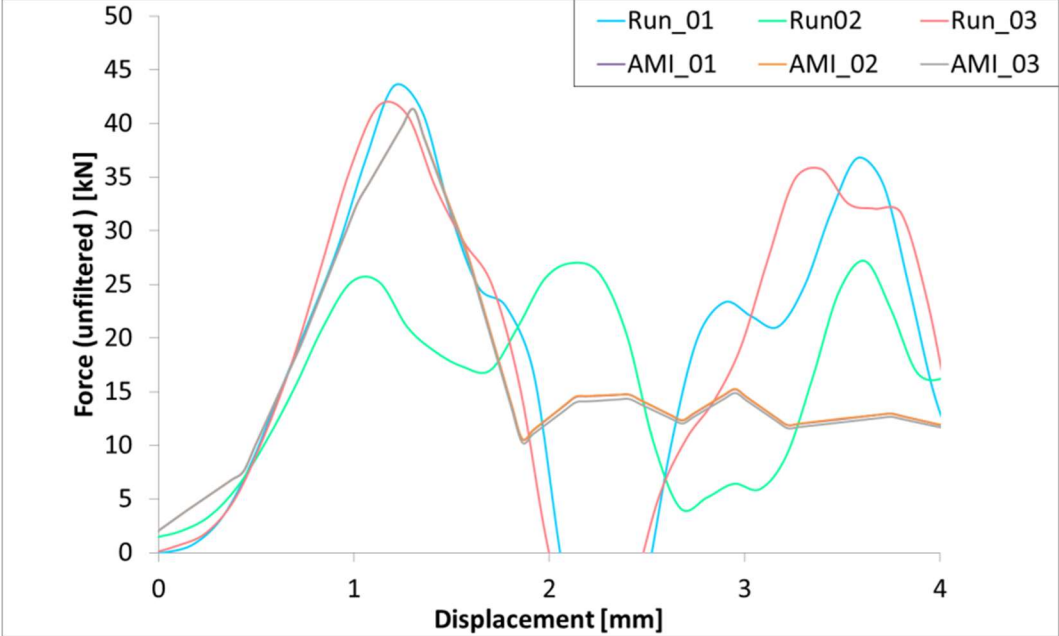


Figure 5-12. Comparative results between simulation and experimental dynamic tests for the toolbox, as a function of the processing conditions.

### 5.7 Conclusions

Injection molding flow simulations and finite element analysis have been applied to simulate the injection molding process and to improve the crashworthiness of thermoplastic parts under specific conditions. In this work, a simulation chain is proposed to link moldflow and structural simulations in order to include the manufacturing process information into the material model.

The accuracy of the proposed methodology is dependent on several factors: from the Moldflow mesh model and the selection of processing settings until the definition of the finite element model and the physical boundary conditions. The establishment of improved relationships between the developed microstructure (characterized by the TMI) and the mechanical response is essential to allow better predictions. The quality of the mathematical fitting (given by the coefficient of multiple correlation) of the

TMI *vs.* mechanical properties must be statistically improved for more accurate predictions. This may be accomplished by redefining the TMI equations.

TMI are dependent on the injection molding conditions used in simulation and the mechanical properties are measured in real injection molded test components. There is always an error associated to the mechanical properties measurements and it must be highlight that differences always exist between molding simulations and real production. The combination of these issues influences the accuracy of our predictions.

The simulation chain was successfully implemented. The scale factors were defined for the hardening (HRD) and elastic region (YM). Another approach may be followed to encompass a more complex strain-rate dependency of the materials on the mechanical response. This may improve the accuracy of the predictions. Other kind of tests, simpler tests (e.g. tensile on cut specimens from complex parts) should be performed in order to test the overall feasibility of this integrated methodology.

## References

1. C. Fiell and P. Fiell. *Plastic Dreams: Synthetic Visions in Design*, Fiell Publishing Limited (2009).
2. B. Louhichi, G.N. Abenhaim, and A.S. Tahan. *Int. J. Adv. Manuf. Technol.*, 76, 391 (2015).
3. V. Ferreira, L. P. Santos, M. Franzen, O.O. Ghouati, and R. Simoes. *Advances in Engineering Software*, 71, 52 (2014).
4. H-S. Park and X-P. Dang. *Computer-Aided Design*, 42, 889 (2010).
5. G. Gu, Y. Xia, C-H. Lin, S. Lin, Y. Meng, and Q. Zhou. *Materials & Design*, 44, 199 (2013).
6. J.C. Viana, A.M. Cunha, and N. Billon. *Polymer Engineering & Science*, 47, 337 (2007).
7. P.A. DuBois, S. Kolling, and M. Koesters, T. Frank. *International Journal of Impact Engineering*, 32, 725 (2006).
8. C.N. Barbosa, R. Simoes, M. Franzen, T. Baranowski, and J.C. Viana. *Polymer Engineering & Science* DOI: 10.1002/pen.24650 (2017).
9. C.N. Barbosa, F. Carvalho, J.C. Viana, M. Franzen, and R. Simoes. *International Journal of Advanced Manufacturing Technology*, 77, 873 (2015).
10. J-W. Housmans, M. Gahleitner, G.W.M. Peters, and H.E.H. Meijer. *Polymer*, 50, 2304 (2009).
11. J.C. Viana. *Mechanical characterization of injection moulded plates*, PhD Thesis, University of Minho (2002).

12. Y. Xu, Q. Zhang, W. Zhang, and P. Zhang. *International Journal of Advanced Manufacturing Technology*, 76, 2199 (2015).
13. H. Miled, L. Silva, T. Coupez, and J.F. Agassant. *International Polymer Processing*, 27, 547 (2012).
14. W. Michaeli, C. Hopmann, K. Bobzin, T. Arping, T. Baranowski, B. Heesel, G. Laschet, T. Schläfer, and M. Oete (2012). *International Journal of Materials Research*, 103, 120 (2012).
15. A. Wüst, T. Hensel, and D. Jansen. ANSA &  $\mu$ ETA International Conference, Halkidiki (2009).
16. A.Y. Peng, E. Wu, and C.T. Huang. LS-Dyna European Users Conference, Strasbourg (2011).
17. C. Kröner, H. Altenbach, and K. Naumenko. *Mechanics of Composite Materials*, 45, 249 (2009).
18. T. Schmidt. SIMULIA Community Conference, Vienna (2013).
19. [www.partengineering.com/software/converse](http://www.partengineering.com/software/converse) (01-10-2017, 12h45)
20. [www.e-xstream.com/products/digimat/about-digimat](http://www.e-xstream.com/products/digimat/about-digimat) (01-10-2017, 12h46)
21. E. Andreasson, L. Persson, H. Jacobsson, and J. Nordgren. SIMULIA Community Conference, Vienna (2013).
22. F. Huberth, S. Hiermaier, and M. Neumann. LS-Dyna Anwenderforum, Bamberg (2005).
23. A. Arriaga, R. Pagaldai, A.M. Zaldua, A. Chrysostomou, and M. O'Brien. *Polymer Testing*, 29, 170 (2010).
24. H. Louche, F. Piette-Coudol, R. Arrieux, and J. Issartel. *International Journal of Impact Engineering*, 36, 847 (2009).
25. F. Detrez, S. Cantournet, and R. Séguela. *Comptes Rendus Mécanique* 338, 681 (2010).
26. A.F. Epee, F. Lauro, B. Bennani, and B. Bourel. *International Journal of Solids and Structures*, 48, 1590 (2009).
27. D.A. Şerban, L. Marşavina, and V.V. Silberschmidt. *Computational Materials Science*, 64, 116 (2012).
28. A. Maurel-Pantel, E. Baquet, J. Bikard, J-L. Bouvard, and Noëlle Billon. *International Journal of Plasticity*, 67, 102 (2015).
29. [www.matfem.de/en](http://www.matfem.de/en) (01-10-2017, 13h20)
30. G. Oberhofer, M. Franzen, and H. Dell. *Kunststoffe+Simulation*, Fellbach/Stuttgart (2007).
31. M. Franzen and H. Lanzerath. *ATZautotechnology*, 8, 40 (2008).
32. G. Oberhofer, A. Bach, M. Franzen, H. Lanzerath. European LS-Dyna Conference (2009).
33. H. Gese, G. Oberhofer, and H. Dell. LS-Dyna Anwenderforum, Frankenthal (2007).
34. C.N. Barbosa, F. Carvalho, J.C. Viana, M. Franzen, T. Baranowski, and R. Simoes. *International Journal of Materials and Product Technology*, 52, 76 (2016).

35. J. Shoemaker. Moldflow Design Guide: A Resource for Plastics Engineers, Hanser Gardner Pub. (2006).
36. [www.iso.org/standard/38914.html](http://www.iso.org/standard/38914.html) (28-09-2017 22h10)
37. A. Hänschke. The CAE Driven Safety Development Process of the New Ford Fiesta. European Hyperworks Technology Conference, (2009).





## 6. COST MODELING FOR EARLY STAGE DESIGN DECISIONS: A MOLDFLOW-BASED TECHNICAL COST ESTIMATION FOR INJECTION MOLDED THERMOPLASTIC PARTS

This chapter is based on the scientific paper published elsewhere:

C.N. Barbosa, R. Simoes, J.C. Viana, M. Franzen, T. Baranowski, and P. Afonso. International Conference on Project Evaluation, ICOPEV, Guimarães (2016).

### **Abstract**

The cost estimation of new injection molded plastic products is often presented as a complex but important task in the early stages of the product development process. This is because only limited information is available and early stage design decisions ought to have a major impact in the final cost of a product. Thus, it is essential to improve the product cost estimation sooner in the product development process to withstand competitive. This work addresses this issue. It describes a methodology for cost estimation of injection molded plastic products that works with data available during the design stage (e.g. geometric features, materials' properties, processing conditions and production requirements). Several scenarios in terms of product design, processing and production may be studied and the cost of the part anticipated. The main results reveal that the cost of a part is basically dependent on the part geometry, and consequently on mold and press, batch number, material and processing conditions.

### **6.1 Introduction**

Accurate manufacturing cost calculation of plastic-made products is an essential engineering task. In product design and development (PDD) process, most of the costs (ca. 70 to 80%) are determined through the conceptual and detail design phases. This emphasizes the importance of cost engineering at the early design stages. The challenge at the conceptual phase is to deal with the unavailability and uncertainty of

crucial information (e.g. detailed geometric features, production requirements, process settings, etc.) that is, in general, only available downstream in the PDD cycle. In industry, cost estimations are usually done in the detail design phase [1]. At the end of this stage, specific design issues (e.g. detailed geometric features) are “frozen” and considerable changes should be thoughtless in order to avoid extra costs.

Design teams, when developing new products consider dozens of quality criteria such as functionality, reliability, robustness, or manufacturability [2]. Within the product design and engineering world, thermoplastic products are commonly used due to their versatility, durability, relatively low cost, among other interesting characteristics. They have been applied to all kinds of daily necessities and hi-tech commodities [3, 4]. Most of these products are widely produced by injection molding (IM) technology. One of the main goals in IM is the improvement of the quality of molded parts at the lowest cost [5]. Therefore, manufacturing costs (related to the criterion of manufacturability) is indeed a key determinant of the economic success of a product [2].

The cost of a product is entirely context dependent and this is a direct consequence of the interrelated nature of product design and manufacturing cost [6]. The total cost may be divided in fixed costs (independent of the production quantity) and variable costs (vary with the quantity produced) [7]. Specifically in IM, the cost of a product is influenced by the number of parts being produced, the material being processed, tooling costs, process cycle time, and the amount of scrap generated [8]. The manufacturing cost of injection-molded parts is considerably defined by the cost of the injection mold which, in turn, is the result of part’s complexity and size as well as by the number of parts being produced in one shot, i.e. number of cavities. These characteristics decide the size of the injection molding machine (or press) to be used for producing the part(s). The specifications of the press are a function of the size of the mold, pressure needed to fill the cavities with the molten polymer and clamping force to keep the polymer within the cavity under pressure. The process cycle time is basically a result of the part’s geometry, type of material and processing conditions. Resuming, the geometric model of the part, the mold, the size of the machine, the processing conditions and the production requirements interact in a complex way to influence the per-part cost.

Computer-aided design and engineering (CAD and CAE) tools have been used by product design engineers to minimize the complexity of their daily work activities. CAD tools are used to generate concept and detailed design parts. On the other hand, CAE tools are applied to evaluate the quality (e.g. structural analysis) and the manufacturability (e.g. processing conditions) of new products under development. These capabilities allow decision makers (e.g. design engineers) to understand the physical – but also – the economic consequences of their technical choices before these are “frozen”.

It is well recognized that manipulating design specifications (dimensionality or other critical design variables) or process operating conditions (melt temperature or cooling time) has consequences not only on product performance, but also on production costs [6]. Modern CAE tools are useful throughout the product development process for evaluating alternative design configurations and to provide continual feedback regarding the functional performance of the design [1]. However, few tools and little quantitative information is provided to aid in cost analysis [9]. The existing injection molding process simulation software (e.g. Autodesk Moldflow Insight, AMI, or Moldex 3D) do not offer analytical tools to estimate the final cost of molding products.

An integrative solution is being developed to address the aforementioned gap and to help product design engineers in their decision making process. This work aims at developing a methodology for cost estimation of injection molded plastic products at early design stage. The methodology results in a preliminary screening tool developed in MS Excel. It functions with important data available from the AMI software such as the volume of the part and feed system, projected area, material properties, and processing conditions. External information must be added to the dedicated tool, including the production volume required, cost of energy, operators' salary, etc. The open architecture of the workbook allows product design engineers to study different scenarios in terms of part geometry, processing conditions and production requirements. This approach facilitates the understanding of the consequences of their decisions and assumptions.

## **6.2 Literature review**

Some detailed cost analysis procedures for injection molded parts have been reported previously. A process-based cost model (PBCM) has been developed at Massachusetts Institute of Technology (MIT) to shed light on techno-economic questions [6, 10, 11]. A PBCM serves as a mathematical transformation, mapping a description of a process and its operating conditions to measures of process performance, i.e. cost. It works backward from cost to technical parameters, which can be manipulated. Fagade and Kazmer (2000) derived cost estimates from a complexity metric defined by the number of dimensions that uniquely define the part geometry [1]. A cost estimating system was developed by the advantages of back-propagation network and through integration of particle swarm optimization and back propagation neural network [3, 4]. Pârv and Urdea (2009) dealt with cost modelling of an injection molding component [8]. A computer based cost model was developed which integrated the relationship between cost factors, product development activities, and product geometry. Jung (2002) presented a feature-based cost

estimating system for machined parts [7]. Niazi et al. (2006) provided a detailed review of the state of the art in product cost estimation covering various techniques and methodologies developed over the years [12]. The authors highlighted the importance of cost estimation in the early phases of the design cycle and briefly discusses the current trends and future directions in this area. Che (2010) proposed a cost estimation approach for plastic injection products and molds that combines factor analysis, particle swarm optimization and artificial neural network [13]. Shing (1999) presented the development of procedures for estimating the manufacturing cost of an injection molded part at the early stage of concept design [14]. The procedures are based on simplified cost models and assume no user knowledge of process parameters or machine selection. Jones (2000) provided a clear understanding of the interrelated processes of budgeting, costing and estimating procedure for the injection molding industry [15].

### 6.3 Cost modeling methodology

This paper adopts a PBCM developed at MIT Materials System Laboratory, which is detailed elsewhere [6]. Basically, a PBCM is composed of three interrelated and interdependent models: a technical process model, a production operations model, and a financial accounting model. This is illustrated in Figure 6-1.

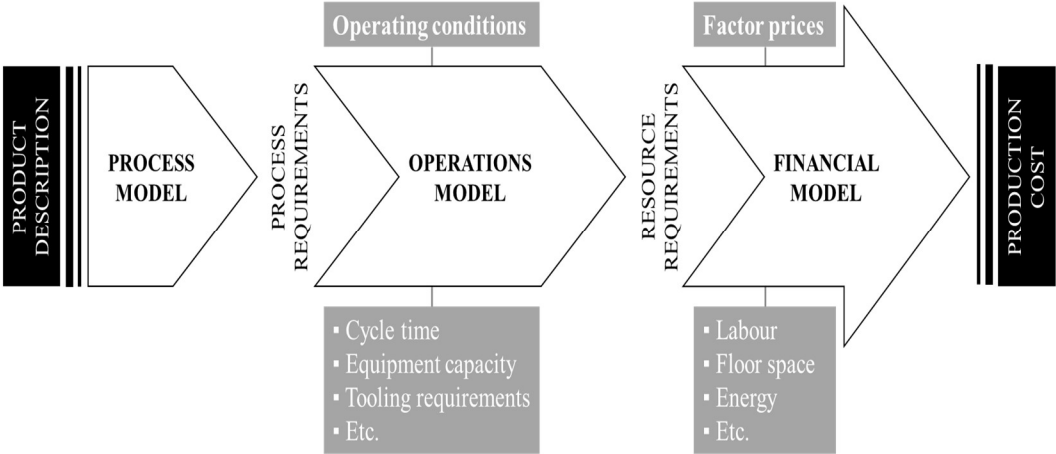


Figure 6-1. Process-based cost modelling framework [10, 11].

Having modeled all the processes and the required resources to produce the part, and introducing the price factors to each cost driver, the economic model is completed and the part cost can be estimated. Cost elements presented in Figure 6-1 can be broken down in two categories: variable and fixed; or into elementary costs: labor, equipment, tooling, material, etc. The cost elements used in this model are shown in Table 6-1.

Table 6-1. Considered manufacturing cost elements.

Fixed costs	Variable costs
Equipment (injection machine)	Material
Mold (tool)	Energy
Overhead labor	Labor
Building	
Working capital	
Maintenance	

The total fabrication cost,  $C_{total}$ , is the sum of all individual contributions, expressed by Equation 6-1.

$$C_{total} = C_{mat} + C_{ene} + C_{lab} + C_{press} + C_{mold} + C_{ohla} + C_{build} + C_{wcap} + C_{maint}$$

Equation 6-1

The recurring (or variable) costs consist of material, energy and labor costs. The one time (or fixed) costs include the machine, tooling, overhead, building, cost of working capital and maintenance costs. This basic approach is kept to streamline the cost model structure organization.

Within the variable cost elements,  $C_{mat}$  stands for the material cost,  $C_{ene}$  expresses the energy cost, and  $C_{lab}$  represents the labor cost. The cost of a material, see Equation 6-2, is a function of the price of the raw material and the annual material consumption. The raw material price (RMP) can be accessed elsewhere [16]. The pricing data is obtained by combining price indexes from suppliers, processors, and consulting groups. Regarding the annual material consumption (AMC), it considers the market demand and the cost of quality (scrap rate and unconformities).

$$C_{mat} = RMP * AMC$$

Equation 6-2

The cost of energy, see Equation 6-3, includes the weight of the molding, the effective production volume (parts per year, EPV), the electric power consumption or electricity requirement (in kWh per kg, ER), the electricity cost (€ per kWh, EC).

$$C_{energy} = weight * EPV * ER * EC$$

Equation 6-3

The cost of labor is presented by Equation 6-4, and it is the result of the number of allocated direct workers (ADW), the annual paid time (in hours, APT) and direct wages (DW). The ADW is the result of the number of direct laborers or workers (NDL) per machine ( $\geq 1$ ) multiplied by the percentage of the line allocated or required (PLA or PLR) depending on the versatility of the line (dedicated or non-dedicated). Nowadays, totally dedicated lines are the exception rather than the rule and the obvious reason behind is the market fragmentation and product proliferation. This implies shorter runs and more variations and versatility to most lines in the typical types of plants making injection molded plastic products [17]. Hereafter it is assumed the line is non-dedicated, thus,  $PLA = PLR$ .

$$C_{lab} = ADW * APT * DW = (NDL * PLR) * APT * DW \quad \text{Equation 6-4}$$

The cost of an injection molding machine, see Equation 6-5, is the result of the payment of loans (credit or investment),  $I_m$ , based on constant payments and a constant interest rate. The number of constant payments can be defined as the accounting life of the machine (in years),  $n_m$ , and the constant interest rate stands for the capital recovery rate (in %),  $i_r$ . The  $I_m$  is proportional to the PLR, the press base cost (PBC) and its installation cost (PIC), as well as the cost of eventual auxiliary equipment (AEC) such as polymer dehumidifier/dryer, hopper feeders, etc.

$$C_{press} = I_m * \left[ \frac{(1+i_r)^{n_m} i_r}{(1+i_r)^{n_m} - 1} \right] = PBC * (1 + \%PIC + \%AEC) * PLR * \left[ \frac{(1+i_r)^{n_m} i_r}{(1+i_r)^{n_m} - 1} \right] \quad \text{Equation 6-5}$$

The proposed cost model assumes that the injection molding machines, or presses, are rated by tonnage or clamping force and hence the press tonnage should be sufficient to determine the PBC. The clamp force is the maximum force required to keep the mold closed during filling and packing phases of the injection molding process. The prediction of the maximum clamp force is a function of the injection pressure distribution over the projected area. Additionally, the injection molding processing pressures are affected by the rheological properties (e.g. viscosity or resistance of a resin to flow) of the material used in the process, i.e. resins with high viscosities (or lower melt rates) require higher injection pressures and thus more clamp tonnage to keep the mold closed. Relying on historical cost data and using simple algebra, a mathematical formula is derived to determine cost against clamping force. The linear relationship between the PBC, and clamping force,  $F_c$ , is presented in Equation 6-6 [18].

$$PBC = 42.86 * Fc + 15890$$

Equation 6-6

The cost of tooling, see Equation 6-7, similarly to the machine cost, is the result of the payment for a loan/credit/investment,  $I_t$ , based on constant payments and a constant interest rate. The number of constant payments can be defined as the accounting life of the tool (in years),  $n_t$ , and the constant interest rate stands for the capital recovery rate (in %),  $i_r$ .

$$C_{mold} = I_t * \left[ \frac{(1+i_r)^{n_t * i_r}}{(1+i_r)^{n_t} - 1} \right] = (MBC + CCC) * \left[ \frac{(1+i_r)^{n_t * i_r}}{(1+i_r)^{n_t} - 1} \right]$$

Equation 6-7

The  $I_t$  is the result of the sum of the cost of the prefabricated mold base (MBC) and the fabrication costs of the cavity and core (CCC). The MBC is a function of the surface area of the selected mold based plates and the combined thickness of the cavity and core plates. The MBC (see Equation 6-8) is essentially dependent on the volume of the mold base. This cost-volume relationship is described elsewhere [19].  $A_c$  stands for the area of the mold base plate and  $h_p$  represents the combined thickness of cavity and core plates in mold base, which derives from measuring the depth of the part.  $A_c$  results from the projected area of the part, or parts depending on the number of cavities, including a minimum clearance of at least 7.5 cm between adjacent cavities as well as between cavities and plates' edges.

Additionally to the MBC, it should be considered other costs associated with tasks to transform the mold base into a working mold (e.g. drilling of the cooling channels, milling of pockets to receive the inserts, preparation of the ejection system, etc.). As a rule of thumb [19], the initial MBC should be doubled to account for those ever-required tasks.

$$MBC = (1000 + 0.45 * A_c * h_p^{0.4}) * 2$$

Equation 6-8

The CCC (see Equation 6-9) is a function of part size and geometric complexity. This entity is generally dictated by the machining hours needed to shape the cavity and core plates. It is obtained by multiplying the total number of hours to manufacture the mold,  $t_0$ , by the toolmaker shop rate, TSR, as empirically expressed in Equation 6-9 [19]. The  $t_{es}$  parameter stands for the required manufacturing hours to produce the ejection system. The  $t_{gf}$  and  $t_{ps}$  variables refer to the required manufacturing hours to produce one cavity and core as a function of the geometrical features/complexity and size of the part,

respectively.  $A_p$  is the total projected area of the part(s). The  $N_{sp}^{in}$  and  $N_{sp}^{ou}$  are the number of surface patches/segments of the inner and outer surfaces, respectively. The higher the number of patches, the higher the complexity of the part.

$$CCC = t_0 * TSR = (t_{es} + t_{gf} + t_{ps}) * TSR =$$

$$= \left\{ \left[ 2.5 * A_p^{0.5} \right] + \left[ 5.83 * (0.1 * (N_{sp}^{in} + N_{sp}^{ou}))^{1.27} \right] + \left[ 5 + 0.085 * A_p^{1.2} \right] \right\} * TSR \quad \text{Equation 6-9}$$

The cost of operational overhead labor, see Equation 6-10, includes those resources not directly involved in manufacturing. It differs from  $C_{lab}$  due to the allocated indirect workers (AIW). This entity is calculated using an indirect/direct laborers ratio. Another approach is to estimate this cost using a burden rate which is applied against the magnitude of the other fixed costs [6].

$$C_{ohlab} = AIW * APT * DW \quad \text{Equation 6-10}$$

Building costs are rather related to the physical space requirements, i.e. the equipment size and conventional practices (e.g. safety specifications, etc.) dictate the building cost. The building cost formula, see Equation 6-11, is the result of the payment for a loan (credit or investment),  $I_b$ , based on constant payments and a constant interest rate. The number of constant payments can be defined as the building recovery life (in years),  $n_b$ , and the constant interest rate stands for the capital recovery rate (in %),  $i_r$ . The  $I_b$  is proportional to the required building space (RBS), the building space cost (BSC), and the PLR.

$$C_{build} = I_b * \left[ \frac{(1+i_r)^{n_b * i_r}}{(1+i_r)^{n_b} - 1} \right] = RBS * BSC * PLR * \left[ \frac{(1+i_r)^{n_b * i_r}}{(1+i_r)^{n_b} - 1} \right] \quad \text{Equation 6-11}$$

The maintenance cost formula is given by Equation 6-12. It is simply a percentage of the sum of the costs of the mold, press and building. The cost of maintenance increases alongside the mold/press/building costs.

$$C_{maint} = \% * (C_{press} + C_{mold} + C_{build}) \quad \text{Equation 6-12}$$



The working capital may be thought as the cash available for day-to-day operations (e.g. buy assets, pay obligations, etc.). In other words, it may represent the cost of assets still in business deal. It is also referred to current capital. It has an interest rate and a period associated. The working capital formula is represented by Equation 6-13. The WCP parameter stands for the working capital period.

$$C_{wcap} = (C_{mat} + C_{ene} + C_{lab}) * \frac{WCP}{12} * i_r \quad \text{Equation 6-13}$$

## 6.4 Case-study presentation

A PBCM was applied to compute the most probable cost of an injection molded part at early product design stages, i.e. before technical drawings are “frozen”. Relevant AMI outputs were integrated into the PBCM in order to improve the accuracy and pace of the cost estimation. Apart of the fundamental information required, the PBCM necessarily contains several explicit assumptions, mainly: electricity and material costs, working days and downtime, toolmaker shop rate, space cost, interest rate or equipment life time. Assumptions can be changed to suit particular circumstances, however, the consequences of changing may vary significantly the final cost of the part.

The relevant PBCM entries from AMI (engineering parameters) are the projected area, the minimum clamping force required for the molding machine, the total weight of the molding (part and feed system, i.e. sprue, runner and gates) and the cycle time. Other important entries are the annual production volume, the scrap rate, the number of cavities (parts per shot), and geometric features of the part such as the number of machined surfaces (cavity and core) as well as the part depth.

The example presented in this work studies the influence of changing geometric details in the final cost of a thermoplastic product, thought under development. The parts shown in Figure 2 present the following basic dimensions: length of 100 mm; width of 60 mm; height of 18 mm; and thickness of 2 mm (main body). The vertical black arrows point out the main differences between the two models. In Figure 6-2a the marked region has a total thickness of 4mm. On the other hand, the 4mm bolt pads were replaced by a number of ribs with 1mm thickness in Figure 6-2b. This geometric modification reduces the amount of material, keeping meanwhile the mechanical resistance of the part.

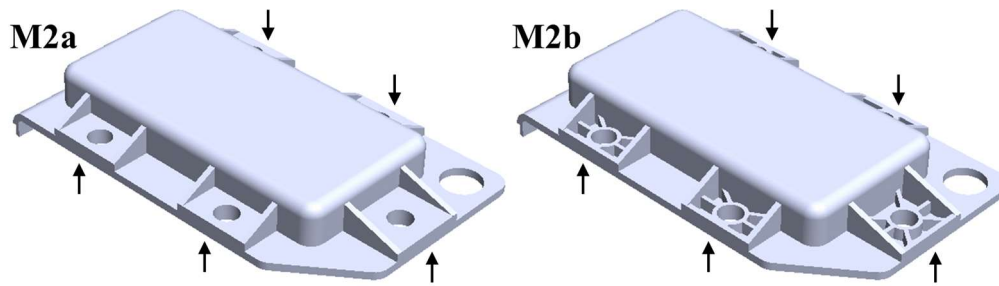


Figure 6-2. CAD models: M2a and M2b (modified).

The injection molding simulations of the two parts were run and analyzed in AMI. The parts are simulated/molded with the same thermoplastic: acrylonitrile-butadiene-styrene (ABS). The molding settings were kept equal for both simulations, as presented in Table 6-2.

The processing temperatures were set according to the recommended conditions of the material supplier. The injection filling time was defined as 1.6 s. The pack/holding control was defined by the packing pressure versus time criterion, i.e. the pressure corresponds to approx. 80% of the injection pressure needed to fill the cavity and the time was determined by the instant at which the gate freezes.

Table 6-2. General injection molding settings.

Process parameters	Value	Units
Mold surface temperature	55	°C
Melt temperature	245	°C
Injection time	1.6	S
Pack/holding pressure	27	MPa
Pack/holding time	7	S
Mold opening/closing time	5	S

The cooling time (not shown in Table 6-2) was defined differently for both simulations due to the modifications in thickness of the bolt pads (observe Figure 6-2). The model M2a needs more time to reach the ideal overall ejection temperature than the model M2b. In this way, the minimum cooling time was 20 s and 3 s for the M2a and M2b, respectively. Resuming, the total cycle time to produce the models are approx. 34 s (M2a) and 17s (M2b).

## 6.5 Results and discussion

Considering the above case description, this section aims at presenting and discussing the results of the per-part cost as a function of i) design features, ii) number of cavities, and iii) annual production volume.

### 6.5.1 Design features

The total manufacturing cost is the sum of the elementary costs. Figure 6-3 compares the elementary costs as well as the total manufacturing costs of both models presented above. In this case, the annual production volume was kept constant (200k parts per year) as well as the number of cavities (1 cavity).

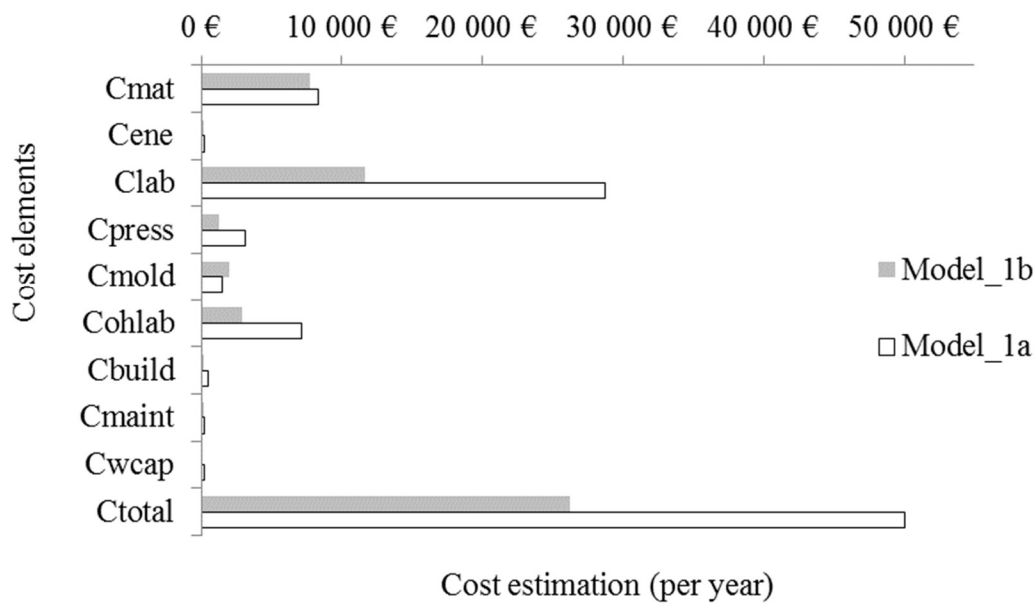


Figure 6-3. Elementary costs and total manufacturing costs estimation of both models for a batch number of 200k parts.

Adding features (stiffening ribs) to the model increases the mold cost but reduces the amount of material needed per shot. This modification considerably reduces the cycle time of the process. Consequently, the press, labor and overheads, working capital, maintenance and energy costs are also reduced. The cost of producing the required batch number is c.a. 50k € and 26k €, per year, respectively, for M2a and M2b. This corresponds to a per-part cost of 0.25 € (M2a) and 0.13 € (M2b).

### 6.5.2 Number of cavities

The influence of the number of cavities on the elementary and final costs is investigated for the specific case of M2b. The injection filling time was retained as 1.6s for the multicavity molds. Therefore, the cycle time is stable regardless the shot size needed to fill the cavities. Increasing the number of parts produced per shot has a strong effect on the production pace. However, it has a strong impact in the press and mold investment. This is highlighted in Figure 6-4.

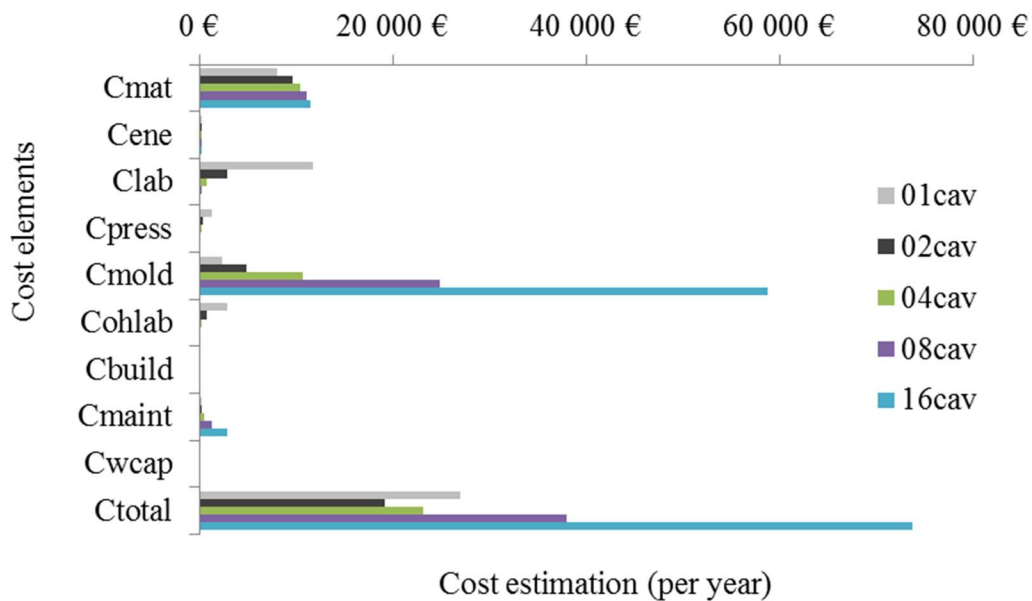


Figure 6-4. Elementary and total costs sensibility to the number of cavities.

When a multicavity mold is used, three main changes occur:

1. The cost of the mold is clearly higher;
2. A larger press (higher shot capacity – pressure and volume – and clamp force, and larger distance between tie columns) is needed;
3. The manufacturing time decreases, per part, in approximately inverse proportion to the number of cavities.

The investment on the tooling system is normally a dominant cost, principally for multicavity molds. Also, the material cost imparts a significant effect on the total cost of the part. Regarding the cost of the press, it is not evident that such cost increases with the mold size (part projected area) and machine clamp force. It must be noted that the PBC is proportional to the clamp force, however, the total investment on the press is also the result of the PLR (note that the line/press is assumed non-dedicated). The later has a stronger effect on the final press cost for higher number of cavities, i.e. the higher the number of cavities the lower the PLR.

Observing the total cost it may be concluded that the most cost-effective solution is the production of a 2-cavity mold. The annual cost of 200k M2b parts with a 2-cavity mold solution is of about 19k €, which corresponds to a per-part cost of 0.096 €. This leads to an overall cost reduction of 40% when compared to a single cavity mold solution.

### 6.5.3 Annual production volume

The annual production volume has a huge effect on the final cost of a product. A sensibility analysis was carried out to identify the influence of the batch number on the final cost of the injection molded part. The results are shown in Figure 6-5. The M2b and a 2-cavity mold were selected for demonstration.

The analysis reveals a sharp decrease of the per-part cost for an APV of 20k (approx. 0.334 €) to 200k (approx.. 0.096 €) parts per year. The higher the APV the lower the per-part cost. This effect is less evident for productions higher than 400k parts as shown by the dashed horizontal red line.

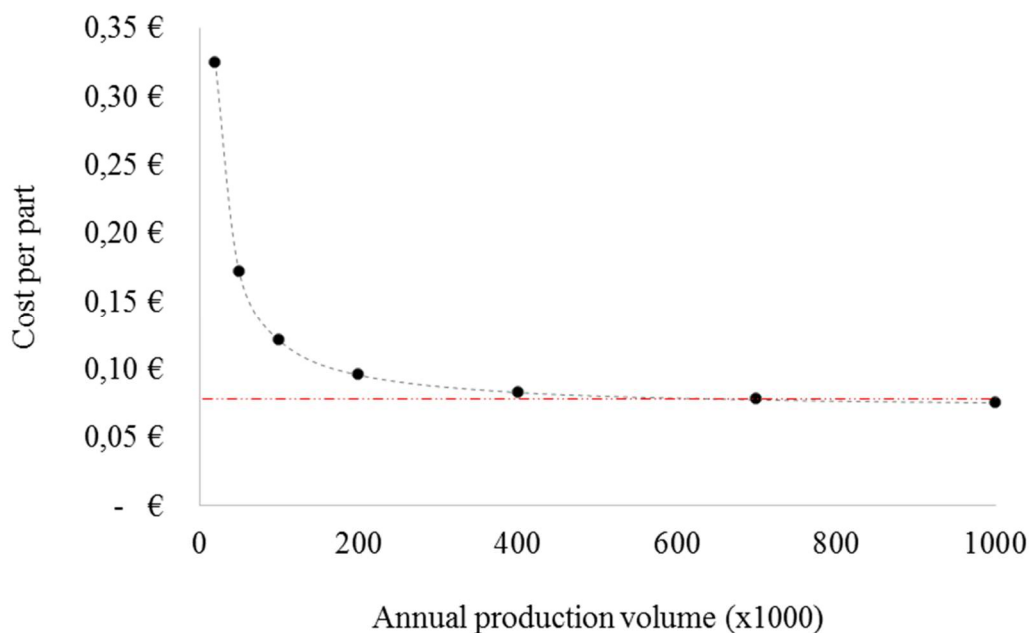


Figure 6-5. Cost per-part sensibility as a function of the annual production volume.

## 6.6 Conclusions

This work describes a methodology for cost estimation of injection molded parts. It is important to estimate the cost of new products through the conceptual and detail design phases. At this point, the technical drawings are still under development, i.e. not “frozen”/validated for production. Thus, the product design engineers have some “space” to analyze several scenarios in what concerns the design features or production issues.

With the proposed methodology, the product design engineers may evaluate the impact of their decisions on the final cost of the part, before the ramp-up production phase. This is highly important for the economic success of any product and, consequently, to the competitiveness of a company.

The methodology is based on a PBCM which is fed by relevant data from a plastic injection molding simulation software (AMI). Designer engineers use AMI to evaluate plastic part designs, injection mold designs, and manufacturing settings. These critical design and processing issues have a great impact on the final cost of a part. Thus, the current work proposes the contribution of AMI results to improve the accuracy of the PBCM.

The PBCM consists of a MS Excel workbook that encompasses three interrelated and interdependent models: a technical process model, a production operations model, and a financial accounting model. By changing data, creating new scenarios, design engineers can quickly evaluate the relative importance of elementary costs. Additionally, they are able to understand the economic consequences of their technical choices.

Considering the example described in the previous sections, the cost of a part is basically dependent on the part geometry, and consequently on mold and press, batch number, raw material and processing conditions (cycle time). It was demonstrated that the PBCM here exposed allows a better understanding on the sensitivity of injection molding costs to critical factors such as the design features, the annual production volume or the number of cavities.

## 6.7 Further research

The AMI-based technical cost model will help design engineers to understand the cost effectiveness of their technical options for injection molding thermoplastic parts. This is a preliminary version, with still some limitations, that must be tested and validated in real industrial environment situations. The authors believe that its usage may help improving the relationship among molders, mold makers, designers, engineers and raw material suppliers. Once validated by industrials, the next step is to suggest an updated version as an add-in for AMI.

## References

1. A.A. Fagade and D.O. Kazmer. *Journal of Injection Molding Technology*, 4, (2000).
2. K.T. Ulrich and S.D. Eppinger. *Product Design and Development* (2003)
3. H.S. Wang, Z.H. Che, and Y. N. Wang. *International Conference on Neural Networks, Vancouver* (2007).
4. H.S. Wang, Y.N. Wang, and Y.C. Wang. *Expert Systems with Applications*, 40 (2013)
5. C. Fernandes, A.J. Pontes, J.C. Viana, and A. Gaspar-Cunha. *Advances in Polymer Technology*, (2016).

6. R. Kirchain and F. Field. Encyclopedia of Materials Science and Engineering, 2, 1718 (2001).
7. J.-Y. Jung. Journal of Intelligent Manufacturing, 13, 227 (2002).
8. L. Pârv, M. Urdea. International Conference on Manufacturing Engineering, Quality and Production Systems (2009).
9. A. Locascio. International Journal of Flexible Manufacturing Systems, 12, 207 (2000).
10. M-C. Nadeau, A. Kar, R. Roth and R. Kirchain. International Journal of Production Economics, 128, 223 (2010).
11. F. Field, R. Kirchain, R. Roth. Journal of the Minerals, Metals and Materials Society, 59, 21 (2007).
12. A. Niazi, J.S. Dai, S. Balabani and L. Seveniratne. Journal of Manufacturing Science and Engineering, 128, 563 (2006).
13. Z.H. Che. Computers and Industrial Engineering, 58, 625 (2010).
14. O.N. Shing. Advances in Polymer Technology, 18, 33 (1999).
15. P. Jones. Budgeting, Costing and Estimating for the Injection Moulding Industry (2009).
16. [www.plasticsnews.com/resin](http://www.plasticsnews.com/resin)
17. D.V. Rosato, D.V. Rosato, M.G. Rosato. Injection Molding Handbook (2000).
18. K-H. Chang. Product Manufacturing and Cost Estimating using CAD/CAE – The Computer Aided Engineering Design Series (2013).
19. G. Boothroyd, P. Dewhurst, and W. Knight. Product Design For Manufacture and Assembly (2002).





## 7. GLOBAL SYNTHESIS

Thermoplastic injection molded components are extensively used in automotive applications. The manufacturing conditions of the automotive moldings have a significant influence on the final quality, performance (e.g. mechanical resistance) and cost. The computer aided engineering (CAE) tools such injection molding and crash simulations, represent a valuable help to meet those requirements. However, such tools are currently not integrated, i.e. the material models that mathematically describe the mechanical behavior and embedded in the structural analysis codes do not consider the effect of the manufacturing conditions, at least for unreinforced plastics. Thus, for a more accurate prediction of deformation and strength, the simulation methods must consider the locally varying microstructure characteristics in the thermoplastic parts. This work aims to improve this topic.

A comprehensive study of the mechanical properties dependency on the microstructure, strain rate, temperature, and processing conditions of injection molded polypropylene (PP) parts was carried out. This consisted of extensive laboratorial test samples preparation and testing. PP samples were obtained through controlled injection molding design of experiments with 25 different processing condition settings (with variations of the flow rate, melt and mold temperatures, and holding pressure). Advanced experimental techniques were employed: polarized light microscopy (skin thickness), wide-angle X-ray scattering (crystallinity, molecular orientation and polymorphism of the skin layer), and differential scanning calorimetry (bulk crystallinity), high velocity tensile tests (Young's modulus, stress at yield and strain at break) synchronized with high speed camera (20k fps), and dynamic-mechanical-thermal analysis (storage modulus and loss factor). The time-temperature superposition principle was adopted and master curves in the form of storage modulus vs. frequency were built (horizontal shift factors were modelled by the Arrhenius equation) to predict the elastic modulus at different strain rates. Response surface methodology and analysis of variance techniques were employed to understand the mechanical properties dependency on the microstructure, strain rate, temperature, and processing conditions. The melt temperature was identified as the most significant variable for the development of the morphologies and the mechanical response of the moldings. The skin thickness, its crystallinity and molecular orientation (flow direction) influence, to a certain degree, the tensile properties of the materials. The mold wall temperature was found to have the highest influence on the storage static modulus and frequency sensitivity coefficient.

The mechanical behavior of thermoplastic injection moldings is dictated to a large extent by the manufacturing conditions that impose a specific thermomechanical environment, thus a specific microstructure on the plastic components. Thus, the establishment of accurate relationships between the developed microstructure and the mechanical response is essential for improved mechanical behavior predictions. The thermo-mechanical indices (TMI) methodology was upgraded and used to create mathematical equations describing the relationships between simulated injection molding conditions and the final mechanical properties. A newly dedicated computer application (TMI-App) allows importing computer aided flow study results from the Autodesk Moldflow Insight (AMI) package and locally characterising the thermo-mechanical environment (TME) during the injection moulding process. The prediction of the mechanical properties through the TME assessment was accomplished, having shown good agreement, thus validating the proposed approach. Nevertheless, the quality of the mathematical fitting (given by the coefficient of multiple correlation) of the TMI vs. envisaged mechanical properties must be statistically improved mainly for the determination of the fracture strain. This may be accomplished by redefining the TMI equations.

Injection molding flow simulations and finite element analysis have been applied to simulate the injection molding process and the crashworthiness of thermoplastic parts (toolbox) under specific conditions. Different combinations of molding conditions were selected to manufacture the toolbox components. The objective of flow simulations is to extract the relevant thermomechanical history variables info which relates to mechanical property changes resulting from the imposed molding conditions. Since the microstructure is strongly affected by the molding conditions, a simulation chain was developed in order to include the effect of simulated molding conditions on the simulated mechanical behavior by coupling flow and crash simulations. A user-defined material model, embedded in the finite element analysis code, computes the TMI and translate them to local mechanical properties. The integrative simulation chain process was successfully applied, mostly for the elasto-plastic and hardening responses. The mechanical response of the toolboxes was analyzed through the developed simulation chain and validated by experimental testing. The force-displacement curves were experimentally and numerically assessed at 1 mm/s (quasi-static) and at 3 m/s (dynamic). The TME imposed by the defined molding conditions imparts minor changes in the response of the material under quasi-static conditions. This is observed for both the physical test and for the simulations. The quasi-static tests reported narrower standard deviation results than the dynamic tests. In the latter case, the differences among the defined molding conditions are enlarged. The quasi-static numerical simulations overestimate the attained peak force, but the overall material response (elastic and hardening) is representative of the expected trend. In the case of dynamic

numerical simulations, the newly approach seem to describe correctly most of the real curves in terms of peak force and initial slope.

Overall, the simulation chain process was successfully applied. However, the proposed integrative methodology still needs a finetuning. The accuracy of the mechanical properties predictions of injection molded thermoplastics is dependent on several factors, such as: moldflow mesh model, processing settings (simulation and shop floor), finite element mesh model, physical and numerical boundary conditions, mechanical properties assessment at different strain rates and temperatures, relationships between molding conditions and mechanical properties, and the mathematical description of the material behavior (material model). The combination of these issues influences the accuracy of our predictions.